III–V Nanowire Surfaces

Hjort, Martin

2014

III–V Nanowire Surfaces

Martin Hjort

LUND
UNIVERSITY

DOCTORAL DISSERTATION
by due permission of the Faculty of Science, Lund University, Sweden.
To be defended in the Rydberg Lecture Hall at the Department of Physics
February 7, 2014, at 10:15.

Faculty opponent
Prof. Rudolf M. Tromp
Universiteit Leiden, Netherlands
IBM T. J. Watson Research Center, USA

Organization	Document name
LUND UNIVERSITY	DOCTORAL DISSERTATION
Division of Synchrotron Radiation Research Department of Physics Box 118 S-221 00 Lund	Date of issue December 20, 2013
Author(s) Martin Hjort	Sponsoring organization

Title and subtitle: III–V Nanowire Surfaces

Abstract

This dissertation deals with the geometric and electronic structure of surfaces on III–V semiconductor nanowires (NWs). NWs made of InAs, GaAs, and InP have been studied using scanning tunneling microscopy/spectroscopy (STM/S), low energy electron microscopy (LEEM), photoemission electron microscopy (PEEM), and x-ray photoelectron spectroscopy (XPS).

All of the mentioned techniques have been developed to study 2-dimensional samples and issues related with the adaption to 3-dimensional nanostructures are discussed, together with solutions on how to overcome them. Preparation techniques of NW samples for surface science studies, including an effective and seemingly non-destructive deoxidation routine using atomic hydrogen have been developed.

Using STM/S, it has become possible to study the atomic arrangement at NW surfaces and evaluate the electronic structure with very high spatial precision. NWs have been studied showing metallic surfaces due to step induced states, Fermi level pinned surfaces, and unpinned surfaces allowing for general probing of NW properties. With the STM, it was possible to image from micrometers along individual NWs down to the atomic scale evaluating, among other things, tapering, surface morphology, and surface reconstructions.

Using LEEM/PEEM as a novel tool for NW studies, it has become possible to determine electronic and geometrical properties of NWs using low energy electrons or photoelectrons. NW dopant incorporation, work function, and surface atomic arrangement were studied. In addition, XPS was used to study NW surface chemistry and interfacial chemistry for NWs covered in high-κ oxides.

Key words

III–V semiconductor materials, nanowire, surface, scanning tunneling microscopy, scanning tunneling spectroscopy, low energy electron microscopy, photoemission electron microscopy, photoelectron spectroscopy

Classification system and/or index terms (if any)

Supplementary bibliographical information	Language English

ISSN and key title	ISBN 978-91-7473-813-1 (print) 978-91-7473-814-8 (pdf)

Recipient's notes	Number of pages 191	Price
	Security classification	

Distribution by Division of Synchrotron Radiation Research, Department of Physics, Lund University, P.O. Box 118, S-221 00 Lund, Sweden

III–V Nanowire Surfaces

Martin Hjort

Doctoral Dissertation
2014

LUND
UNIVERSITY

Division of Synchrotron Radiation Research
Department of Physics
Lund University

Front cover:
STM image depicting the top-most As-atoms on a GaAs (11–20) facet.

Back cover:
A leek in a vacuum chamber.
2012 annual image contest winner at the Center for Functional Nanomaterials, Brookhaven National Laboratory. Photographer: Erik Månsson

Division of Synchrotron Radiation Research
Department of Physics
Lund University
ISBN: 978-91-7473-813-1
ISB(N+1): 978-91-7473-814-8

Printed in Sweden by Media-Tryck, Lund University
Lund 2013

"Das Volumen des Festkörpers wurde von Gott geschaffen,
seine Oberfläche aber wurde vom Teufel gemacht"
– Wolfgang Pauli

Abstract

This dissertation deals with the geometric and electronic structure of surfaces on III–V semiconductor nanowires (NWs). NWs made of InAs, GaAs, and InP have been studied using scanning tunneling microscopy/spectroscopy (STM/S), low energy electron microscopy (LEEM), photoemission electron microscopy (PEEM), and x-ray photoelectron spectroscopy (XPS).

All of the mentioned techniques have been developed to study 2-dimensional samples and issues related with the adaption to 3-dimensional nanostructures are discussed, together with solutions on how to overcome them. Preparation techniques of NW samples for surface science studies, including an effective and seemingly non-destructive deoxidation routine using atomic hydrogen have been developed.

Using STM/S, it has become possible to study the atomic arrangement at NW surfaces and evaluate the electronic structure with very high spatial precision. NWs have been studied showing metallic surfaces due to step induced states, Fermi level pinned surfaces, and unpinned surfaces allowing for general probing of NW properties. With the STM, it was possible to image from micrometers along individual NWs down to the atomic scale evaluating, among other things, tapering, surface morphology, and surface reconstructions.

Using LEEM/PEEM as a novel tool for NW studies, it has become possible to determine electronic and geometrical properties of NWs using low energy electrons or photoelectrons. NW dopant incorporation, work function, and surface atomic arrangement were studied. In addition, XPS was used to study NW surface chemistry and interfacial chemistry for NWs covered in high-κ oxides.

Populärvetenskaplig sammanfattning

Nanoteknologi handlar om att på ett kontrollerat sätt utnyttja strukturer med minst en dimension i nanometerområdet (i storleksordningen 1 till 100 miljondels millimeter). Nanostrukturer har använts under lång tid och redan under medeltiden användes guldpartiklar av varierande storlek för att tillverka infärgade glas. Idag använder vi nanoteknologi dagligdags, t.ex. i våra mobiltelefoner.

Sedan 60-talet har så kallade halvledarmaterial (främst kisel) revolutionerat vårt sätt att se på världen genom de uppfinningar som de har gett upphov till, exempelvis datorer. Halvledare är väldigt användbara då vi kan styra deras elektriska ledningsförmåga från isolerande till nästan metalliska. Solceller, lysdioder, och transistorer bygger alla på halvledarmaterial och klassiskt har dessa tillverkats (”odlats”) i två dimensioner (2D) med olika funktionella lager ovanpå varandra. Under mer än 10 år har det i Lund forskats på ett nytt sätt att odla halvledare: som nanotrådar. Nanotrådar har en diameter i storleksordningen tiotals nanometer och kan vara 100 gånger längre än vad de är tjocka. Att odla materialet i trådform har visat sig väldigt fördelaktigt då det bl.a. ger en möjlighet att kombinera material som inte går att få att passa ovanpå varandra vid 2D-odling.

När saker görs mindre ökar andelen yta i förhållande till volym (bulk) och på grund av de små tjocklekarna för nanotrådar är mängden yta i förhållande till bulk väldigt stor. Det har en betydande påverkan på de elektroniska egenskaperna som härleds från hur atomerna är placerade i materialet (kristallsymmetrin). Vid ytan bryts per definition symmetrin och ytegenskaperna kommer därför skilja sig från de som finns inuti bulken. Eftersom ytan är den plats vid vilken materialet interagerar med omvärlden är det av yttersta vikt att veta dess egenskaper. Om man vet hur atomerna är arrangerade på ytan och deras kemiska tillstånd har man goda möjligheter att t.ex. förutspå vilka gaser som kan fastna på ytan, något som är viktigt vid tillverkning av sensorer.

I den här avhandlingen beskriver jag tillvägagångssätt för att använda klassiska ytkaraktäriseringsmetoder för bestämning av atomers position samt deras elektroniska egenskaper för flera olika sorters halvledarnanotrådar. Metoderna som jag har valt att använda mig av är sveptunnelmikroskopi, lågenergielektronmikroskopi, fotoemissionselektronmikroskopi, och fotoelektronspektroskopi.

I sveptunnelmikroskopi låter man elektroner tunnla – ett kvantmekaniskt fenomen där elektronerna kan passera barriärer som de klassiskt inte borde kunna – mellan provet och

en atomärt skarp metallspets. Genom att flytta spetsen med oerhört hög precision (noggrannhet på 1 miljarddels millimeter) går det att mäta hur många elektroner som tunnlar på olika platser på provet. Med den informationen går det att visualisera var olika atomer finns på ytan och deras elektroniska egenskaper.

I ett lågenergielektronmikroskop låter man elektroner med låg rörelseenergi interagera med provet och genom att undersöka hur elektronerna sprids kan man bilda sig en uppfattning om atompositioner på ytan. Ytkänsligheten kommer av att elektroner med låg energi sprids väldigt lätt och kan därför bara interagera med de översta atomlagren i provet.

I ett fotoemissionselektronmikroskop belyser man provet med högintensivt, monokromatiskt, röntgenljus (synkrotronljus) vilket leder till emission av fotoelektroner. Genom att studera varifrån elektroner med olika rörelseenergi emitteras går det att bestämma vilka ämnen som finns på provet och var, deras kemiska tillstånd (t.ex. om de är oxiderade), samt eletroniska egenskaper såsom utträdesarbete. Elektronerna som studeras har även här låg energi vilket gör att metoden klassas som ytkänslig.

Fotoelektronspektroskopi fungerar på ett liknande sätt, där röntgenljus får infalla på ett prov vilket leder till emission av elektroner. I fotoelektronspektroskopiuppställningen går det att få mycket högre energiupplösning än i mikroskopiuppställningen vilket gör att man t.ex. kan differentiera mellan olika oxider.

I avhandlingen har jag studerat nanotrådar av 3 olika halvledarmaterial: galliumarsenid (GaAs), indiumarsenid (InAs), och indiumfosfid (InP). Dessa material besitter flertalet egenskaper som gör dem högintressanta för framtida optik- och elektroniklösningar. Exempelvis så rör sig elektroner väldigt snabbt i materialen (hög mobilitet) vilket gör att de lämpar sig väl för höghastighetselektronik.

En intressant detalj med nanotrådar är att man kan ändra hur atomerna placerar sig i materialet genom att ändra odlingsparametrar. Som nämndes tidigare bestämmer atomernas position de elektroniska egenskaperna och de subtila skillnaderna mellan ett material odlat i olika kristallstrukturer har länge debatterats. Genom att studera nanotrådarna med flera olika tekniker hag jag kunnat utröna vad som händer både med atomernas position och deras elektroniska egenskaper då kristallstrukturen varieras. De upptäckterna är av intresse för såväl grundforskning som för tillämpningar inom exempelvis elektronik.

Acknowledgments

There are plenty of people who have helped me during my PhD studies and whom I would like to thank. The contributions of each and every one of you have been very valuable to me. If you are not acknowledged here, please forgive me.

First and foremost, I would like to thank my supervisor, Anders Mikkelsen, for always finding time for me. I greatly admire your skill of having new ideas on how to deal with measurements that seem to point towards opposite conclusions. It has been a pleasure to do my PhD studies under your supervision.

I would like to thank my co-supervisor, Edvin Lundgren, for all your enthusiasm and support. Thank you also for hosting the annual kick-off!

I am indebted to Rainer Timm, who has not only been excellent in teaching me everything there is to know about STS, organizing beam times, and commenting on manuscripts, but has also been a very nice travel companion on numerous conferences and experiment sessions abroad.

I would like to thank Alexei Zakharov for introducing me to the power of LEEM and PEEM. It has been great working with you! Thanks are also due to Karina Thånell for keeping beam line I311 in excellent shape. I would like to thank Jesper Andersen for his good sense of humor.

Thank you, Lars Samuelson, for creating the world leading nanoscience environment within the nanometer structure consortium.

The whole research group led by Kimberly Dick Thelander is acknowledged for providing me with crystal structure engineered nanowires of unprecedented quality. Special thanks go out to Sebastian Lehmann for his good will in providing samples especially suited for my experiments, for his ability to direct my attention to those samples, and for great companionship during visits abroad. Thank you, Daniel Jacobsson, for great collaboration on hosting the CGMS-meetings.

Another sample related acknowledgement goes to Magnus Borgström and Jesper Wallentin for giving me the opportunity to study state-of-the-art doped InP NWs.

Thank you, present and former group members of Lars-Erik Wernersson, for a very interesting collaboration on the high-κ on III–V studies.

Thanks Bernhard Mandl for collaboration on the Au-free NW project, which finally seems to have left the drawer.

The group of Peter Kratzer is acknowledged for theoretical calculations and simulations.

I would like to thank Emelie Hilner for teaching me how to use the STM and giving me a flying start.

Johan Knutsson, thanks for always keeping a good mood when working together on plenty of projects. I would also like to thank you for all the help with 3D visualization of nanowires.

Shane Kennedy and David Jesson are acknowledged for their excellent work in explaining mirror electron mode contrast when studying nanowires.

I would like to thank present and former members at the Division of Synchrotron Radiation Research for creating a pleasant and inspiring work environment.

My collaborators at Brookhaven National Laboratory, Percy Zahl and Peter Sutter, are acknowledged. Percy, thanks for always keeping the STM in great condition and for being such a welcoming host. It has always been a pleasure to come and visit you!

I would like to acknowledge everyone who has assisted me during the writing of this dissertation: Anders Mikkelsen, Edvin Lundgren, Rainer Timm, Dan Hessman, Alexei Zakharov, Sebastian Lehmann, Johan Knutsson, and Erik Mårsell. Your help really improved the dissertation.

The Royal Physiographic Society in Lund is acknowledged for their financial support.

I would like to thank Jason Kawasaki (Big J), and Sahil Patel, UCSB, for showing me around in Santa Barbara and for great collaboration on the ARPES project. Closely connected, I would also like to thank Nyan Cat.

The people behind the conference updates are acknowledged – Erik Mårsell, Filip Lenrick, Daniel Jacobsson, *et al*. Thank you for sharing.

Olof Persson is acknowledged for sharing my compassion for curry wurst.

Thank you, Erik Mårsell, for great discussions.

HRH Prince Daniel is acknowledged for inspiration.

Thanks to everyone who has contributed to the black board filled with puns (mainly Erik Mårsell). “Idag e-mail, igår morse.”

My family and friends, thanks for your endless support!

My wife, Anna, for always being there for me, I love you!

Abbreviations and symbols

1D, 2D, 3D	One-, two-, and three-dimensional
III–V	Compound comprised of one group III-element and one group V-element in the periodic table
ARPES	Angle resolved photoelectron spectroscopy
CB	Conduction band
EBL	Electron beam lithography
E_F	Fermi energy
E_g	Energy band gap
E_i	Ionization energy (energy distance, valence band edge to vacuum)
E_{vac}	Vacuum energy level
fcc	Face-centered cubic
hcp	Hexagonally close packed
I_t	Tunneling current
kPEEM	k-resolved photoemission electron microscopy
(L)DOS	(Local) Density of states
LEEM	Low energy electron microscopy, also for microscope
MBE	Molecular beam epitaxy
MEM	Mirror electron microscopy
MFP	Mean free path
MOVPE	Metal-organic vapor phase epitaxy
NW	Nanowire
QD	Quantum dot
SE	Secondary electron
SEM	Scanning electron microscopy, also for microscope
SPELEEM	Spectroscopic photoemission and low-energy electron microscope
STM	Scanning tunneling microscopy, also for microscope
STS	Scanning tunneling spectroscopy
TEM	Transmission electron microscopy, also for microscope
TIBB	Tip-induced band bending
TPS/TSL	Twinplane superlattice
UHV	Ultra-high vacuum ($p < 10^{-9}$ mbar)
VB	Valence band
V_T	Sample bias
Wz	Wurtzite

(X)PEEM	(X-ray) Photoemission electron microscopy
XPS	X-ray photoelectron spectroscopy
Zb	Zinc blende
(μ)LEED	(micro) Low energy electron diffraction
(hkl)	Miller index notation for a specific plane
{hkl}	A family of equivalent planes
[hkl]	A specific direction
<hkl>	A family of equivalent directions
(111)A	The group III terminated (111) surface in a Zb crystal
(111)B	The group V terminated (−1−1−1) surface in a Zb crystal
Φ	Work function (energy distance, Fermi energy to vacuum)
χ	Electron affinity (energy distance, conduction band edge to vacuum)

List of papers

This dissertation is based on the following papers, which will be referred to in the text by their Roman numerals

I

Direct Atomic Scale Imaging of III–V Nanowire Surfaces

E. Hilner, U. Håkansson, L.E. Fröberg, M. Karlsson, P. Kratzer, E. Lundgren, L. Samuelson, and A. Mikkelsen

Nano Letters **8**, 3978 (2008)

In this paper we present the first STM image of III–V nanowire surfaces.

I took part in the development of the cleaning procedure of the nanowires, performed the electrical measurements, and took part in the discussion of the manuscript. My previous surname was Karlsson.

II

Direct Imaging of Atomic Scale Structure and Electronic Properties of GaAs Wurtzite and Zinc Blende Nanowire Surfaces

M. Hjort, S. Lehmann, J. Knutsson, R. Timm, D. Jacobsson, E. Lundgren, K.A. Dick, and A. Mikkelsen

Nano Letters **13**, 4492 (2013)

In this paper we present the first STM and STS study of GaAs NWs.

I planned the experiment, developed the cleaning procedure, took part in the measurements, analyzed the data, and wrote the manuscript.

III

Surface Chemistry, Structure, and Electronic Properties from Microns to the Atomic Scale of Axially Doped Semiconductor Nanowires

M. Hjort, J. Wallentin, R. Timm, A.A. Zakharov, U. Håkansson, J.N. Andersen, E. Lundgren, L. Samuelson, M.T. Borgström, and A. Mikkelsen

ACS Nano **6**, 9679 (2012)

In this paper we present the first STM and STS study of InP NWs.

I planned the experiment, developed the cleaning procedure, took part in the measurement, analyzed the data, and wrote the manuscript.

IV

Doping Profile of InP Nanowires Directly Imaged by Photoemission Electron Microscopy

M. Hjort, J. Wallentin, R. Timm, A.A. Zakharov, J.N. Andersen, L. Samuelson, M.T. Borgström, and A. Mikkelsen

Applied Physics Letters **99**, 233113 (2011)

In this paper we present a fast method for the determination of axial doping profiles in NWs.

I planned the experiment, took part in the measurements, analyzed the data, and wrote the manuscript.

V

Characterizing the Geometry of InAs Nanowires using Mirror Electron Microscopy

S.M. Kennedy, M. Hjort, B. Mandl, E. Mårsell, A.A. Zakharov, A. Mikkelsen, D.M. Paganin, and D.E. Jesson

Nanotechnology **23**, 125703 (2012)

In this paper we present a novel microscopy method for characterization of nanowires.

I took part in the measurements, analyzed the experimental data, and took part in discussion of the manuscript.

VI

Interface Composition of InAs Nanowires with Al_2O_3 and HfO_2 Thin Films

R. Timm, M. Hjort, A. Fian, B.M. Borg, C. Thelander, J. N. Andersen, L.-E. Wernersson, and A. Mikkelsen

Applied Physics Letters **99**, 222907 (2011)

In this paper we studied the interfacial chemistry of high-κ oxide wrapped InAs NWs using x-ray photoelectron spectroscopy.

I took part in the measurements, and discussions about the manuscript.

VII

Electronic and Structural Mapping of Wurtzite and Zinc Blende InAs Nanowire Surfaces

M. Hjort, S. Lehmann, J. Knutsson, A.A. Zakharov, Y.A. Du, S. Sakong, R. Timm, G. Nylund, E. Lundgren, P. Kratzer, K.A. Dick, and A. Mikkelsen

(in manuscript)

In this paper we studied the electronic structure of InAs nanowires exhibiting axial stacking of wurtzite and zinc blende segments.

I planned the experiment, took part in the measurements, analyzed the data, and wrote the manuscript.

VIII

Scanning Tunneling Microscopy Studies of Au-free Grown InAs Nanowires

M. Hjort, J. Knutsson, B. Mandl, R. Timm, E. Lundgren, K. Deppert, and A. Mikkelsen

(in manuscript)

In this paper we present a STM study of InAs NWs grown without the use of a catalytic Au-particle.

I planned the experiment, took part in the measurements, analyzed the data, and wrote the manuscript.

List of papers not included in the dissertation to which I have contributed

IX. Epitaxial Growth and Surface Studies of the Half Heusler Compound NiTiSn (001)

J.K. Kawasaki, T. Neulinger, R. Timm, M. Hjort, A.A. Zakharov, A. Mikkelsen, B.D. Schultz, and C.J. Palmstrom

Journal of Vacuum Science and Technology B **31**, 04D106 (2013)

X. Al_2O_3/InAs Metal-Oxide-Semiconductor Capacitors on (100) and (111)B Substrates

J. Wu, E. Lind, R. Timm, M. Hjort, A. Mikkelsen, and L.-E. Wernersson

Applied Physics Letters **100**, 132905 (2012)

XI. Interface Composition of Atomic Layer Deposited HfO_2 and Al_2O_3 Thin Films on InAs Studied by X-ray Photoemission Spectroscopy

R. Timm, M. Hjort, A. Fian, C. Thelander, E. Lind, J.N. Andersen, L.-E. Wernersson, and A. Mikkelsen

Microelectronic Engineering **88**, 1091 (2011)

XII. Reduction of Native Oxides on InAs by Atomic Layer Deposited Al_2O_3 and HfO_2

R. Timm, A. Fian, M. Hjort, C. Thelander, E. Lind, J.N. Andersen, L.-E. Wernersson, and A. Mikkelsen

Applied Physics Letters **97**, 132904 (2010)

Contents

1. Introduction

In surface science in general, and also in this dissertation, the surface is defined as the outermost (few) atomic layer(s). For most materials, the surface atoms only constitute a minute part compared to the number of atoms in the bulk of the crystal. However, the surface is a material's interface to the surroundings, being the place where it interacts with foreign species. In order to understand and predict phenomena such as gas adsorption, crystal growth, and chemical reactions at surfaces, it is important to characterize the surface's chemistry, geometry, and its electronic structure. In addition, as dimensions shrink, the surface-to-bulk ratio goes up, and for nanostructures, it is no longer possible to define properties from the bulk only, but the surface needs to be considered.

Since the surface breaks the translational symmetry in the direction perpendicular to the surface, it will inevitably alter the electronic structure and can induce states bound to the surface, so called surface states. Further, it is common for surface atoms to relax or rearrange in order to lower the energy associated with the surface. Thereby, the surface is sometimes seen not to be a simple truncation of the bulk structure but rather experience a complex reconstruction pattern. Characterizing these phenomena is a prerequisite in order to predict and utilize surface properties.

Within surface science, several different techniques are available, working with either physical probes (e.g. scanning tunneling microscopy/spectroscopy, STM/S, and atomic force microscopy, AFM), electrons (e.g. low energy electron diffraction, LEED, and low energy electron microscopy, LEEM), or photons (e.g. x-ray photoelectron spectroscopy, XPS, or x-ray photoemission electron microscopy, XPEEM). The use of one technique, most often, only gives partial information and comparative studies are needed for a complete understanding of a system.

All of these probes have been developed to analyze model systems in the form of very flat single crystals. One of the goals of this dissertation has been to develop new concepts and use conventional surface science techniques to study surface properties on novel nanostructures. As an example, it can be mentioned that corrugations of more than about 5 Å are usually considered large in STM. Studying nanostructures with heights of tens to hundreds of nanometers is indeed far from trivial.

One of the most promising types of nanostructures for applications within energy harvesting, light emission, and electronics, is III–V nanowires (NWs), which has received enormous attention during the past 15 years. III–V NWs are rod-shaped, crystalline

objects with diameters in the nanometer range and lengths in the micrometer regime, composed of materials from group III (e.g. Ga) and group V (e.g. As) in the periodic table. III–V materials possess several advantages over the more readily available silicon, making them attractive for research. III–V materials cover a wide band gap range from < 0.2 eV (InSb) to > 3 eV (GaN), i.e. covering the energy range for visible photons. Many of these materials have a direct band gap and can be integrated on the cheap Si platform for efficient, low-cost light emitting diodes (LEDs)[1, 2]. Further, III–V materials have very high carrier mobilities and are well-suited as channel materials in high-speed electronics[3, 4]. In addition, it has recently been shown that III–V NWs can be used to make high-efficiency solar cells[5].

It is well-known that NWs can be affected by the surface, e.g. the photoluminescence properties of pure GaAs is usually much lower than for GaAs grown in a core-shell geometry[6]. Despite this, surfaces of NWs are in general poorly understood and when I started my PhD studies, no experimental STM studies showing atomically resolved images of NW surfaces had been presented. However, the STM had been used to study NWs, but only in cross-sectional geometry[7] where the surface properties were left uncharacterized.

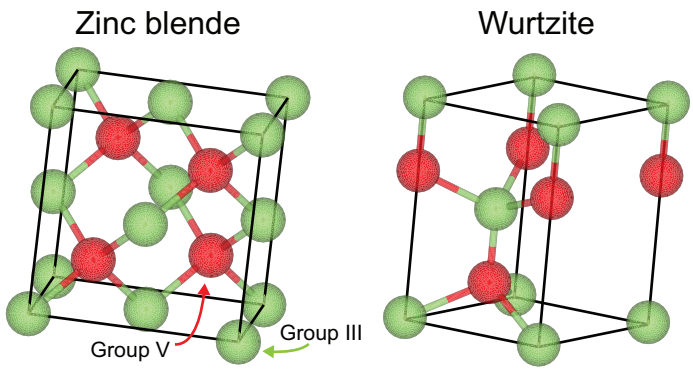

Figure 1.1. The unit cell of zinc blende and wurtzite, respectively. Each atom is tetrahedrally coordinated in both structures. Group V-atoms are depicted as red spheres, whereas group III-atoms are depicted as green spheres.

III–V materials (except III–N) exist naturally in the cubic zinc blende (Zb) crystal structure which can be seen as two interpenetrating face-centered cubic (fcc) lattices placed at (0,0,0) and (1/4,1/4,1/4), respectively. The Zb crystal structure is closely related to the diamond structure, in which both sub lattices are comprised of the same atomic species. In the form of NWs, III–V materials can also crystallize in the hexagonal wurtzite (Wz) structure which can be viewed as two interpenetrating hexagonal close-packed (hcp)

lattices. The unit cells of both these structures are shown in Figure 1.1. The Wz structure gives access to surfaces not found in other geometries, and is therefore an excellent playground for fundamental surface science studies.

In the work presented in this dissertation, several different material systems and characterization techniques have been used, but a common theme in all the investigations, was the use of ultra-high vacuum technology (UHV, $p < 10^{-9}$ mbar). Proper UHV conditions are needed to keep sample surfaces clean and allow for prolonged investigations without adsorption of foreign species, e.g. oxygen. UHV conditions are also needed in order to reduce electrons scattering off rest gases in the systems when performing measurements involving low energy electrons. In fact, a substantial part in the making of the work behind this dissertation has been devoted to achieve, and maintain UHV conditions in an assortment of experimental systems.

The experimental results presented in this dissertation were obtained by me, if nothing else is noted.

This dissertation is built up as follows. Chapter 2 deals with an introduction to NWs and how they need to be prepared for surface science studies. Crystal structure engineering and its implications on NW geometry, and electronic structure is also discussed.

In Chapter 3 and 4, I discuss the capabilities for NW studies presented by the scanning tunneling microscope. Large and atomic scale imaging on NWs of varying III–V materials are presented. Spectroscopic measurements revealing the electronic surface structure of the NWs are presented and discussed from a tip-induced band bending perspective.

Chapter 5 gives a brief introduction to low energy electron diffraction and photoelectron spectroscopy – two techniques that were used to gain additional insight into the surface properties of NWs.

In Chapter 6 surface sensitive electron microscopy in the form of low energy electron microscopy (LEEM) and photoemission electron microscopy (PEEM) is discussed. The possibilities and limitation of LEEM and PEEM when doing NW related research are exemplified for several different structures and material systems.

Chapter 7 contains conclusions and describes some possible routes for future NW surface science studies.

In Chapter 8, the papers that constitute the second part of the dissertation are summarized.

2. III–V semiconductor nanowires

III–V semiconductor nanowires (NWs) are elongated, rod-shaped crystalline objects with diameters in the nanometer range and lengths in the micrometer regime made of stoichiometric amounts of materials from group III (e.g. indium or gallium) and group V (e.g. phosphorus or arsenic) in the periodic table. III–V NWs have attracted a lot of attention for their use within, among other things, high-performance electronics[8, 9], photovoltaics[5, 10, 11], light-emitting diodes[2], studies of low-dimensional physics[12], and recently for studies of Majorana fermions[13-15]. Owing to the small diameter of the NWs they can: 1) relax strain in a lateral manner and allow for axial stacking of heavily lattice-mismatched materials[16, 17], 2) allow for seamless integration on Si-substrates[18], 3) confine carriers in 1-dimension and allow 1D ballistic transport[19], 4) show structural and optoelectronic properties different from corresponding bulk materials[20]. Due to the possible 1D carrier confinement, NWs are sometimes referred to as 1D-structures. From a surface science viewpoint, where samples traditionally have very low corrugation in the Ångström regime, NWs can also be referred to as 3D-structures. Importantly, all NWs in this work have diameters of about 100 nm or larger which is above the quantization limit.

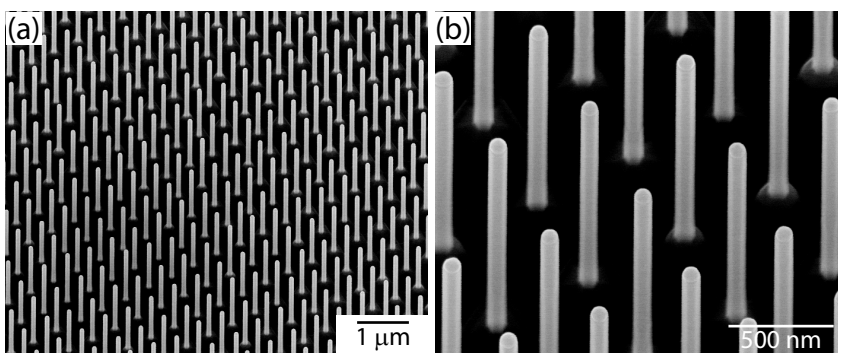

Figure 2.1. 30 ° tilted view SEM images depicting InAs NWs grown on a pre-patterned substrate.

An example of NWs grown on a pre-patterned substrate can be seen in Figure 2.1 with InAs NWs grown normal to the substrate.

2.1 Growth

All NWs presented in this dissertation were grown epitaxially on crystalline substrates using Au particles to catalyze the growth or grown self-catalyzed using mask-openings in a SiO_x film to define the NW positions. This dissertation is not intended to give a detailed description of NW growth, but a review of Au-catalyzed NW growth can be found in Reference[21], whereas a review of Au-free growth can be found in Reference[22]. Several other types of III–V NW growth have been reported, e.g. gas-phase grown NWs[23], and NWs grown on amorphous substrates[24], which are recommended for the interested reader but are not covered in this dissertation. Au-particle assisted growth of NWs is commonly thought to proceed in the steps outlined in Figure 2.2[25].

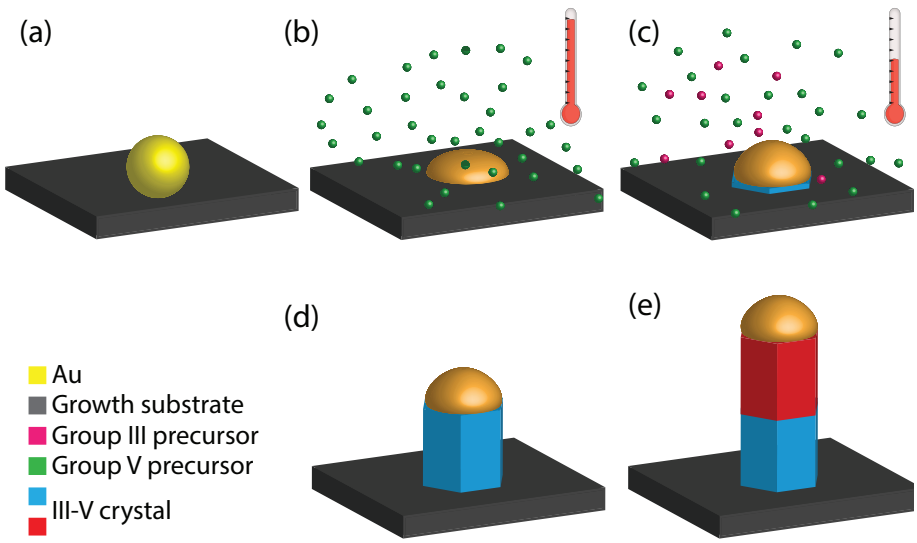

Figure 2.2. Au-particle assisted NW growth. (a) Size selected Au particles are deposited on a growth substrate. (b) The sample is annealed under group-V flow to allow the Au-particle to alloy with the substrate and for removal of surface oxides/contaminants. (c) Temperature is lowered and group III-precursor is introduced. III–V materials precipitate directly under the Au-particle. (d) After growth the vertical NW still resides with the Au-alloy on top. (e) Changing of precursors or introductions of dopant during growth allows for formation of axial heterostructures.

NWs have been found to prefer to grow in the [–1–1–1] direction and are most often grown on (111)B substrates so that they grow perpendicularly to the growth substrate. First, size selected Au-particles are deposited on a growth substrate, Figure 2.2(a). Several

routes exist for the creation of high quality Au particles, e.g. aerosol techniques or electron beam lithography (EBL), which have been reviewed by Messing *et al.*[26]. The substrate with Au-particles is introduced into a metal-organic vapor phase epitaxy (MOVPE) growth reactor (other growth methods such as molecular beam epitaxy are also possible but no such NWs have been studied in the work behind this dissertation). Secondly, the temperature is increased under group V precursor flow in order to alloy the Au-particle with the substrate and to remove oxide residues and contaminants on the substrate, Figure 2.2(b). To initiate growth, the temperature is reduced so that nucleation only takes place under the Au-particle (and not on the substrate), typically 400-600 °C. Growth constituents are introduced as organometallics (e.g. trimethylindium) and hydrides (e.g. arsine). The group III material is then thought to enter the Au-particle and supersaturate it, Figure 2.2(c). At the interface in between the vapor, the Au-group-III alloy, and the substrate, growth material precipitates into a nucleus which rapidly grows and forms a new layer of crystal directly beneath the Au-particle. The result is a single crystalline NW where the diameter is set by the Au-particle and the length is determined by the growth time, Figure 2.2(d). Changing the growth conditions by e.g. switching the precursors allows for the making of axial heterostructures as in Figure 2.2(e). By increasing the growth temperature so that material can nucleate also on the NW side facets, radial heterostructures (core-shell) can be grown.

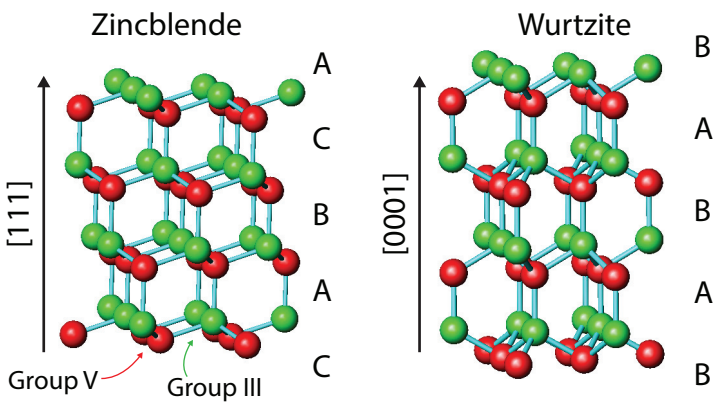

Figure 2.3. Schematic view of 4 bilayers of small Zb and Wz crystals. The difference in stacking sequence (ABC or AB) is seen for both structures. The green and red spheres denote group III- and group V-atoms, respectively. Both models are rotated 10 ° and tilted 5 ° from the <110> direction.

The growth of NWs is an epitaxial process meaning that the crystal structure of the growth substrate continues into the NW. Even though most III–V materials (except for

the nitrides) occur naturally only in the cubic zinc blende (Zb) crystal structure, the hexagonal wurtzite (Wz) structure has been found in NWs. When observed along the NW growth direction ([-1-1-1] and [000-1] for Zb and Wz, respectively) it is the stacking sequence of each bilayer that differs. Zb adopts …ABCABC… stacking whereas Wz adopts …ABABAB… stacking of the bilayers where A, B, and C denote different atomic stacking positions. Most non-optimized NW growth does not show pure Zb or pure Wz stacking, but rather a mixture with small Zb and Wz segments with plenty of stacking defects in between. Polytypes with a larger repetition cell than …ABC… have also been reported[21] but is not covered in this dissertation. Uncontrolled stacking in NWs have been shown to be detrimental to NW device performance[27-30]. Enormous efforts have therefore been put into making NWs with pure crystal structure (both Wz and Zb) by tuning parameters such as growth temperature[31, 32], NW diameter[33, 34], total precursor flows[31, 32], nominal V–III ratio[31, 35, 36], introduction of dopants[27, 36-39], and by group V precursor flow tuning[40]. For the NWs presented in this dissertation, the NW crystal structure has been tuned either by dopant incorporation (Paper III and IV), or by tuning the group V precursor flow (Paper II and VII). The latter method is well-suited for creation of sharp interfaces since gas flows can be changed almost instantaneously. Further on, it allows a constant growth temperature, and even though precursor migration length and precursor pyrolysis might be affected by the group V flow, the effect is expected to be minor compared to changing the growth temperature[40].

2.2 Surfaces

NWs typically show low index side facets of {110} and {112} character for Zb ({11–20} and {10–10} for Wz)[41]. {110}, {11–20}, and the {10–10} type facets are non-polar and the atomic stacking positions of the unreconstructed side facets can be seen in Figure 2.4. The {112} facet is polar which can be seen by the atomic stacking in the second top most layer.

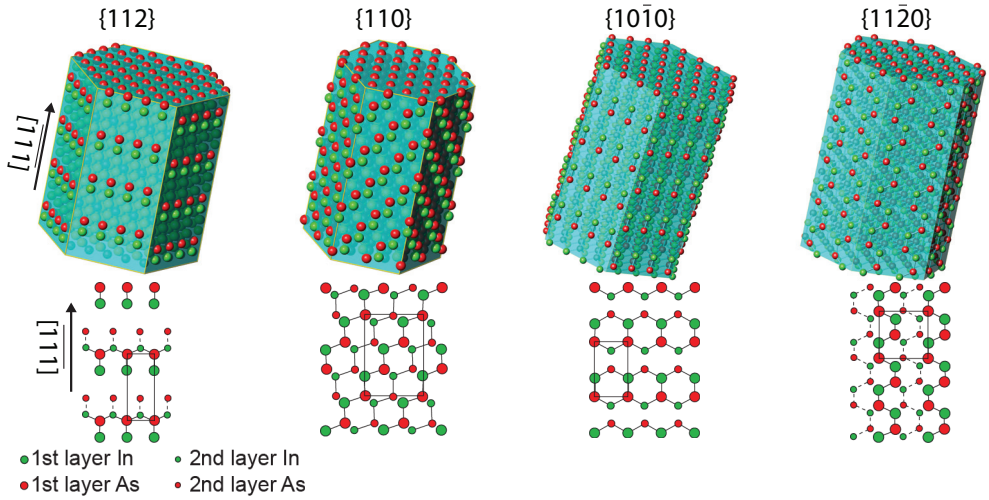

Figure 2.4. Unreconstructed versions of four conventional low-index side facets commonly observed for Zb and Wz III–V NWs as demonstrated for the InAs material system. Top shows models of hexagonal NWs terminated by one type of crystal facets only. Bottom shows the two top-most atomic layers at one side facet.

The {110} terminated facet shows rows of atoms extending along the surface at 35.4 ° angle to the growth direction. {110}-type facets are the by far most studied III–V surfaces since they have been found to be unreconstructed, without surface states in the energy band gap, and can be obtained *in vacuo* by cleaving (001) oriented wafers[42]. The {112} and the corresponding Wz facet {10–10} both show rows of atoms extending perpendicular to the NW growth axis and, in difference to the {110}, show a very open structure. The {11–20} shows a zigzag pattern of the outermost atoms extending along the NW. In addition to these facets it has commonly been seen that Zb NWs can be grown in a periodically twinned fashion[37, 43] with large scale <112> oriented sidewalls, terminated by {111}A and {111}B micro facets, called rotationally twinned Zb or twinplane superlattice (TPS or TSL).

2.3 Overgrowth and facet orientation

When growing axially stacked segments of different crystal structures, two different growth modes have been observed. First, the new NW material that precipitates directly under the Au-particle, resulting in a layer-by-layer mode. Secondly, under certain growth conditions there can also be incorporation of material from the gas-phase directly onto the NW side facets giving a so called overgrowth, resembling conventional thin film

epitaxy. Such an overgrowth is decoupled from the influence of the Auparticle and occurs simultaneously for all NW segments. For all undoped, crystal structure engineered NWs investigated in this work, Wz and Zb facets formed during overgrowth are expected to have comparable properties since they are grown under identical settings (in difference to the Au-catalyzed growth where at least one parameter is changed to induce the different crystal structures, e.g. group V flow). This allows studies of electronic differences between Wz and Zb with as little influence as possible of growth related variations.

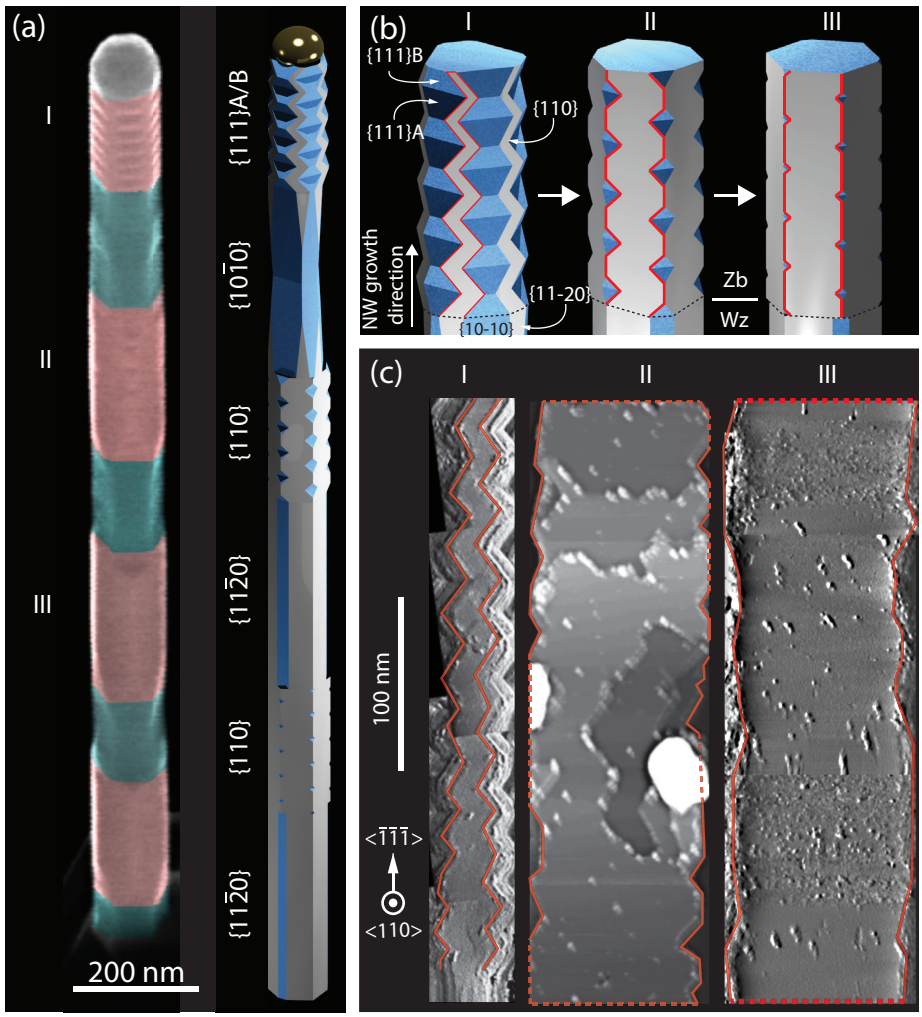

Figure 2.5. Overgrowth of NW facets in the InAs material system. (a) 30 ° tilted SEM micrograph depicting an InAs NW with axial stacking of Wz (green) and Zb (red) segments as also shown in the 3D-model where overgrown facets are colored gray. For ease of viewing, the bottom most Wz and Zb segments are not shown in the model. Dominating surface terminations are shown in the model. (b) Illustration of the overgrowth of Zb twinplane superlattice InAs displaying original {111}A/B facets (blue) and overgrown {110} facets (gray). (c) STM images of the {110} facet at the positions marked I, II, and III in (a). V_T = –1.6 V, I_t = 100 pA for I and V_T = –1.0 V, I_t = 50 pA for II, and III.

In Figure 2.5, an example of overgrowth of an InAs NW with axially stacked segments of Wz and Zb is depicted. A NW was grown with multiple stacking of Wz and Zb segments, where each Zb segment was grown as a TPS and the Wz was terminated by {10–10} facets. As growth continued, overgrowth occurred, gradually transforming the

TPS into {110} facets, as seen in Figure 2.5(b). The top most Zb segment was only exposed to the growth material for a short time and the overgrowth was limited which can be seen in the model in Figure 2.5(a) as well as in the STM image in Figure 2.5(c). As the Zb segment was exposed to growth materials for a longer time (segment II, and III, in Figure 2.5) the overgrowth progressed and at segment III, only weak signs of the zigzag edges stemming from the underlying TPS could be seen.

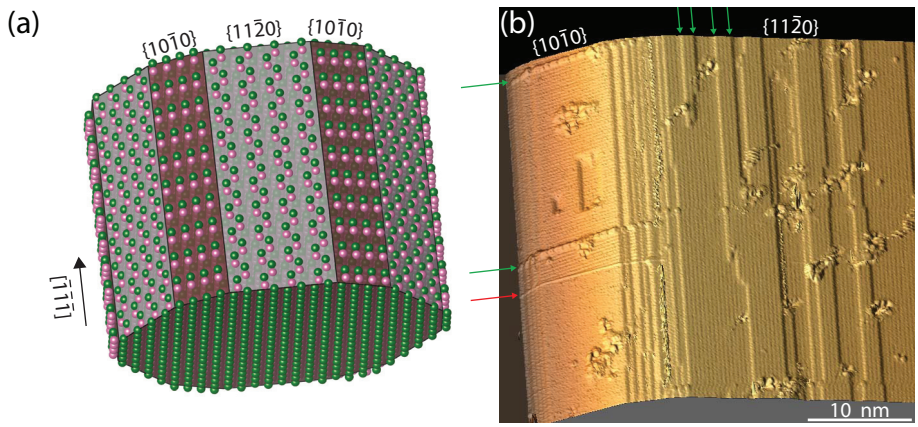

Figure 2.6. Overgrowth at a Wz facet as observed on an InAs NW. (a) Schematic model of a short InAs NW segment with facet types indicated in the figure. Green spheres depict In-atoms and pink spheres depict As-atoms. (b) 3D rendered STM image as obtained from a Wz InAs NW segment after substantial overgrowth of the original {10–10} facet into {11–20} type facets. The inclined, non-overgrown {10–10} facet is seen to be about 10 nm wide. Green arrows denote placement of some atomic steps on the different facets. At the red arrow tip conditions changed slightly resulting in better resolution on the inclined facet. V_T = –1.5 V, I_t = 50 pA, image acquired at 5 K.

At the interface between the {111} terminated TPS and the {10–10} terminated Wz segment, nucleation of {11–20} facets occur, leading to an overgrowth of the Wz segment. The overgrowth leads to a 30 ° facet rotation as exemplified in Figure 2.6, where STM was used to image two side facets on a Wz InAs NW segment. In the figure, it can be seen that the {10–10} facet is almost completely overgrown into {11–20} type facets. Interestingly, it is also possible to study the step morphology, which is facet dependent. At the {10–10} facet, steps seem to be preferentially ordered perpendicularly to the NW growth direction whereas they are mainly oriented along the NW growth direction at the {11–20} facet. Similar results were also found on Wz GaAs NWs[44]. The difference is probably related to varying diffusion lengths of growth material at these facets which is long perpendicular to the NW growth direction for {10–10} facet and long along the NW growth direction for the {11–20} facet[45, 46].

Complicating things a bit more, it is possible to study Wz-Zb interfaces of NWs having an axial stacking of Zb and Wz segments. Knowledge of the geometrical relationship between the different low-index facets is essential in order to make a reasonable interpretation of experimental data.

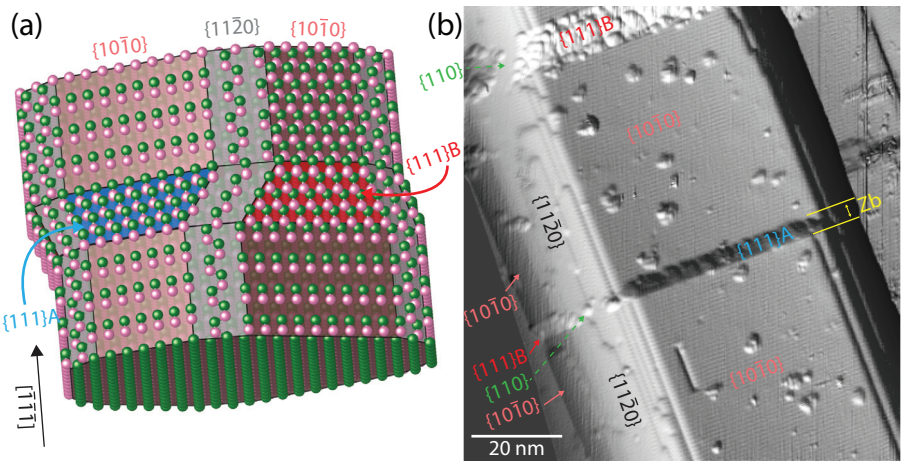

Figure 2.7. Geometry relationship for various low-index side facets commonly observed for NWs. (a) Model depicting a NW with a small Zb segment in a Wz matrix with low-index facets visualized. Please note that the {111}A facet is inclined "downwards" whereas the {111}B is inclined "upwards". Green spheres depict In-atoms and pink spheres depict As-atoms. (b) STM image depicting a Wz InAs NW grown with small Zb segments obtained at 5 K. In the image, it is possible to see two Zb segments. Facet termination is indicated as in (a). V_T = –2.7 V, I_t = 50 pA.

The geometrical relationship between the various low-index facets can be seen in the STM image in Figure 2.7, where an InAs NW with small segments of Zb crystal structure were grown in an InAs Wz matrix. From Figure 2.7(b), it can be seen how the {10–10} and the {111}A/B facets can be accessed from atop. The small {111}A terminated segment is seen to have a downward slope (moving up the NW), whereas the {111}B facet is having an upward slope. The {11–20} facet can be found at a 30 ° inclined side wall as is also shown in the model. Interestingly, the Zb segment found at the 30 ° inclined side walls exposes {110} facets. It is therefore, at least in principle, possible to access both {11–20} and {110} facets without moving across any surface steps enabling studies of e.g. surface relaxations. Rotating an additional 30 ° down from the {11–20} facet, the {10–10} facet is repeated but here the polarity of the Zb {111} surface is reversed (from A to B or vice versa).

2.4 Electronic effects of crystal structure engineering

The electronic structure of a semiconductor is derived from its crystal symmetry and variations in the atomic stacking sequence such as going from Zb to Wz will therefore inevitably change the electronic band structure. Due to the similarities in between Wz and Zb crystal structure where 9 out of 12 neighbors for every atom in the Wz structure are the same in Zb, the electronic properties are expected to be relatively similar.

Theoretical calculations of the electronic properties of III–V polytypes have been performed by several groups[47-51], but experimental confirmation is often lacking since many of the experiments have been performed on (somewhat) faulted NWs where it is hard to deduce the properties of pure crystal structures. Generally, III–Vs in Wz form have been calculated to have a slightly larger band gap energy than in Zb[47]. Exception to this is GaP which shows a smaller, but also direct, band gap when in Wz form[47].

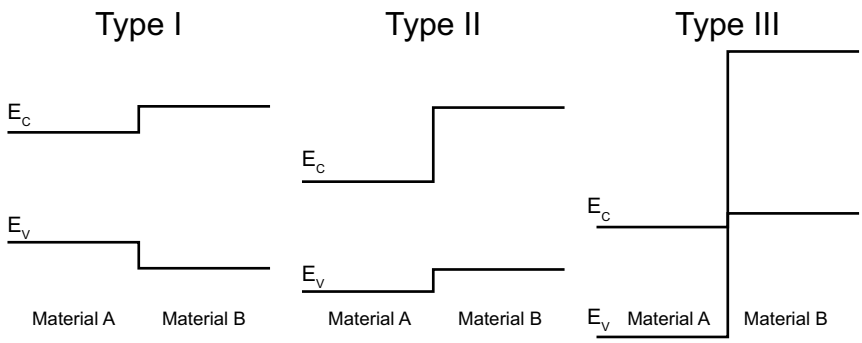

Figure 2.8. Band alignments between two materials (A and B) are shown. For a type I band alignment the valence and conduction band edges are symmetrically aligned, but not for a type II alignment (staggered). For a type III alignment (broken) the valence band edge of one material is above the conduction band edge for the other.

For NWs as the one in Figure 2.7 with axial stacking of Wz and Zb segments the alignment of the bands at the interfaces become important. Band offsets at Wz-Zb interfaces are similar to what has been found for junctions in material heterostructures, Figure 2.8[47-49]. Band offsets are classified as one of the cases shown in Figure 2.8, and Belabbes *et al.* showed that all III–V materials (except GaP) should experience a type II staggered band alignment between Wz and Zb, where Zb is at more negative energies[47]. The offsets may form energy barriers for electrons and/or holes and may even be used to tailor homomaterial crystal structure quantum dots by repeated switching between Wz and Zb. It should be mentioned that the exact ordering of the bands in most

of the III–V systems have been under debate and clear experimental evidence is often missing at this date.

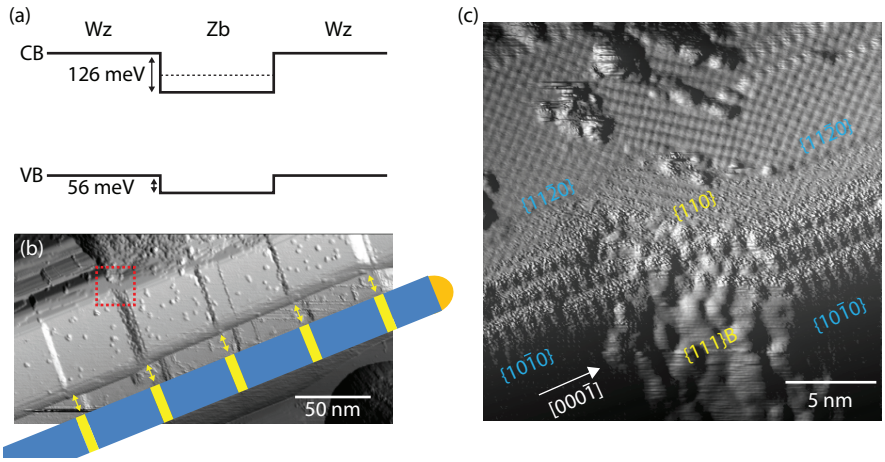

Figure 2.9. Example of crystal quantum dots in an InAs NW. (a) Schematic of an InAs crystal QD with band offsets from Reference [47]. The dashed line represents a bound state whose energy position in the potential well is determined by its size. (b) STM image depicting a Wz InAs NW with Zb crystal QDs at positions marked by the yellow arrows. NW is seen with {10–10} facets facing upwards. V_T = –2.7 V, I_t = 50 pA. (c) Close-up of the red square in (b) showing the QD as observed at the {110}-{11–20} surface. Facet types are indicated in the figure and shown in yellow, and blue for Zb and Wz, respectively. In the bottom of the image the {10–10} facet can be seen where the QD is terminated by a small {111}B type facet having a rough surface. V_T = –2.6 V, I_t = 50 pA. STM images were obtained at 5 K.

With the advent of sharp crystal phase switching during growth it has now become possible to grow crystal phase quantum dots where the same material is grown in one phase (e.g. Zb) in a matrix of another phase (e.g. Wz)[21, 40, 52-54]. In Figure 2.9, InAs NWs with Zb quantum dots of varying sizes were grown in an otherwise Wz NW. From the expected band alignment shown in Figure 2.9(a), bound states can arise in the conduction band of the Zb quantum dot, where the energetic position of the bound state depends on the dot size. In Figure 2.9(c), an atomically resolved STM image obtained at 5 K depicting the QD as seen at the {11–20}-{110}-{11–20} facet can be seen.

2.5 Doping of nanowires

Doping is a fundamental prerequisite for most semiconductor device applications and relies on the introduction of small amounts of electrically active impurities into the crystal

lattice. For NWs, this can be realized by introducing low amounts of dopant precursors during growth, so called *in situ* doping. Doping of NWs is a challenging task since the dopants can be incorporated both via the Au-particle and via incorporation on the NW sidewalls directly from the gas-phase. NW doping has nevertheless proved to be very useful and devices such as pn-junctions[39, 55], Esaki-diodes[9, 56, 57], solar cells[5, 11], field-effect transistors[3, 8], and photodetectors[58] have been presented.

Not only is it a major challenge to dope the NWs but even more, the detection of the introduced impurities is far from trivial. Typical bulk methods such as secondary ion mass spectroscopy (SIMS) are not applicable for NWs due to their small volume. Several different ways to detect dopants, either measuring the impurity concentration or by measuring the charge carrier concentration have been explored. The most used method is to contact NWs and use them in a device configuration which demands additional processing, and several assumptions on device geometry must be made[59].

For the work presented in this dissertation, I have explored two novel methods of determining the charge carrier concentration in doped NWs, STM/S and XPEEM. Both methods can be used to study clean NWs and no additional processing is needed. STM/S has the major advantage of being capable of spatially resolving individual dopants on NW surfaces and to map electronic structure down to the atomic scale. On the other hand, the technique is slow and interpretation of the results is not always straight forward. Secondary electron XPEEM is a fast technique with a spatial resolution in the tens of nanometer range.

2.6 Transfer

In order to obtain information about the surface side facets of the NWs there is a need to transfer the as-grown free standing NWs onto a new substrate, thereby exposing the sides and enabling surface sensitive probes, such as STM, LEEM/PEEM and XPS, to reveal the surface structure and its electronic and chemical properties. There are several different requirements on the transferred NWs, and thus the transfer process, depending on which analysis technique is to be used. The most important ones, that I have recognized, are described below.

The transfer process must not introduce any contaminants e.g. in the form of crystal fragments from the growth substrates or in the form of residues of transfer material. Minimizing the amount of crystal fragments from the growth substrate is especially important in XPS experiments since NWs are often grown on wafers of the same material as the NWs. A large amount of fragments would lead to contamination peaks which might overlap and hide the NW signal and lead to misinterpretation. Contaminants of atomic species other than the NWs' constituents would be easily detectable in XPS and,

depending on the study, might not be as troublesome. Contaminants placed on NWs could, however, change the NW surface chemistry and electronic properties and should therefore be avoided. In STM experiments the restriction regarding growth substrate crystal fragments is not as strict. It is in most cases easy to distinguish between a crystal fragment and a well-defined NW. Residuals from the transfer process could be a problem during STM if scanned upon, since it would alter the tunneling conditions and risk a tip crash. Solvent residuals from solution dispersed NWs could also act to change the surface conditions by e.g. surface carbon contamination, or altered surface chemistry.

Secondly, the transfer process should leave NWs broken off at the base and without fragmenting the NWs. This is of paramount importance when examining NW heterostructures that have interesting features in different axial positions along the NW. Since heterostructures often experience strain accumulation at interfaces between different crystal structures or composition[16, 60], it is not always trivial to avoid fragmenting NWs.

The third need deals with the placement of the NWs after the transfer process. From an STM point of view, it would be impractical to analyze bundles of NWs since these might become several μm high and therefore risk tip crashes. Well dispersed NWs of sufficient density are therefore most often preferred as it would give good signal count in XPS and short search times for NWs in STM.

Two different transfer methods have been utilized in the work leading up to this dissertation. In the first method, a clean room wipe was used to gently scrape the surface of the growth substrate in order to pick up some of the NWs. The wipe was then pushed onto the new substrate resulting in a transfer of NWs. The clean room paper transfer was found to give reasonable coverage of NWs on the sample but with extensive NW fragmentation and bundling. The clean room wipe method was mainly used for LEEM/PEEM studies.

In the second method, the growth substrate with the standing NWs was placed in mechanical contact with the new substrate. As they were in contact a gentle pressure was applied to the new substrate resulting in NW break off and transfer. This technique limits the risk of contamination to that of unwanted crystal fragments since no external contamination sources were used (such as a clean room wipe or solvents).

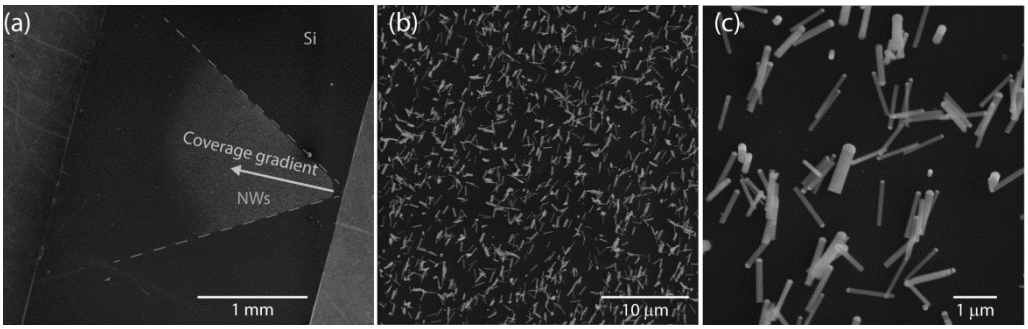

Figure 2.10. SEM micrograph of contact deposited InP NWs onto a Si substrate. (a) Overview image showing the deposited area. The dashed gray lines show where the growth substrate with NWs was placed. An uneven pressure was applied in order to obtain a coverage gradient on the Si wafer as seen by a darkening of the NW area. White arrow points toward lower NW coverage. In (b) NWs in the high coverage area can be seen. (c) Zoom in of the area in (b) showing the Au-particle still residing on top of the NWs.

Typical results from the contact deposition are shown in Figure 2.10 with high density of transferred NWs in a well-defined area. A higher density on the growth substrate was also seen to give a higher density of transferred NWs, as would be expected. For very high NW growth coverage (> 4 μm^{-2}) an increased bundling of transferred NWs was observed, which obstructed STM measurements. By applying an uneven pressure during transfer, a coverage gradient on the transferred substrate could be obtained and NW bundles could therefore be avoided during STM measurements, see Figure 2.10(a).

Even though the contact transfer can be thought of as rather crude regarding the mechanical contact, only spurious contaminating crystal fragments were found among the transferred NWs. From SEM it was often seen that the NWs were (mainly) broken off at the base and with the catalyzing Au-particle still residing on the NW top indicative of a gentle transfer process. NW fragmentation was mainly a problem close to the edge of the transferred area. Interestingly, despite the mechanical contact, the method was found to be able to transfer NWs onto 50 nm thin silicon nitride membranes without observable damage neither to the membranes nor to the NWs. The high coverage, low amount of bundling, and lack of contaminating species showed that the contact transfer was an excellent technique to transfer free standing NWs onto new substrates for STM and XPS studies.

The NWs were transferred to different substrates depending on the type of experiment to be performed. For STM analysis the NWs were transferred onto a substrate made from the same material as the NWs, i.e. InAs NWs on InAs substrates, in order to ensure similar conductivity, and similar surface oxides. During a deoxidation step where the native oxides on the NWs were removed, the substrate was used as a quick reference to gain information about possible deoxidation problems, Section 2.7.

For XPS analysis the NWs were transferred to well-characterized, highly doped HF-etched Si wafers. Using the same Si-wafer for all experiments, the well-studied Si*2p* peak was used as an energy reference level. Ideally, one would use a Fermi edge as calibration for the energy scale, but that is only well-defined for metals. However, most metals are incompatible with the native oxide removal since they can alloy or react with the NWs.

2.7 Native oxide removal

All III–V semiconductors, as well as most other materials, oxidize when exposed to the ambient resulting in a 1–2 nm thick layer of native oxide. These oxides impose great problems from a surface science point of view since the examined surface would be that of the oxide rather than the (interesting) semiconductor. Further, the often insulating nature of the oxides makes them incompatible with STM/S which requires a conductive sample.

Several routes exist for the removal of surface oxides. Oxide removal using Ar ion sputtering has been employed with great success for cleaning of metal crystals. After sputtering, the samples are typically annealed to reduce surface roughening, remove trapped Ar, and ensure high surface crystal quality. For III–Vs it has been found challenging to anneal away defects making sputtering a poor choice. Thermal cleaning where the sample is heated in UHV has been one conventional way to desorb oxides and surface contaminants on semiconductor substrates. Thermal desorption is, however, not applicable to most of the III–V materials since the oxide desorption temperature is usually much higher than the congruent evaporation temperature. That is, the temperature where the group V constituent preferentially desorbs and droplets of the group III material form on the surface. Formation of group III droplets not only changes the surface stoichiometry, but metallic particles can affect the surface electronic structure several nanometers away, thus complicating electronic structure mapping using STS, PEEM, or XPS. As an example, for InP the oxide desorption temperature is 480-530 °C[61, 62], whereas the congruent evaporation temperature is reported to be 363 °C[63].

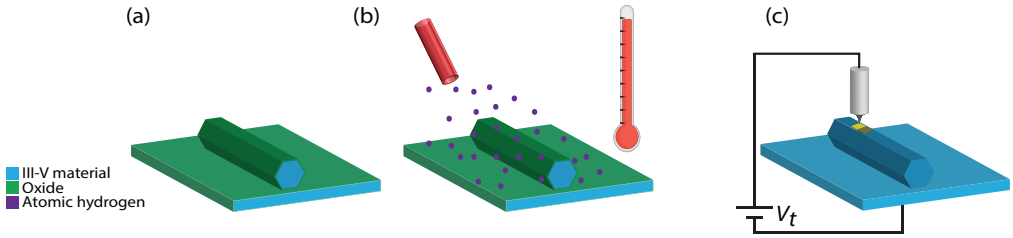

Figure 2.11. Schematic description of the atomic hydrogen cleaning process. (a) Oxidized NWs are broken off onto a III–V wafer. (b) NWs are annealed in atomic hydrogen atmosphere in order to remove the native oxide. (c) Surface science experiments can be performed, such as approaching an STM tip (light gray) to scan the NW side facets with sample bias V_t. Please note that the native oxide thickness is not drawn to scale.

The cleaning temperature can be lowered significantly if one, together with the elevated temperature, exposes the sample to a flow of atomic hydrogen as is illustrated in Figure 2.11[44, 64-66]. Hydrogen gas can be introduced into the preparation chamber through a leak valve and thermally cracked at around 2000 °C to atomic hydrogen (H^*). The thermally cracked hydrogen radicals have very low kinetic energies, typically less than 1 eV, which limits the interaction of the H^* to the surface layer[67], and should not be incorporated into the NWs. In the case of InP, the H^* is thought to react with the stable In oxide, In_2O_3, and produce the more volatile In_2O[68] which desorbs at low temperatures. Fairly high temperatures are however needed for full cleaning due to the removal of hydrocarbons and $In(PO_3)_3$ which persist at temperatures up to 400 °C[61].

Several different atomic hydrogen sources have been used in this work, all with the same principle of thermally cracking hydrogen gas into atomic hydrogen in either a heated W tube or by flowing hydrogen gas around a heated W filament. The pressure during the atomic hydrogen treatment was typically on the order of 10^{-6} mbar. Care should be taken to ensure that the temperature of the heated W tube/filament does not exceed 2000 °C, since otherwise the vapor pressure of W quickly goes up to 10^{-7} mbar resulting in deposition of small W clusters on the sample. After successful deoxidation, the sample was kept at elevated temperatures for some minutes after closing to the hydrogen gas in order to desorb possible adsorbed hydrogen.

	InAs	GaAs	InP
Temperature [°C]	340–400	500–600	400
Cleaning time [min]	35	35	20–50

Table 2.1. Temperatures and times needed for successful oxide removal on the different NW materials when using an atomic hydrogen pressure of $2x10^{-6}$ mbar and a hydrogen source heated to approximately 1900 °C.

In Table 2.1, times and temperatures for successful cleaning of NWs of different III–V materials are depicted. The higher cleaning temperature for GaAs compared to InAs resides from the higher decomposition temperatures of Ga-oxides whereas the cleaning of InP is limited by the removal of $In(PO_3)_3$[62].

For STM/S, an experimental session could last for several weeks using the same sample and successful STM/S could be performed for up to one week without noticeable contamination. If the experiment kept running, the surfaces could be refreshed using a 5 min hydrogen cleaning. For STM, the substrate around the NWs was used as a first control of the success of the sample cleaning. A clean substrate (originally covered in epi-ready oxides) does not necessarily mean that the NWs (that had a native oxide) were clean. A non-clean substrate, on the other hand, indicated errors in the cleaning, e.g. contamination of the hydrogen gas. Please note that if the shutter to the hydrogen source was closed during cleaning, no successful deoxidation was observed, confirming the necessity of atomic hydrogen for successful oxide removal at the chosen temperatures. For LEEM/PEEM experiments, sample cleanliness was determined either by the existence of a μLEED-pattern or by the absence of oxide-related peaks in core-level photoeelectron spectroscopy.

3. Scanning tunneling microscopy

The STM relies on quantum mechanical tunneling of electrons between a conductive sample and a conductive (usually metallic) tip to study surfaces of solids. Since its invention in 1982 by Binnig, Gerber, Rohrer, and Weibel[69, 70] it has revolutionized the world of surface science due to its excellent capabilities to image individual atoms and individual localized electronic states.

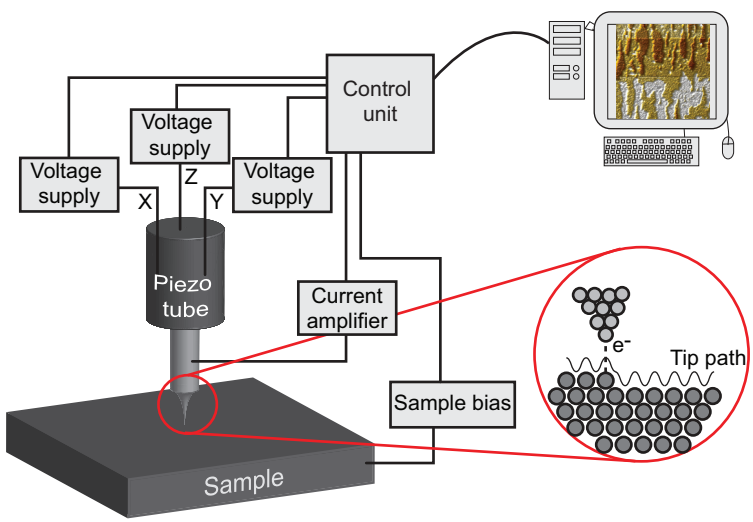

Figure 3.1. Schematic setup of a scanning tunneling microscope. An atomically sharp metallic tip is brought within 10 Å of a conducting sample and a bias is applied between tip and sample enabling electrons to tunnel. The tip height is adjusted to maintain the tunneling current at a fixed value. An image is formed depicting the z-piezo extension over the scanned surface.

In the microscope itself an atomically sharp metal tip, typically an electrochemically etched W-tip, is brought close (around 10 Å) to a conductive sample, Figure 3.1. A bias is applied between the sample and tip (sample bias, V_T) which induces a tunneling current

(I_t) often in the order of pA–nA. In the most common way to operate an STM, the constant current mode, the tip is scanned over an area of interest while the tunneling current is kept constant using a feedback loop. In order to keep the tunneling current at a fixed value, the height of the tip is adjusted using a piezo crystal which changes in size if a bias is applied. The height displacement at every point is converted into a color scale forming the STM image which is a convolution of the electronic structure of the tip and surface.

In the simplest approximation, the tunneling current is seen as one-dimensional tunneling across a vacuum barrier (corresponding to the tip–sample separation) leading to an exponential dependence of the tunneling current, I_t, on the vacuum barrier (tip–sample separation), s[70]:

$$I_t \propto \exp(-2\kappa s)$$

where κ is the inverse electron decay rate, which in turn is dependent on the sample bias. As a rule of thumb, a change in tip–sample separation by 1 Å induces an order of magnitude change in the tunneling current, for a work function of 4 eV. The exponential dependence of the tunneling current on the tip–sample separation ensures the sub-Ångström vertical resolution in the STM. In addition, since the tunneling current mainly originates from the outermost tip atom which interacts with the outermost surface atom, very high lateral resolution is inherent.

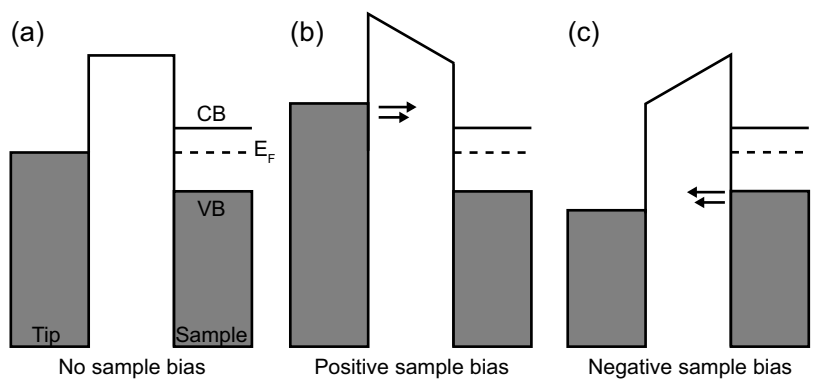

Figure 3.2. Schematic view of the tip–sample interaction and direction of tunneling currents under different sample biases. Conduction band (*CB*), valence band (*VB*), and the Fermi level (E_F) are marked in the figure.

The polarity of the sample bias determines the direction of electron flow as depicted in Figure 3.2. If a positive bias is applied to the sample, electrons tunnel from electronic states in the tip to empty states in the sample valence band, known as empty states

imaging, Figure 3.2(b). Applying a negative sample bias makes electrons tunnel from states in the sample conduction band into empty tip states, filled states imaging, Figure 3.2(c).

3.1 STM on nanowires

Most STMs have been designed to scan on very flat samples, and height differences of more than a couple of nanometers are, by most users, considered challenging. To scan on NWs that are lying down with heights up to several hundreds of nm therefore demands extra attention from the operator. It is often necessary to use a rather low tunneling current (large tip–sample separation), fast feedback, slow scan speed, and to have an STM with a large z-piezo range in order to avoid crashing the tip into the NWs. There is also a strong need to keep track of the tip sharpness since it might greatly influence the images.

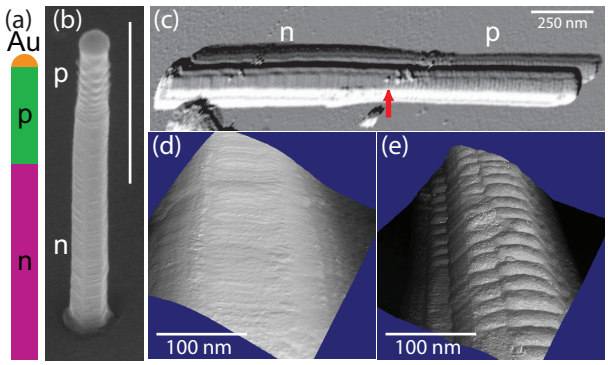

Figure 3.3. Large scale imaging of a NW using STM. (a) Schematic representation of the studied sample. An axial pn-junction NW made of InP, for more details, see Paper III. (b) 30 ° tilted view SEM micrograph of the sample. Scale bar denotes 500 nm. (c) STM image of a broken off, hydrogen cleaned NW lying flat on an InP(111)B substrate, V_T = –3.0 V. Red arrow marks the epitaxial pn-junction. The image has been differentiated for ease of viewing. (d) 3D visualization of the n-type segment, V_T = –3.0 V. (e) 3D visualization of the p-type segment, V_T = –3.0 V.

In Figure 3.3, STM overview images depicting an InP NW lying on an InP substrate can be seen. Due to the large height (diameter) of the NW of 80 nm, it is not surprising that multiple-tip effects can be seen in the form of "extra" NWs in close proximity to the investigated one. Just above the InP NW a second NW can be seen in Figure 3.3(c) having the same structure and features as the bottom one, and is an artifact from the tip having a finite width.

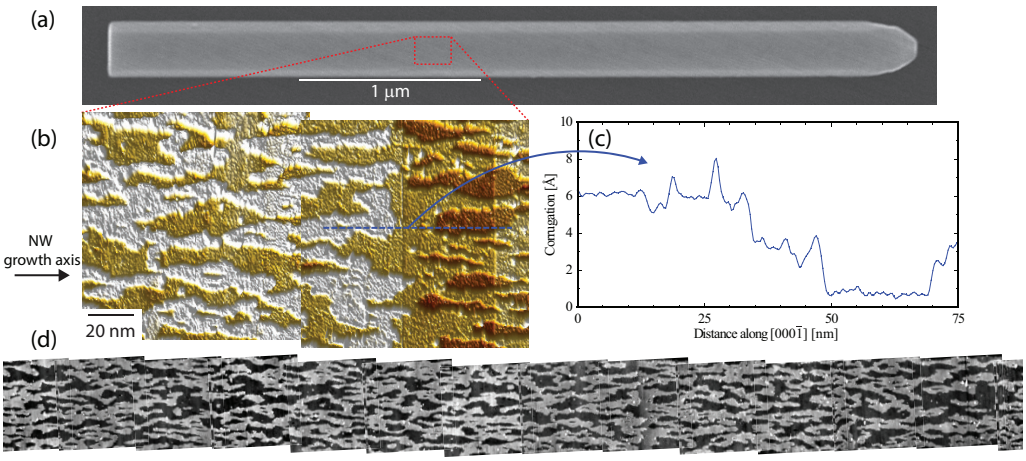

Figure 3.4. Large scale imaging on a Au-free grown InAs NW. (a) SEM image depicting an InAs NW grown without the use of Au-catalyst particle after STM measurement. (b) STM micrograph showing a part of one of the side facets. (c) Line scan along the dashed red line in (b) showing monolayer step height of the winding pattern. (d) Several images as the one in (b) depicting the axial evolution of the surface morphology along the NW growth direction. Each image is 100x100 nm^2. Settings for all STM images: V_T = –2.5 V, I_t = 80 pA.

Once on top of a NW the surface is most often smooth and well suited for STM, allowing higher scan speeds and larger currents, much like in conventional STM. In order to minimize the tip-movement in each scan line (and thereby lower the risk of tip crashes), it is recommended to image one side facet only. In Figure 3.4, STM images from one of the side facets of an InAs NW grown without the use of Au-catalyst particle can be seen. By making sure to not "fall off" the sides, the corrugation can be kept < 1 nm which is usually considered safe for the tip. By scanning along a NW, mapping the axial surface evolution, it is possible to keep monolayer step resolution over several micrometers along individual NWs, Figure 3.4(d), while maintaining reasonable scan speed, for more details see Paper VIII.

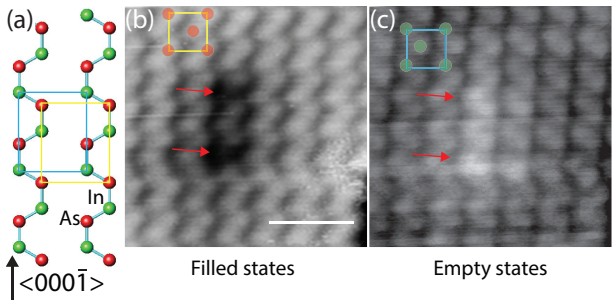

Figure 3.5. (a) Atomic scale structure of an unreconstructed InAs{11–20} surface depicting the top-most position of As- (red spheres) and In-atoms (green spheres). (b) Image obtained using negative bias (probing filled states, As atoms). V_T = –1.7 V, I_t = 80 pA. (c) Image of exactly the same area obtained using positive sample bias (probing empty states, In atoms). V_T = +1.8 V, I_t = 80 pA. The red arrows in (b) mark two As vacancies and can be seen as slight protrusions of the In-atoms in (c). Scale bars denote 1 nm.

It has previously been reported, for several of the low index III–V surfaces, that the empty states are mainly centered at the dangling bonds of the group III-atoms and the filled states are at the group V-atoms[44, 65, 71, 72]. By switching the sample bias one can therefore choose which atoms to image and utilize elemental specific STM. In Figure 3.5 I present filled and empty states images obtained at an InAs{11–20} surface at the Au-free NWs in Figure 3.4 depicting As- and In-atoms, respectively. Interestingly, at the place of two As-vacancies a corresponding protrusion of the In-atoms can be seen. Similar behavior was also seen for Wz GaAs NWs in Paper II.

All room temperature STM images presented in this dissertation were obtained using an Omicron variable temperature XA STM working at a base pressure $<10^{-10}$ mbar. Additional low temperature STM (at 5 K) was performed at the Center for Functional Nanomaterials, Brookhaven National Laboratory in New York, using a Createc STM.

3.2 Atomic scale imaging

When imaging large objects (nanometer scale corrugation), topography dominates over electronic contrast and STM images can, most often, be seen as direct representations of the samples' morphology, cf. Figure 3.2 and 3.3. When imaging on the smaller scale, however, the electronic properties of the sample (and the tip) need to be considered in order to determine features seen in the images. The physics behind was found to be a most intriguing problem as was stated already in 1982 by Binnig and Rohrer[69]:

> "The STM graphs are not simply reproductions of the surface-atom corrugation. They rather reflect the corrugation of the electron wave functions near the Fermi level, roughly in the middle of the vacuum gap. To make a quantitative connection with the corrugation of the surface cores, a detailed tunnel theory on the atomic scale is required,…"

Using Bardeen's formalism, Tersoff and Hamann formulated a description of the tunneling current using perturbation theory[73]: The tip and sample were first modeled as independent systems, and the tunneling corresponds to transition of charge from a certain state in one system into a certain state in another system. The tunneling current from the tip to sample, *I*, can then be expressed as:

$$I = \left(\frac{2\pi e}{\hbar}\right)\sum_{\mu,\nu} f\left(E_\mu^t\right)[1 - f(E_\nu^s + eV_T)]\left|M_{\mu\nu}\right|^2 \delta\left(E_\mu^t - E_\nu^s\right)$$

where E_μ and E_ν are the energies of the states ψ_μ and ψ_ν of the sample and tip, respectively. *f(E)* is the Fermi distribution function and $M_{\mu\nu}$ is the transition matrix element for tunneling in between a state in the tip and a state in the sample. For computational simplicity, the delta function is used which ensures that only elastic tunneling is considered and tip–sample interactions generating phonons, plasmons, and other losses are ignored. The Fermi distributions imply that tunneling only occurs from occupied states into empty ones. The transition matrix element was parameterized as an integral over an arbitrary plane, *S*, between the two subsystems as shown by Bardeen to be[74]:

$$M_{\mu\nu} = -\frac{\hbar^2}{2m}\int \left(\psi_\mu^{t^*}\nabla\psi_\nu^s - \psi_\nu^s\nabla\psi_\mu^{t^*}\right)\cdot d\vec{S}$$

In order to calculate the tunneling current one needs to know the wave functions of the tip and sample (to calculate *M*). These parameters are however most often not known and several assumptions must be made. Tersoff and Hamann assumed a "perfect" tip with spherical apex, geometrically and electronically isotropic, with s-like wave functions dominating the tunneling current, and operated in low temperature[75]. With this model the tunneling current is shown to be proportional to the integrated local density of states (LDOS) at the Fermi level up to $E_F + eV_T$ at the position r_0 of the tip:

$$I \propto \rho_t \int_0^{eV_T} \rho_{s,loc}\left(\vec{r_0}, E_F + \varepsilon\right)d\varepsilon$$

where ρ_t is the LDOS for the outermost tip atom (approximated as constant) and $\rho_{s,loc}(r,E)$ is the sample surface LDOS at the position *r* and energy *E*. The exponential decay of the tunneling current with distance is not as easy to distinguish anymore but can, approximately, be seen through the exponential decay of the sample LDOS into vacuum.

In reality few tips satisfy the conditions of a "perfect" tip. Chen has even shown theoretically that for some investigated surfaces the observed resolution can only come from tips with specific wave functions of higher angular momentum, l [76]. Several groups have also reported an observed increase in resolution using functionalized tips where e.g hydrogen or deuterium is confined in the tunneling junction[77-79]. In Paper VIII, I could observe how a small (reversible) tip-change resulted in an observed zigzag pattern at the InAs{11–20} surface (for a symmetric tip) or a square pattern (for an assymetric tip), as also shown in Figure 3.6. When observing a square pattern, the higher intensity for half the surface atoms arises purely from an increased overlap in the orbitals of tip and sample. It is interesting that this sensitivity to the tip symmetry cannot be observed on defect free III–V {110} surfaces since all dangling bonds are oriented in the same direction on those surfaces. In the bottom part of Figure 3.6(b,c), two small Zb segments with a twin defect can be seen, green arrows. For a symmetric tip, both Zb orientations have similar intensity, Figure 3.6(b), whereas one of the segments is blurred out for an asymmetric tip, Figure 3.6(c), corroborating our model.

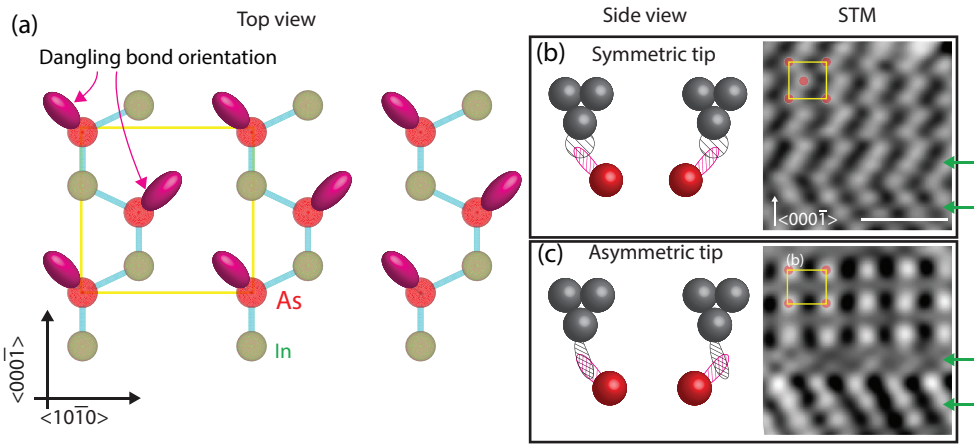

Figure 3.6. Tip symmetry and its effect on the observed STM images at InAs{11–20}. (a) Top view schematic representation of an unreconstructed {11–20} surface with As dangling bond directions marked by the pink ellipses. (b) A tip (gray) with a symmetric, s-like, orbital at the apex gives equal orbital overlap for both dangling bond orientations. The corresponding STM image shows equal intensity for all atoms, and a zigzag-pattern, V_T = –1.8 V, I_t = 80 pA. (c) A tip with asymmetric orbital at the apex gives unequal orbital overlap for the dangling bond orientations. The corresponding STM image shows strong corrugation for half the atoms and thus a square-pattern, V_T = –1.7 V, I_t = 80 pA. Experimental images were acquired at the exact same place. Green arrows in (b,c) mark the positions of two small segments with local Zb stacking. Scale bar denotes 2 nm.

The tip properties have great impact on the way STM experiments are performed. In reality atomic resolution STM is, as most experimentalists are aware of, infrequent and relies on getting the tip to form a stable localized state that interacts with the sample. Every STM operator has his or her own way of achieving this, including scanning at high negative sample bias to achieve migration of tip atoms to get a tip with a single atom at its apex, scanning across moderately high surface steps, or dipping the tip gently down into a noble metal hoping to pick up an atom with a suitable localized state[76].

To interpret STM images correctly it is important to understand that electronic effects play a major role. For simple metals there are most often no strong variations in the LDOS near the Fermi level and STM images are rather constant with V_T, typically showing positions of the outermost atoms. Semiconductors (and oxides) on the other hand experience strong variations of the LDOS with energy and image features often change a lot with V_T and does not necessarily correspond to the surface topography. It is therefore common to obtain images of the same area using several different sample voltages to deduce the role of the electronic structure, so called voltage dependent imaging.

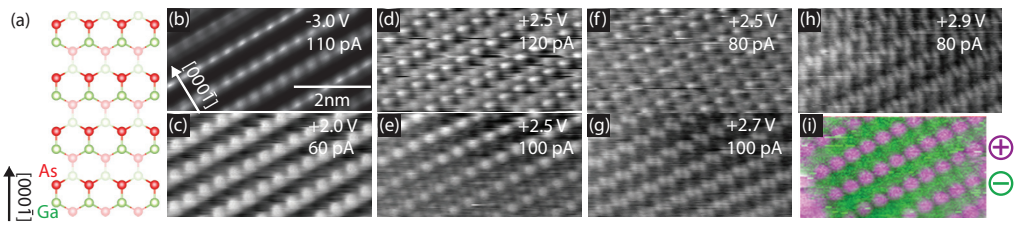

Figure 3.7. Voltage dependent STM imaging on GaAs{10–10}. (a) Model of the 2 topmost layers of an unreconstructed GaAs {10–10} surface. (b) Filled states image of the surface depicted in (a). (c–h) Empty states imaging obtained using V_T and I_t as depicted in each figure. (i) Dual-mode image obtained using sequential switching between empty and filled states imaging. Images obtained using the different polarities have been overlaid where purple color denotes empty states imaging and green is filled states imaging. $V_{T,empty}$ = +2.7 V, $V_{T,filled}$ = –2.9 V. Scale bar in (b) is also valid for (c–i). For details, see Paper II.

In Figure 3.7, voltage dependent atomic scale images as obtained from the GaAs{10–10} surface over a large sample bias range are presented. At negative sample bias (filled states), images as Figure 3.7(b) were obtained with a pattern depicting the positions of the top-most As-atoms, no qualitative differences with bias was observed. On the other hand, at positive sample bias (empty states), the appearance was very much dependent on settings. When imaging very close to the conduction band edge, Figure 3.7(c), a pattern similar to the one obtained at negative bias was seen presumably depicting the top-most Ga-atoms. At higher positive bias, Figure 3.7(d–f), I noticed the appearance of features in between the well-defined rows. At even higher positive bias, first a splitting of the spots was seen,

Figure 3.7(g), which then changed into a Y-like shape, Figure 3.7(h). Also at fixed bias, Figure 3.7(d–f), it can be seen that the tunneling current had a major effect on the images.

I also imaged in so called dual-mode where the polarity was switched sequentially when the tip was moved back and forth in the image, thereby forming two images simultaneously with both polarities. In Figure 3.7(i), such an image where I have overlaid the images colored green for negative bias (filled states) and purple for positive bias (empty states) can be seen. From the image one can see that the filled states and the empty states were located at different spatial positions, thus being similar to the GaAs(110) surface where the empty states are mainly centered above the Ga-atoms and the filled states above the As-atoms[72].

Voltage dependent imaging is not always trivial to interpret but in conjunction with advanced *ab initio* modeling using density functional theory (DFT) calculations, the observed patterns can be explained. In Paper I, this combination of calculations and voltage dependent imaging in order to study two Wz InAs surfaces, {10–10} and {11–20}, was used.

4. Scanning tunneling spectroscopy

STS is a powerful technique in which one is able to determine the electronic surface properties of a material with atomic precision[80]. In this dissertation, only STS on semiconductor materials will be considered. The principle behind the method is, as with the STM, rather straight forward, but the actual measurements are not. Instead, they are rather time consuming since the tip has to be stable over wide bias ranges and long times. The basic idea is to place the STM tip in an area of interest, disengage the feedback loop, to keep the tip at fixed tip–sample separation, and scan the sample bias while the tunneling current is recorded. The results are current-voltage curves (*I-V*-curves), see Figure 4.1, from which the electronic properties of the surface around the Fermi level can be derived.

In addition to sweeping the sample bias and recording the tunneling current it is very useful to also record the differential signal (*dI/dV - V*) since this is related to the local density of states (LDOS) at $E_F + eV_T$ (the tunneling current signal could be seen as an integration of electrons from states at E_F to E_F+eV_T). The differentiated signal can in principle be acquired by numerically differentiating the *I-V*-signal but that also amplifies the noise. Instead, I add a low amplitude, high frequency sinusoidal voltage to the sample bias. The tunneling current is detected and compared to the sinusoidal voltage using a lock-in amplifier and directly gives us the *dI/dV*-signal. One should, however, choose the signal carefully so that it does not interfere with the feedback system of the STM. At every STS point spectrum I obtained both the *I-V* and the *dI/dV - V* curves simultaneously.

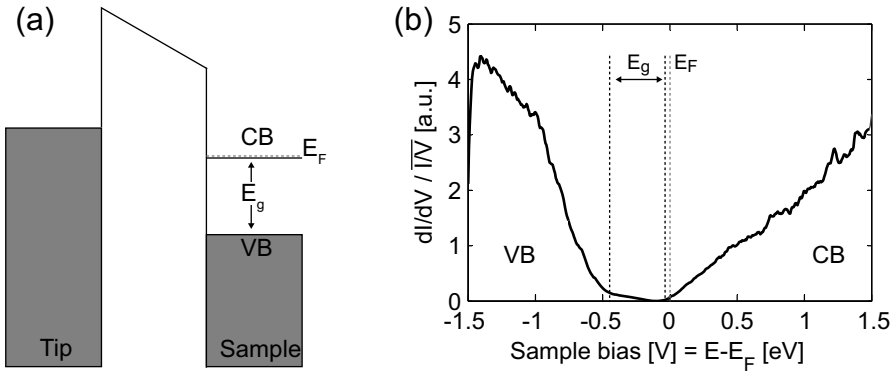

Figure 4.1. (a) Schematic description of the electronic bands in a biased tip close to an n-type semiconducting sample. Valence band (*VB*), conduction band (*CB*), Fermi level (E_F), and band gap (E_g) are marked in the figure. (b) STS *(dI / dV) / (I/V)* spectrum obtained from an InAs{11–20} NW facet. Between approximately –0.5 V and 0 V sample bias the band gap region can be seen with no/low amount of states available for tunneling.

In Figure 4.1, I present a typical STS spectrum depicting the differentiated tunneling current broadened by the total conductance as a function of sample bias. The formation of this quantity, which is proportional to the local density of states (LDOS)[81, 82], will be discussed in detail in Section 4.1 and Section 4.2. In between approximately –1.5 V and –0.5 V, tunneling from valence band states can be seen. At –0.5 V the STS-signal is very low and marks the band gap region. At 0 V sample bias the tip and sample are in equilibrium and the Fermi level is thus found there. At positive sample bias the tunneling current goes up again due to electrons tunneling into empty conduction band states. From the spectrum in Figure 4.1(b) it is apparent that the Fermi level is located close to the conduction band edge (and in fact even in the conduction band) showing the n-type character of the surface. For unpinned surfaces, the position of the band edges with respect to the Fermi level directly shows the charge carrier concentration and type[83].

4.1 Variable-z mode

Spectra are usually obtained over large voltage ranges, leading to very small measured currents at the band edges. To have the possibility of probing the band edges and surface states within the band gap with high accuracy, the spectroscopy acquisition was modified. The STS measurements were performed using a technique called variable-z mode, also known as Feenstra mode. The technique was presented by Mårtensson and Feenstra in 1989 and makes use of a continuously varying tip height while recording the tunneling spectra[84]. The tip is placed at an area of interest and the feedback loop is turned off just

as in a regular STS measurement. While sweeping the voltage in the desired range, the tip–sample separation changes according to the equation below, where a is a displacement factor chosen by the operator, s is the height of the z-piezo, s_0 is the z-piezo height before the measurement, $|V|$ is the absolute value of the sample voltage, and $|V_0|$ is the voltage at the start of STS acquisition, the so called stabilization voltage. A value of a = 2 Å/V was typically used, which indicates that the tip approaches the sample as the voltage becomes smaller.

$$\Delta s(V) = s_0 - a(|V_0| - |V|)$$

The main advantage when working in variable-z mode is a major increase in current resolution at low voltages; Feenstra reports that the conductance can be measured at six orders of magnitude in one single measurement[83]. This is an increase with about 2–3 orders of magnitude compared to STS acquired at fixed tip–sample separation without any increase in acquisition time.

A very elegant way to remove the *dI/dV*-signal's dependence of the tip–sample separation and at the same time forming a quantity that is proportional to the sample LDOS has been shown by normalizing it by the total conductance (I/V), see Figure 4.2[81, 82]. A drawback of this representation is that although it works excellent for metals and small band gap materials; for semiconductors with considerable band gap the ratio $(dI/dV) / (I/V)$ tends to diverge at the band edges due to the fact that the current approaches zero faster than the conductivity. That is, the *I-V*-sweeps give erroneous results in the areas that are most interesting, the band edges, resulting in curves approaching infinity, a highly unrealistic model. Feenstra and Mårtensson showed empirically that the divergence could be worked around if the total conductivity was broadened[85].

The broadening can be performed in several different ways with only minor differences in the presented spectra. The easiest is just to add a small constant to the conductivity. All spectra obtained and presented in this dissertation were broadened by convoluting the total conductivity (I/V) with an exponential function in a manner similar to the one presented by Feenstra[83]:

$$\overline{I/V} = \frac{1}{2\Delta V}\int_{-\infty}^{\infty} \frac{I(V')}{V'} \exp\left(\frac{-|V' - V|}{\Delta V}\right) dV'$$

That is, for any certain voltage V, the broadened conductance is convoluted by an infinite voltage integral, weighted around the respective voltage by an exponential function with given width ΔV. In reality this is performed by translating the integral into a summation. Since the integral boundaries are infinite, it was assumed that the current occurring for the lowest (highest) voltage also would occur for values extending ΔV below (above) the experimentally obtained values. More than ΔV away from the edges the artificially

extended values do no longer affect the spectra due to the exponential weighting. Using this method, the only parameter that must be set is the voltage width, ΔV. This parameter should be set larger than half the band gap to avoid diverging curves. Only minor differences can be seen using different values and in the work performed here typical values that were used were in between 1.0–1.5 V. For a more detailed comparison of different broadening functions see Reference[86].

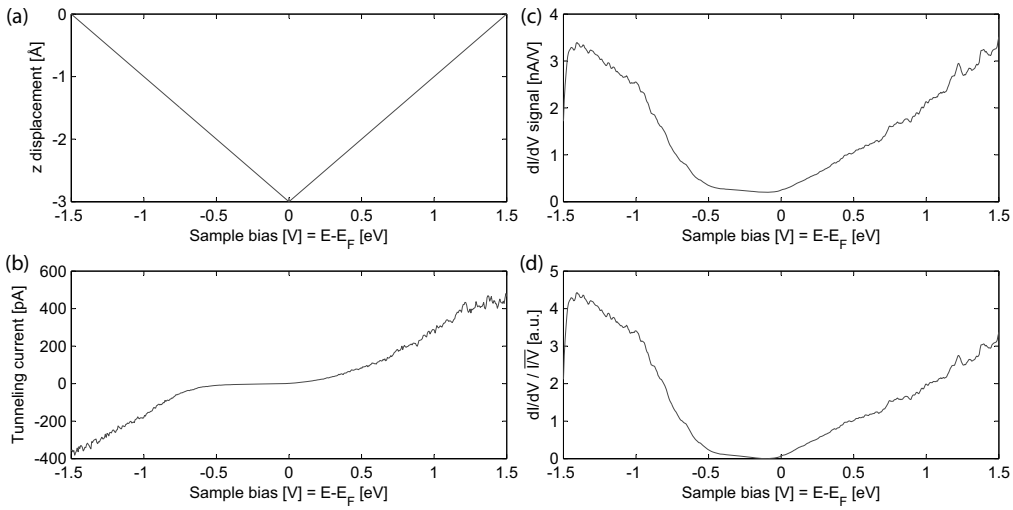

Figure 4.2. 4 graphs relevant for an STS experiment as acquired on an InAs{11–20} facet. (a) the tip z-displacement as a function of sample bias where 0 Å marks the height at the start of spectrum acquisition using a = 2 Å/V. (b) I - V curve showing the tunneling current as a function of sample bias. (c) dI/dV-signal as obtained from the lock-in. (d) dI/dV / I/V as obtained after the dI/dV curve was convoluted with the broadened I/V-curve broadened by ΔV = 1 V.

In the final diagram showing (dI/dV) / (I/V) features including band edges, possible surface states, dopant induced states, and more can be deduced. In Figure 4.2, both the dI/dV-signal and the normalized quantity are shown where it is possible to, among other things, see a decrease in the signal strength at states far away from the Fermi level. In order to gain information about the position of the band edges, they were zoomed in individually and a linear model was drawn to match the slope of the curve at the onset[83]. The cross section of the linear model and the base line defines the band edge. However, in some cases it is non-trivial to find a suitable linear fit to the LDOS increase at the band edges. It is then possible to fit the onset very close to the edge using a simple model assuming a linear increase of the DOS and a thermal broadening[87], as is depicted in Figure 4.3. In Paper II, I compared the two methods of extracting band edges and found that they gave similar results. The energy resolution in room temperature STS

experiments is limited by the thermal broadening of all electronic states (kT = 25 meV at 300 K). Obtaining the STS data at low temperature is therefore preferred, but is at the same time associated with additional effects such as possible freeze-out of dopants and semi-insulating samples.

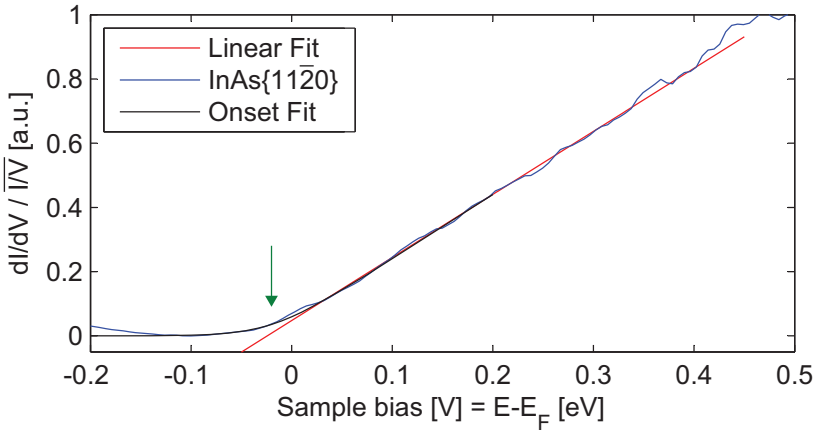

Figure 4.3. Band edge determination at the InAs{11–20} facet. Red is a linear fit to the onset of the conduction band edge. The onset can be found at the intersection with y = 0. Black is obtained using a fitting procedure as described in Reference [87] with an onset value of -0.02 eV. Green arrow marks the onset according to both models.

4.2 Tip-induced band bending

When a metal tip is brought close to a semiconductor sample it will form a metal-insulator-semiconductor junction where the mere existence of the tip will affect the electronic bands in the semiconductor[88-91]. Depending on the Fermi levels of tip and sample, the tip work function, the sample electron affinity, charge carrier concentration, and the distance between tip and sample, the bands will bend differently in the semiconductor. This has consequences for STM/S since the measured band position at the surface will be different from the one in the bulk, and more importantly, it will depend on the tip that is being used. Even if the tip material is kept the same, the tip work function will differ depending on the exact geometry of the apex[76, 92].

During an STM/S experiment an external bias is applied to the sample (in my case, I apply it to the tip, but nevertheless call it sample bias). Ideally, all of the applied sample bias drops in the vacuum barrier between the tip and the sample. However, it is often

found that the bias is dropped partly in the vacuum barrier, and partly in the sample itself, as depicted in Figure 4.4.

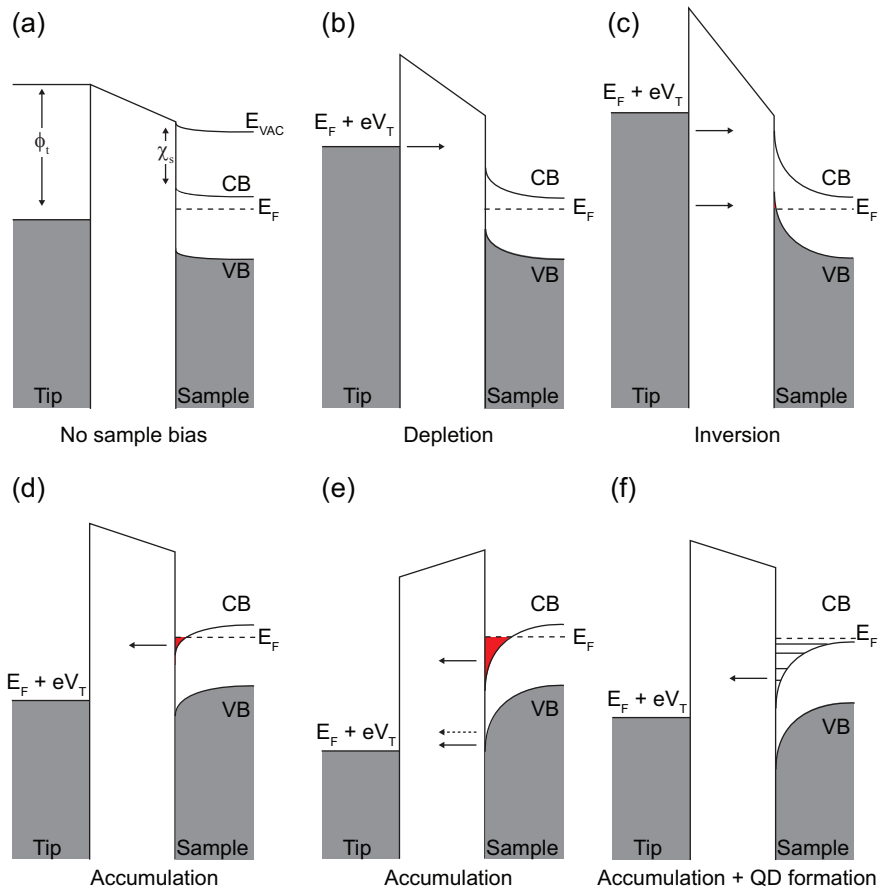

Figure 4.4. Tip-induced band bending (TIBB) at different sample bias settings for an n-type semiconductor. (a) No sample bias applied, the TIBB is determined by the tip work function, ϕ_t, the sample electron affinity, χ_s, the charge carrier concentration in the sample, and the width of the vacuum barrier. (b) Under positive sample bias, the bands bend upwards in the near surface region of the sample. The CB gets depleted of electrons. Electron tunneling is marked by the black arrow. (c) Under a large positive sample bias inversion occurs and electrons can tunnel from the tip directly into the VB. (d) Under negative sample bias the bands bend downwards giving an electron accumulation region at the surface CB (red area). (e) Under large negative sample bias electrons can also tunnel directly from the VB into the tip as well as having a probability of tunneling through the narrow band gap region (marked by a dashed arrow). (f) Occasionally, quantum-confined states can form in the CB called tip-induced quantum dots. Valence and conduction band are marked *VB* and *CB*, respectively. V_T marks the sample bias, E_F marks the Fermi level, E_{VAC} denotes the vacuum level.

If a positive sample bias is applied ($V_T > 0$ V) part of the bias will be dropped in the vacuum region and part will be dropped in the sample itself as sketched in Figure 4.4(b). Electrons will be allowed to tunnel from the tip into empty CB states. Due to the reduced amount of electrons at the surface, this is known as depletion. At even higher positive bias inversion can occur, as depicted in Figure 4.4(c), resulting in the Fermi level of the sample being positioned below the VB edge at the surface. Electrons can thus tunnel both into CB states as well as into VB states above the Fermi level. On the other hand, for a negative sample bias ($V_T < 0$ V) the bands bend downwards giving an increase in electrons at the surface, known as accumulation. If the sample Fermi level positions above the CB edge, a tunneling path opens up. At higher negative bias electrons are allowed to tunnel from the sample VB into the tip as well. If the extension of the TIBB is short (as in Figure 4.4(e)) electrons have a probability of tunneling through the gap as is depicted by the dashed arrow. In some instances it has been shown that the TIBB might induce confined, quantum dot like states as shown in Figure 4.4(f)[89, 93].

The TIBB can become a major challenge when trying to map the local band structure. For low-doped GaAs(110) it has even been shown that the TIBB can become too large and no carrier inversion takes place, making it impossible to tunnel into empty conduction band states[94]. In Paper II, I could observe this phenomenon in real time when I scanned on nominally undoped GaAs Wz NWs. When a new, sharp tip was used to scan the sample, a tunneling current could be detected at positive sample bias. After hours of scanning, with accompanied tip blunting, no signal could be detected at the positive side anymore which was a clear indication of the increase in TIBB that occurs using less sharp tips. Similar results could also be obtained by imaging close to the CB edge and adjusting the tip–sample separation by tuning the tunneling current. At smaller separation (larger TIBB), the imaging became less controlled and more noisy, whereas an increased separation (smaller TIBB) allowed for proper atomic scale imaging.

In most cases, the TIBB "only" gives an increase in the observed band gap due to some of the bias being dropped in the sample itself. In Figure 4.4, it can be seen that opposite band bending effects take place at VB and CB edges. In an STS-experiment where the bias is swept from negative to positive, the band bending in the sample will go from being upward to being downward and thus give the appearance of an enlarged band gap. Thankfully, a publicly available 3-dimensional Poisson solver that models a hyperbolically shaped tip in close proximity to a semiconductor has been developed by Feenstra[87, 95, 96]. Using that software, it is possible to simulate the band bending that occurs in a semiconductor given that you know, among other things, the tip geometry, the sample charge carrier concentration, the contact potential, and the tip–sample separation. Most of the parameters, except for the tip geometry, can be estimated or are known. In Paper II, I studied GaAs NWs with axial stacking of Wz and Zb crystal structure and used the well-known GaAs{110} facet as a reference in order to deduce the tip geometry.

The same tip-setting was later used to estimate the TIBB in the Wz part and deduce band gap energy offsets.

The TIBB reasoning is valid for all III–V {110} facets, but for a facet experiencing a Fermi level pinning at the surface, the charges associated with the pinning would most often be very effective in screening the potential associated with the TIBB. Therefore, STS on a pinned surface shows a measured band gap which is close to the expected value. In Paper III, I studied doped InP NWs and could observe a midgap Fermi level position for the part doped p-type and a measured band gap that was clearly not influenced by TIBB. I explained the STS results using a surface reconstruction induced Fermi level pinning.

5. Electron diffraction and spectroscopy

Two of the most common surface science techniques, x-ray photoelectron spectroscopy (XPS) and low-energy electron diffraction (LEED) have been used in order to gain complementary insights into the surface chemistry and structure of NWs. In this chapter, some fundamental aspects of these techniques are presented.

5.1 Low energy electron diffraction

Already in 1927 Davisson and Germer conducted the first LEED experiments, thereby preceding the discovery of the STM by almost 60 years[97, 98]. They found that the angular intensity distribution of low energy (roughly 100 eV) elastically scattered electrons from a Ni crystal showed a structured pattern due to diffraction, proving that the electrons behaved like waves. Davisson was awarded the 1937 Nobel prize shared with Thomson "for their experimental discovery of the diffraction of electrons by crystals".

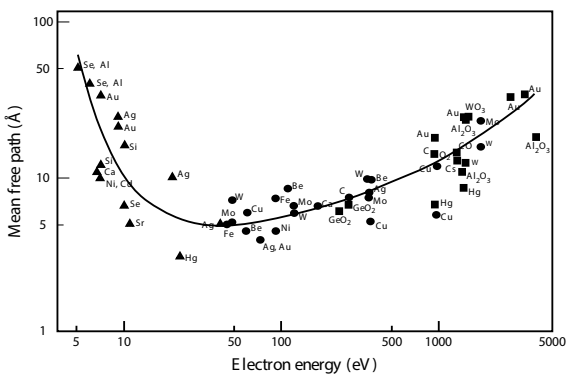

Figure 5.1. Electron inelastic mean free path in solids.

In LEED, a monoenergetic beam of low energy electrons (usually between 20–200 eV) is incident on a crystal and the angular distribution of the elastically scattered (diffracted) electrons is analyzed. Low energy electrons have de Broglie wavelengths in the order of interatomic distances making them suitable for detection of atomic spacings. They interact strongly with materials and the inelastic mean free path (MFP), i.e. the average distance an electron can travel before undergoing inelastic scattering, is on the order of a few Ångströms and virtually elemental independent, Figure 5.1. If an ordered surface exists, the spatial distribution of the LEED spots reflects the symmetry and crystalline order, showing the reciprocal space map of the surface. From the position of the diffracted electron beams, the two-dimensional periodicity of the surface unit cell may be deduced as well as domain orientations, adsorption structures, and changes in unit cell size.

As was explained in Chapter 1, the Zb structure can be viewed as two interpenetrating fcc lattices whereas the Wz structure can be seen as two hcp lattices. The LEED spots observed for Zb and Wz surfaces will therefore show fcc or hcp symmetry. In Figure 5.2 LEED-patterns for relevant low index NW surfaces are shown.

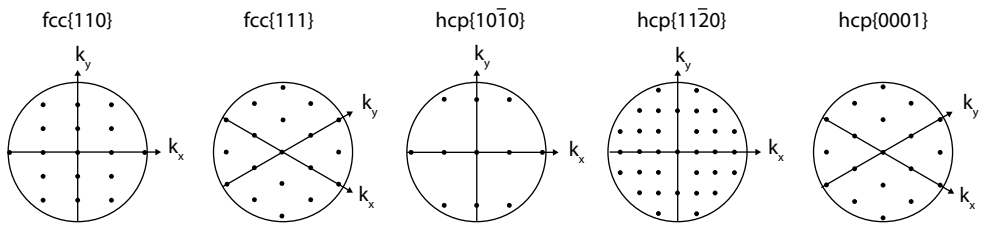

Figure 5.2. LEED patterns from some low-index surfaces related to the work presented in the dissertation. Fcc denotes face-centered cubic and hcp denotes hexagonal close-packed.

A conventional LEED setup typically has an electron spot diameter in the millimeter regime, and is therefore not suitable for NW studies. However, the underlying scattering mechanisms and surface sensitivity is fundamentally important for LEEM studies, which can be performed on single NWs and are discussed in Chapter 6.

5.2 X-ray photoelectron spectroscopy

In 1887 Hertz discovered that electrons can be emitted from a surface under light irradiation[99]. Einstein explained it in the theory of the photoelectric effect[100] for which he was awarded the Nobel Prize in 1921. It was later realized that by illuminating a

sample with monochromatic light and observing photoelectrons with specific kinetic energies one could retrieve chemical information about the sample. A large part of the development was performed by Siegbahn for which he was awarded the Nobel Prize in 1981.

In a photoelectron experiment, monoenergetic photons, with energy $h\nu$, irradiate a sample and electrons are promoted from an occupied initial state, E_{in}, to an unoccupied final state, E_{fi}. If a sufficiently energetic photon is incident, the photoelectron can escape into vacuum and be detected by an electron energy analyzer which can determine the number of electrons and their kinetic energy, E_k. By keeping the sample at the same potential as the analyzer, the sample Fermi level, E_F, becomes a natural reference level. The initial state energy can then be expressed as $E_{in} = E_k + \Phi - h\nu = -E_b$, where Φ is the work function of the sample, and E_b is the binding energy of the electron. The emitted photoelectrons can be studied in a dedicated XPS setup or in a PEEM setup. The PEEM setup has the benefit of spatially resolved studies but the energy resolution is lower. Importantly, the sample is floating at high negative potential in the PEEM, whereas it is kept grounded in the XPS setup.

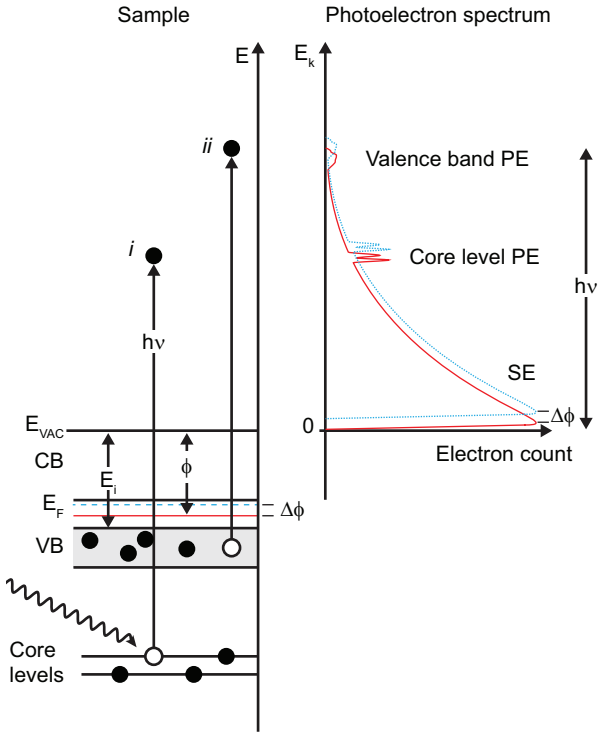

Figure 5.3. Schematic description of the photoelectron emission process. A photon incident on a sample can promote electrons from either the core-levels or from the valence band region, depending on its energy $h\nu$. Core-level photoemitted electrons (i) give rise to sharp peaks in the spectrum. Valence band photoemitted electrons (ii) directly give the valence band DOS. High intensity secondary electrons (*SE*) with a maximum at very low kinetic energy can also be seen. A change in the Fermi level of the sample by $\Delta\phi$ (red and blue line, respectively) shows up in the photoelectron spectrum as a shift of all peaks, including the SE peak by the same amount. Indicated in the figure: the vacuum level (E_{VAC}), conduction band (*CB*), valence band (*VB*), Fermi level (E_F), work function (ϕ), ionization energy (E_i), Fermi level shift ($\Delta\phi$), Core-level states, photon energy ($h\nu$), photoelectron kinetic energy (E_k), valence band and core-level photo electrons (*PE*), and secondary electrons (*SE*). Please note that the energy distances between the bound states, hν, and Φ are not drawn to scale.

The emitted photoelectrons can be divided into three categories, Figure 5.3. Starting from low photoelectron kinetic energy and extending all the way up to $E_k = h\nu - \Phi$, secondary electron (SE) emission can be found. The SEs have undergone inelastic scattering or are emitted from a secondary event and it is therefore possible to get several SEs from one primary excitation event. SEs are dominated by electrons emitted from the valence sea, originating from a cascade of refilling processes, and have lost information about the original excitation event[101]. The high intensity SE emission constitutes the major part of all emitted photoelectrons and is virtually featureless except at the onset.

The onset of the SE emission depicts transitions from the top of the valence band into vacuum and can thus be used to probe the ionization energy, E_i. Another important quantity within semiconductor physics is the electron affinity, χ, depicting the energy needed to promote an electron from the conduction band edge to vacuum. This quantity is used to determine, among other things, band offsets between semiconductors but has not been studied here.

At higher E_k, photoelectrons directly emitted from the tightly bound core-levels are found. The binding energies of the core-levels are specific to each element and well-documented (at least for all elements investigated in this dissertation). Core-level photoelectron spectroscopy can go far beyond the identification of the elements in the sample. Even though the core electrons do not directly take part in the chemical bonding (in difference to the valence electrons), they will undergo slight changes in binding energy due to the local chemical surrounding, called chemical shifts[102].

At even higher E_k, photoelectrons directly emitted from the valence band can be found. The valence electrons take an active part in chemical bonding and interpretation of these photoelectrons is usually non-trivial. One of the main techniques that utilize these photoelectrons is angle-resolved photoelectron spectroscopy (ARPES) in which the dispersion of the valence electrons can be probed, allowing for momentum resolved mapping of occupied bands. The photoionization cross-section for valence electrons decreases with increased photon energy and most studies are therefore often performed using photon energies below 100 eV.

A shift of the work function by $\Delta\phi$ (which can be accomplished by e.g. doping a material) also induces a shift of all photoelectron peaks by the same magnitude as is illustrated in Figure 5.3. It is therefore possible to probe $\Delta\phi$ using any of the above mentioned photoelectron types. In Paper III, I studied core-level peaks of doped InP NWs and found a close to conduction band Fermi level pinning for both n-type and p-type NWs when covered in native oxide which could be (partly) lifted by annealing the NWs in atomic hydrogen and removing the native oxides as seen by a binding energy shift in the core-level peaks.

Although the x-rays used to illuminate the samples have a fairly large penetration depth, XPS is considered surface sensitive. The photo emitted electrons that were used in the work presented in this dissertation had energies ranging from 50–1000 eV giving them a very short mean free path in solids, as shown in Figure 5.1. Photoelectrons emitted from depths larger than 3 MFP do not contribute significantly to the signal giving us a possibility to study depths ranging from some Å down to a few nm into the sample.

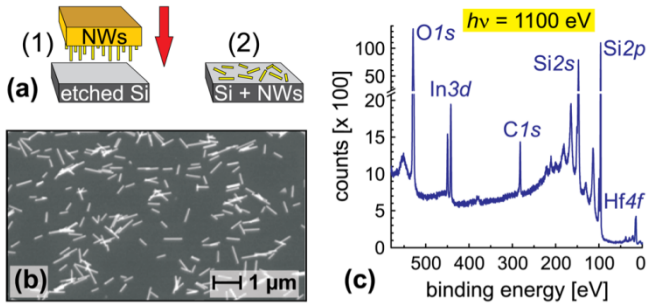

Figure 5.4. (a) Sketch of the NW deposition: The growth sample containing vertical NWs is gently pushed onto a Si substrate, resulting in (b) InAs NWs deposited on a Si substrate, imaged by SEM after XPS measurements. (c) XPS overview spectrum of InAs/HfO_2 NWs deposited on a Si substrate, obtained at a photon energy $h\nu$ = 1100 eV. Please note the changing scale of the y-axis. For more details, see Paper VI.

In Figure 5.4, I present the outline of a NW XPS study. InAs NWs capped with HfO_2 are deposited on a Si substrate by mechanical break off as described in Section 2.4. Core-level positions from the Si substrate such as the well-studied Si*2p* peak are used as energy references. Every experiment session typically starts by obtaining an overview spectrum displaying a number of core-levels, Figure 5.4(c), allowing for identification of possible contaminants. The overview spectrum is dominated by very strong oxygen and silicon peaks from the substrate but it is at the same time possible to identify indium and hafnium related peaks. The As peak that I use the most, As*3d*, can be hinted at 40 eV binding energy but is very small due to its low photoionization cross-section at high photon energies. After mapping the overall surface chemistry, high resolution spectra are obtained around each core-level of interest.

In order to deduce information from the spectra, some basic properties of the core-level peak shape need to be considered. Every peak has an intrinsic Lorentzian line shape which is due to the finite life time of the core excited system[103]. Every peak also gains a Gaussian broadening due to limitations in the experimental setup such as finite energy width of the x-ray source, analyzer resolution etc.[104]. In this work, the final line shapes have been fitted self-consistently using a so-called Doniach-Sunjic line profile which takes both the Lorentzian and Gaussian contributions into account[105]. In addition to this, the local chemistry (chemical shifts), as well as spin-orbit split components give rise to slight binding energy variations. A slowly decaying background arising from SE emission can often be approximated by a linear fit.

XPS measurements gain a lot from the usage of synchrotron facilities, not only due to the increase in photon flux compared to laboratory sources. The tunable x-rays give the possibility to choose photons so that the kinetic energy of the photoelectrons is kept constant when mapping different core-levels. The same kinetic energy means equal probing depths, as shown in Figure 5.1, which facilitates an easier interpretation. Further,

by mapping the same core-level using different photoelectron kinetic energies, it is possible to obtain chemical depth analysis in the near surface region. In Figure 5.5, As*3d* spectra obtained from an InAs(100) crystal covered in native oxide using photon energies between 170 and 930 eV, corresponding to photoelectron kinetic energies of 130 to 890 eV, is shown. In every spectrum it is possible to see peaks related to: spin-orbit split As bound to In (green), As in a +III oxidation state (As_2O_3, blue), As in a +V oxidation state (As_2O_5, light blue), and a gray background from the SE emission[106]. As higher photon energy is used, photoelectrons can escape from deeper into the sample and become less surface sensitive. From Figure 5.5 it can be seen that the ratio between the surface oxide related peaks and the bulk related As–In peak changes dramatically when probing deeper. Studying the oxide peaks, it can be seen that the ratio between the two As-oxides changes. From this, it was possible to conclude that the native oxide had a top part consisting mainly of As+III-oxide but had more As+V-oxide closer to the InAs-oxide interface.

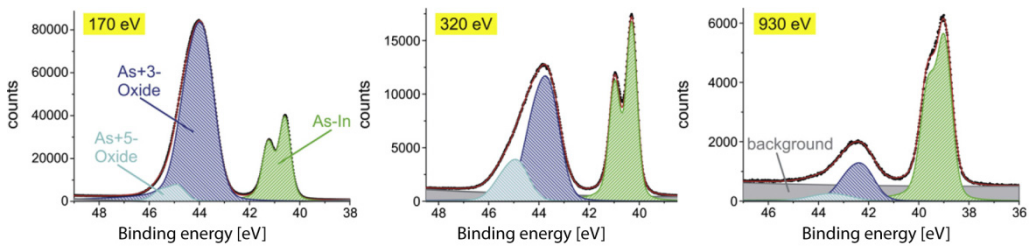

Figure 5.5. As*3d* spectra from an InAs single crystal measured using different photon energies as indicated in the upper left corner of each spectrum. The ratio between the two oxide species changes as a function of photon energy because the probing depth increases with increased photoelectric kinetic energy. The change in binding energy is due to a slight problem with the x-ray monochromator. For more details see Reference [107] (Paper XII).

Not only is it useful to have tunable x-rays from the synchrotron when probing different elements keeping the same surface sensitivity, but it is also useful in order to maximize the photoionization cross-section for the different core-levels when studying infrequent surface elements. In Figure 5.6, the photoionization cross-section for the As*3d* and In*3d* core-levels are shown. Depending on the photon energy, the cross-section varies orders of magnitude and care must thus be taken when performing quantitative comparisons of intensities for different photon energies (or different core-levels). In every experiment, the photon energy must thus be chosen wisely in order to keep an appropriate surface sensitivity, obtain a sufficient photon flux from the undulator, and have large enough photoionization cross-section for the investigated core-level.

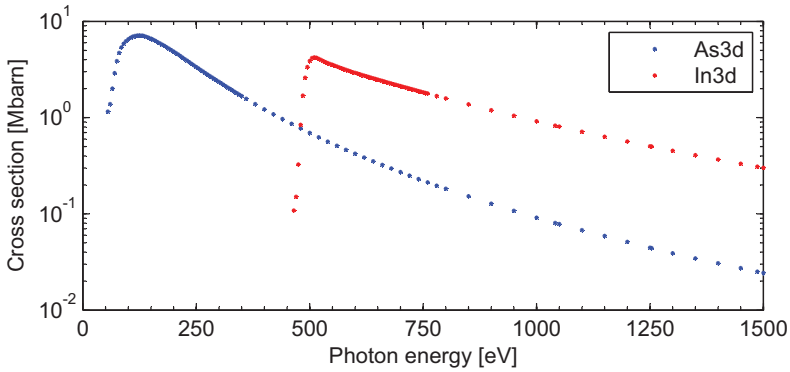

Figure 5.6. Photoionization cross-section for In*3d* and As*3d* as calculated by Yeh and Lindau[108].

I have used a dedicated XPS setup at the soft x-ray, undulator beam line I311 at the national Swedish synchrotron radiation facility, the MAX-IV laboratory, Lund[109], for studies of NW surface chemistry. I311 features a hemispherical Scienta electron energy analyzer, a photon energy range of 43–1500 eV, and spot size of 0.5 mm (horizontal) and 0.1 mm (vertical). The (for NWs) large spot size makes it ideal for studies of NW assembles where many homogenous NWs are deposited on a sample and the XPS signal is averaged.

In Paper VI, I used XPS for studies of interfacial chemistry of InAs NWs covered in 2 nm of two different high-κ oxides, Al_2O_3 and HfO_2. High-κ oxides are used as gate oxides in field-effect transistors and the interface chemistry between the conducting channel (in this case the InAs NW) and the oxide has been seen to be closely linked to the device performance[110-112]. NWs with high-κ were studied and compared to NWs with native oxide. It was possible to monitor the interfacial chemistry between the high-κ and the InAs NW mapping In- and As-oxides, and evidence of metallic As was found.

6. Cathode lens microscopy

The first modern cathode lens microscope was constructed in the 1980's by Telieps and Bauer[113] making use of UHV-technology and low energy electron lenses. Cathode lens microscopy is a collection of several different microscopy techniques in which the sample is part of the objective lens (it is the cathode). In this dissertation only instruments working with elastically back-scattered electrons (low energy electron microscopy, LEEM and mirror electron microscopy, MEM), and x-ray generated photoelectrons (XPEEM) are considered, but instruments working with e.g. thermal electrons (TEEM), and inelastically scattered electrons have been constructed[114].

Cathode lens microscopes are full-field microscopes, i.e. they image the whole surface at once, and can therefore be used for real-time image acquisition. Cathode lens microscopy has been used to study dynamics at surfaces[115, 116], chemical reactions[117, 118], surface phase transitions[119, 120], adsorption of molecules[121], growth of nanostructures[122], and much more.

6.1 Spectroscopic photoemission and low energy electron microscope

All the LEEM/MEM and XPEEM measurements were performed within the same instrument, an Elmitec spectroscopic photoemission and low energy electron microscope (SPELEEM) III situated at beam line I311, MAX-IV laboratory. The SPELEEM is equipped with a hemispherical electron energy analyzer, is operated in UHV, and has the possibility to acquire video rate images of samples at 100-1800 K. X-rays in between 50 and 600 eV can be used for XPEEM experiments. The spatial resolution is approximately 10 nm for LEEM and around 30 nm for XPEEM.

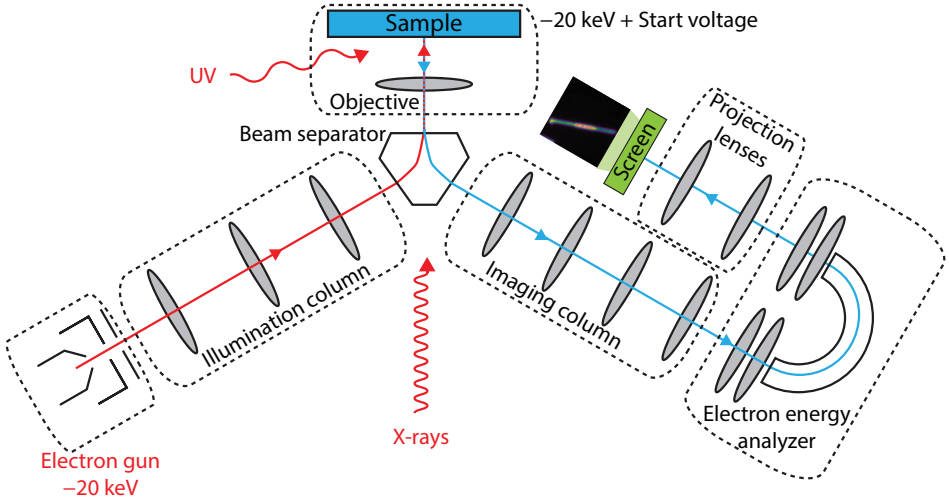

Figure 6.1. Schematic description of the SPELEEM instrument at the MAX-IV laboratory. The sample may be illuminated by low energy electrons, synchrotron x-rays, or UV-light. Red path marks illuminating electron path or photon excitation source. Blue path marks imaging path (both for LEEM and PEEM). Gray depicts position of electron lenses.

The difference between a SPELEEM and other types of electron microscopes is the immersion objective lens and the beam separator, both shown in Figure 6.1. Illuminating electrons at –20 kV are generated at the electron gun, a LaB6 crystal, and focused by lenses in the illumination column. The beam separator, a magnetic sector field, is used to separate incoming (illuminating) electrons in LEEM/MEM from outgoing, reflected electrons, using a 60 ° deflection in the electron trajectory. The sample is the cathode of the objective lens and is biased at –20 kV with reference to the anode of the lens. The high electric field decelerates the illuminating electrons (in case of LEEM/MEM) and they interact with the sample as surface sensitive low energy electrons where their energy at the sample is determined by the potential difference between gun and sample (start voltage). After interaction, the electrons are reaccelerated by the same electric field to high voltage and travel through the imaging column, the energy analyzer, and get projected onto a screen. For PEEM, photoelectrons are emitted from the sample and accelerated by the electric field in the objective lens and travel in the same path as the reflected/diffracted electrons in MEM/LEEM, see blue path in Figure 6.1.

By decelerating the electrons one gains the surface sensitivity of slow electrons while at the same time being able to use conventional electron lenses when the electrons travel in the microscope (the lenses have the highest performance for fast electrons). It should be mentioned that the electrons travel at relatively low speed also in the electron energy analyzer.

The design using a 60 ° bend in the magnetic sector field is used by Bauer (Elmitec GmbH) but other manufacturers have emerged with different designs. Tromp (Specs GmbH) has developed a LEEM instrument with a beam separator utilizing 90 ° bends[123, 124]. In addition, PEEM instruments having a linear layout and working with electrostatic lenses have been designed by Schönhense (Focus GmbH) but do not have any magnetic sector field since they do not have an illuminating electron source[125].

Several exciting possibilities for NW surface microscopy is presented in Section 6.2–6.4 and in most of these studies, the spatial and energetic resolution is limited by aberrations in the objective lens. During the past years, enormous efforts have been put into the creation of aberration corrected (both spherical and chromatic aberrations) microscopes where the most successful development has been with the usage of electron mirrors to compensate for the aberrations of the objective lens[123, 124, 126, 127]. With these new instruments, LEEM resolution below 2 nm has been presented and an order of magnitude increase in transmission (amount of detectable electrons) is expected[123, 128]. The SPELEEM at the MAX-IV laboratory will be upgraded to an aberration corrected microscope during 2014.

6.2 Mirror electron microscopy

At low start voltages the illuminating electrons do not have enough energy to reach the sample, but rather turn around tens of nanometers away from the surface, thus only interacting with the electric field outside the sample, called mirror electron mode (MEM) imaging. MEM imaging is usually considered a non-destructive technique since the electrons do not directly interact with the sample and it has been used to study droplet dynamics[115, 116], surface electric fields[129, 130], surface magnetic fields[131], and chemical reactions at surfaces[132]. The technique is especially well-suited for studies of materials which cannot withstand conventional electron microscopy, such as easily degradeable biomolecules.

MEM contrast is due to changes in the potential field outside the sample surface, i.e. electric and magnetic field variations in the sample, surface topography, contact potential, or work function variations across the sample[129, 131, 132].

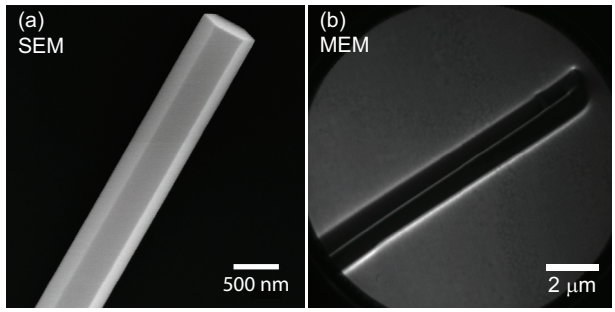

Figure 6.2. Example of a NW imaged using mirror electron microscopy. (a) SEM image showing the morphology of a large InAs NW deposited on a Si substrate. (b) MEM image obtained of an InAs NW showing a non-intuitive appearance.

MEM contrast is seldom easily interpretable, therefore models using geometrical ray-tracing[133-135] and wave-optical treatment[136] have been developed which are well-suited for small deflections of the incoming electrons. For larger deflections (as would be the case for NW studies) strong features, so-called caustics, are observed experimentally and not accounted for by the above mentioned techniques. In Figure 6.2, a comparison between SEM and MEM images of large InAs NWs is depicted. In SEM, the morphology of the NW can clearly be seen and the hexagonal cross-section is obvious. In MEM, the contrast is non-intuitive with bright, caustic edges surrounding a dark NW with a bright stripe in the middle. The apparent size of the NW is also much larger than what would be expected from SEM. In order to explain the observed contrast, I have employed caustic imaging theory, which is discussed below. For additional details, see Paper V.

As a first step, the electric field as it is just outside the sample needs to be determined. In Figure 6.3, finite element modeling has been used to calculate the equipotential curves of the electric potential just outside an infinitely long 500 nm diameter InAs NW lying flat on a Si substrate. The equipotential curves quickly become very smooth and little information about the geometry of the sample can be seen in the equipotential curves at 100 nm above the NW. The start voltage determines how close to the NW the electrons reach before turning around. In order to distinguish minor geometrical variations in the sample, it is necessary to use a high enough start voltage to allow the electrons to turn around close to the NW.

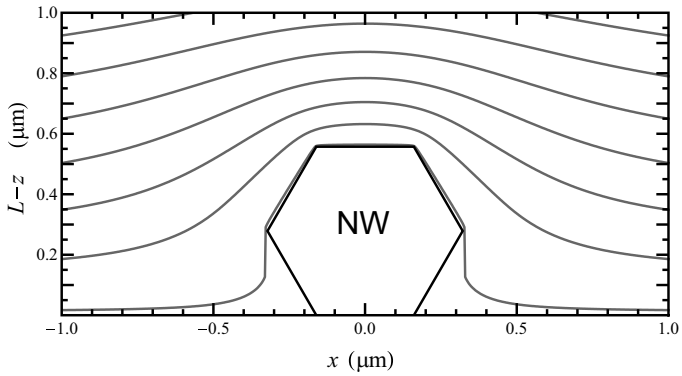

Figure 6.3. Equipotential surfaces of the electric potential (gray lines) above an infinitely long nanowire, 500 nm diameter NW with hexagonal cross section is shown (black line). The nanowire is kept at the potential V = −20000.4 V, i.e. calculated for a start voltage of −0.4V, the first equipotential line above the nanowire is at −20000.3 V, and the subsequent lines are +0.4 V apart (e.g. the second is at −19999.9 V). See Paper V for more details.

In Figure 6.4, a schematic description of the caustic image formation used for MEM modeling is shown. Illuminating electrons from the source face the sample in parallel beams. The electrons turn around at a distance L_M away from the sample and get reaccelerated back by the electric field between the anode (A) and cathode (C) of the objective lens. The electron rays are traced back (red dashed lines) and assumed to form a virtual image at $z = \Delta f + 4L_M/3$, where Δf is the defocus distance from the plane $z = 4L_M/3$ set by the current in the objective lens[137], and L_M is the turnaround distance above the sample.

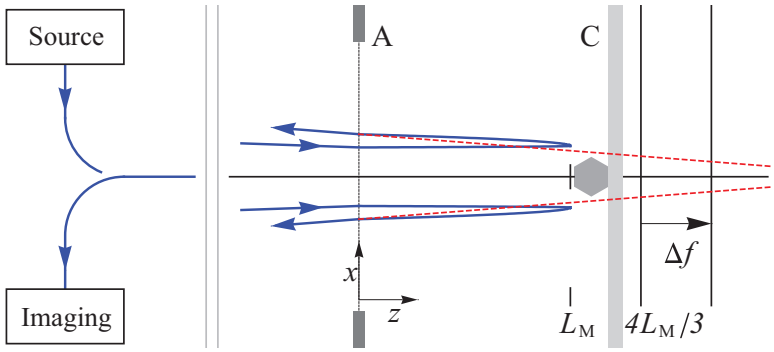

Figure 6.4. Schematic description of the caustic image formation used for MEM modeling. Illuminating electrons from the source face the surface in parallel beams between the anode (A) and the cathode (C, the sample) of the objective lens. The electrons turn around at a height L_M above the sample and after interacting with the potential field above the sample they get reaccelerated back by the electric field. The microscope is assumed to form an image of the electron positions as they would appear on a virtual image plane at $z = \Delta f + 4L_M/3$ (back traced dashed red line) where Δf is the defocus set by the current in the objective.

In line with the caustic imaging formation theory, a parallel beam of electrons is incident on the sample and their interaction with the electric field as shown in Figure 6.3 is evaluated and presented in Figure 6.5. A complete ray tracing including incoming, reflected, and back traced rays is shown in Figure 6.5(a). The box marked α includes the incoming parallel electrons illuminating the sample. At β, i.e. just outside the sample, the electrons get deflected by the electric field outside the sample. A magnified image can be seen in Figure 6.5(b) where strongly deflected electrons overlap with electrons passing further from the NW. The rays at the virtual image plane (γ), which are the apparent straight line paths of the exiting electrons, are what the imaging system reproduces at the detector. In Figure 6.5(c), the virtual image plane is shown for different defocus values (Δf) which are set by the current in the objective lens.

More rays give a higher signal count in the detected image and some specific features can be seen. For $\Delta f = 0$ µm, the NW is predicted to have an appearance of bright caustic edges enclosing a dark area with a bright middle section. At negative defocus, the bright middle section shrinks to a single line, and at even higher negative defocus, the area in between the bright edges should be dark. For positive defocus, the bright middle segment gets wider at the same time as the caustic edges get less defined.

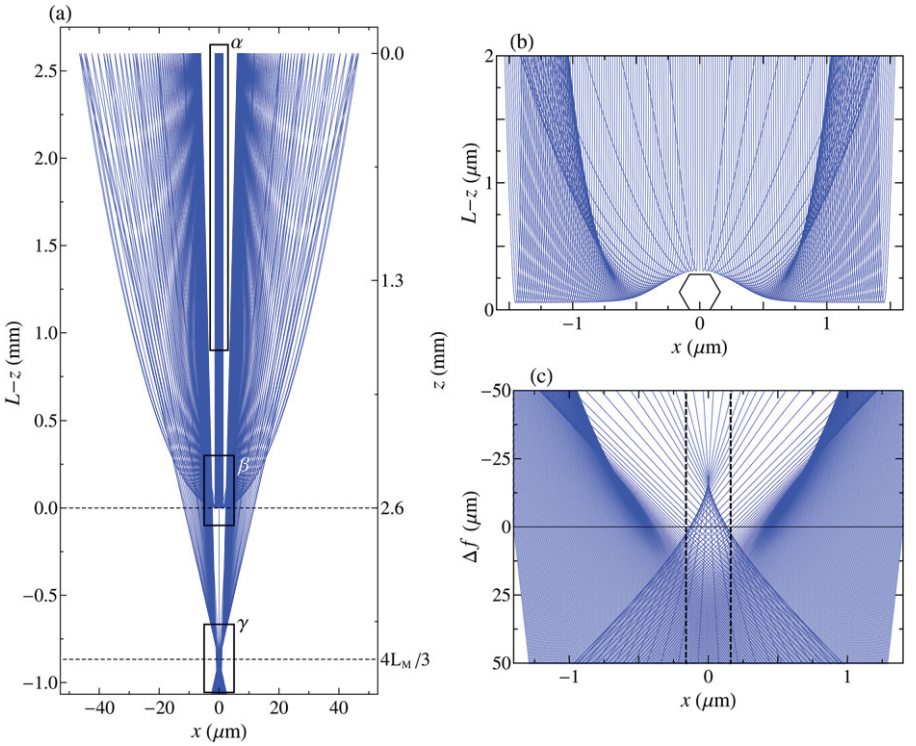

Figure 6.5. The family of electron rays simulated in the MEM system of Figure 6.4. The electron beam of energy U = −20 keV is incident on an infinitely long nanowire with 6–fold symmetrical cross section (Figure 6.3) and side length of 0.16 μm. The cathode is a distance of $z = L$ = 2.6 mm from the grounded anode aperture, indicated by a dashed line, and the cathode and NW are held at a potential of V = −20000.4 V, i.e. start voltage of −0.4 V. (a) The boxed region α includes the incident electron paths. These rays travel parallel to the z-axis until they approach the distorted electric field in the vicinity of the nanowire (Figure 6.3). (b) The electron paths close to the NW, corresponding to the boxed region β in (a). The electron rays that closely approach the NW are strongly deflected away from the NW, overlapping with rays further from the NW. (c) The apparent straight line paths of the exiting electrons at the virtual image plane $z = \Delta f + 4L_M/3$, for defocus Δf which is controlled by the objective lens current. This region corresponds to the boxed region γ in (a), with 2.5 times the number of rays. The edges of the nanowire (the corner at x = ±0.16 μm) are shown indicated by vertical dashed lines. Note that banding patterns evident in the regions of closely spaced rays in (b), and (c), are Moiré effect artifacts inherent in the method of presentation.

Using the results from Figure 6.5(c) and simulating images based on different defocus values it is possible to compare the caustic imaging theory to experimentally obtained images where the defocus is changed by varying the objective current, Figure 6.6. The caustic imaging theory was found to reproduce all features of the experimental images in a satisfactory way.

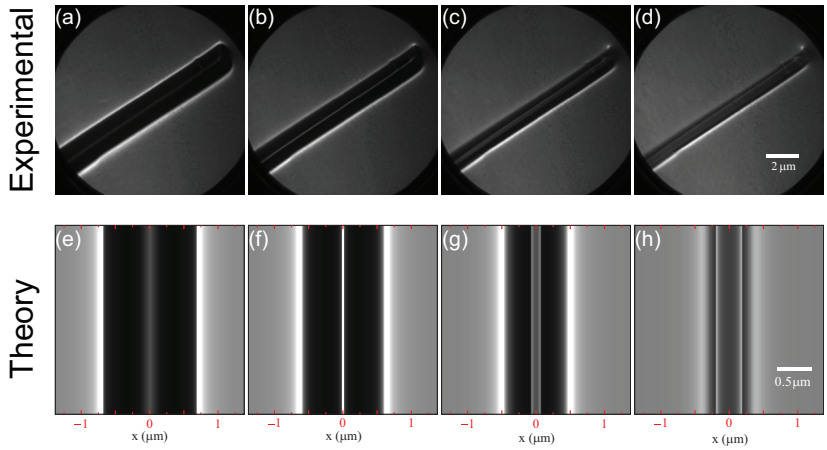

Figure 6.6. (a–d) Experimental MEM images of an InAs nanowire on a Si substrate, with varying objective lens current i.e. defocus providing a through focus sequence of images. The start voltage is –0.4 eV, acceleration voltage 20 kV, the electron beam turns approximately L = 52 nm above the specimen surface. The objective lens current is (a) 1597.5 mA, (b) 1596.0 mA, (c) 1594.5 mA, and (d) 1593.5 mA. (e–h) Corresponding simulated MEM images of an InAs nanowire on a Si substrate, generated from Figure 6.5(c) at defocus (e) Δf = –22 µm, (f) Δf = –15 µm, (g) Δf = –5 µm, and (h) Δf = 5 µm.

Interestingly, from the theoretical calculations it was also possible to simulate the influence of minor geometrical variations such as a 30 ° rotation of the NW along its growth axis and conclude that it had only a minor effect on the images, see Paper V. With the use of caustic imaging theory, it is now possible to, in a non-destructive way, study electronic and/or magnetic variations along similar (and more advanced) nanostructures.

6.3 Low energy electron microscopy

At higher start voltage values (higher electron kinetic energy) the illuminating electrons reach the sample, enabling diffraction contrast from crystalline materials, called LEEM mode. LEEM contrast can be divided into two categories: diffraction and phase contrast. Diffraction contrast is due to local differences in the structure factor of a sample, i.e. the crystallographic arrangement of atoms at the surface. Phase contrast is related to interference effects and can be further subdivided into two categories: i) interference of electrons being reflected off terraces of different heights at the sample. These can be used for monolayer height resolution[113]. ii) Interference of electrons being reflected off the surface and off a buried interface. This has for example been used to study the thickness of graphene films on surfaces[138, 139]. For the work presented in this dissertation, focus has been on diffraction based contrast in order to determine the cleanliness of the sample

and to identify segments of varying crystal structure in NWs. A NW covered in oxide does not give rise to any diffraction contrast due to the non-ordered nature of the surface.

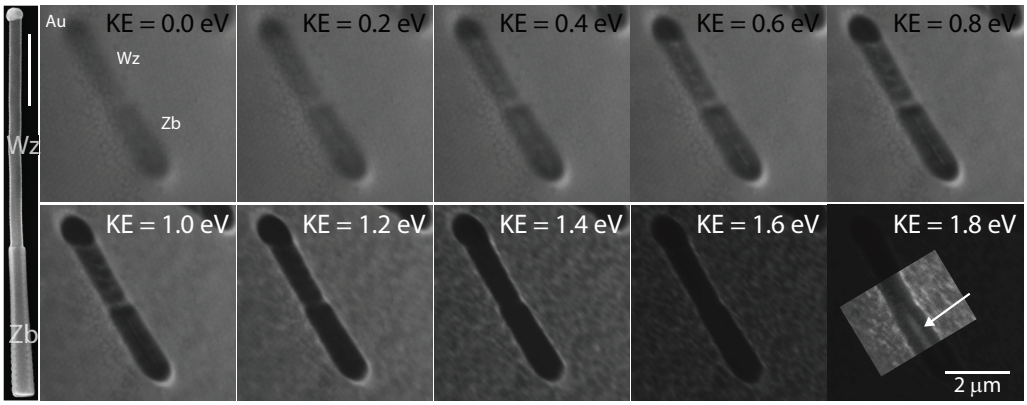

Figure 6.7. Left: SEM micrograph of an InAs NW with a Zb bottom segment ({110}-terminated), and a Wz top segment ({10–10}-terminated). MEM to LEEM transition observed for the NW where the kinetic energy (KE) of the electrons are depicted in every image. In the images it can be seen how i) the Au-particle heavily distorts the potential field outside the sample surface. ii) That there is a work function difference between Wz and Zb InAs. iii) A general decrease in signal as higher electron KE is tuned in (LEEM). iv) At 1.8 eV kinetic energy, LEEM signal from the ordered surface can be seen at the Zb part (white arrow). The contrast has been enhanced in the middle of the last image for ease of viewing. Scale bar in the left image depicts 500 nm.

In Figure 6.7, I show a series of images depicting the MEM to LEEM transition when imaging an InAs Zb-Wz NW. From the images, similar caustic features as in Figure 6.2 can be seen with bright edges and a bright stripe in the middle of the NW. Further, it is possible to identify 3 parts in the NW: Au-particle, Wz-part, and Zb-part, indicating that they have different work functions. The images were obtained using the same detector sensitivity and a strong decrease in signal can be observed when going from reflected (MEM) to diffracted (LEEM) electrons. At the highest electron energy (1.8 eV) the signal is very low compared to MEM imaging, but a bright stripe in the middle of the Zb segment can be hinted when adjusting the contrast. The bright stripe arises from LEEM contrast due to diffraction of the electrons at the ordered surface.

In LEEM, it is possible to image using electrons in the specular (00) diffraction spot (bright field imaging) as well as non-specular electrons in a diffracted beam (dark-field imaging). All LEEM results presented in this dissertation have been obtained using bright field imaging due to higher count rates compared to dark field imaging. Dark-field imaging is, however, very useful when mapping the position of different surface domains[116].

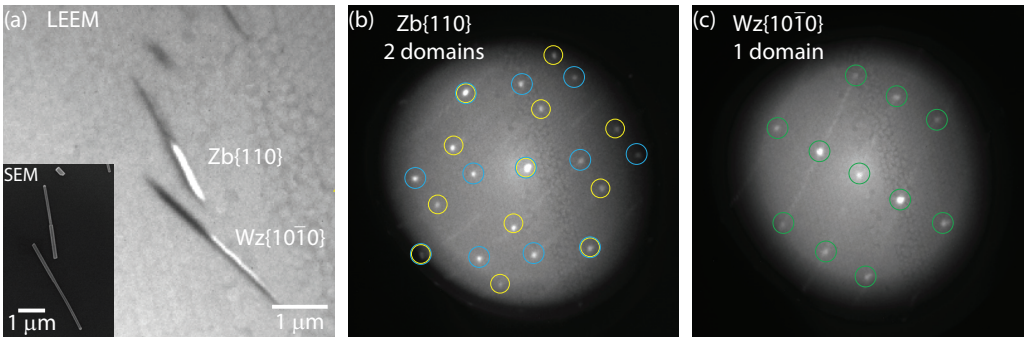

Figure 6.8. LEEM/µLEED results from InAs NWs grown with a bottom Zb segment and a top Wz segment. (a) LEEM image (electron kinetic energy 2.5 eV) depicting two NWs lying opposite to each other where the top one has the Zb segment oriented normal to the incoming electron beam and the bottom NW has the Wz segment normal to the beam as seen by the high LEEM signal. Inset shows a SEM image of the same NWs. (b) Overlaid µLEED pattern obtained from the Zb segment at the top NW depicting two {110} domains, colored blue and yellow, respectively. (c) Overlaid µLEED pattern from the Wz segment in the bottom NW showing a single {10–10} domain.

In a LEEM it is also possible to project the back focal plane instead of the image plane and thus obtain the LEED-pattern. In a LEEM instrument, the LEED spots will not be moving when the electron kinetic energy is varied (in difference to in a conventional LEED-setup)[140]. This is, however, not true for surfaces with a normal being inclined to the optical axis, and spots from those surfaces will move as the electron energy is varied. During bright-field LEEM imaging, the intensity of the specular beam gives the contrast in the image and for an inclined surface where the spots are moving, the LEEM signal only appears at some specific energies where a spot from the inclined facet happens to pass by the position of the specular beam.

An example can be seen in Figure 6.8 where µLEED-patterns were obtained from individual segments on Zb-Wz heterostructured InAs NWs. The NWs are terminated by {10–10} and {110} facets and show a 30 ° facet rotation along the NW growth axis at the Zb-Wz interface, as was explained in Chapter 2. The top NW in Figure 6.8(a) is oriented with the {110} facet facing upwards whereas the bottom NW is oriented with the {10–10} facet facing upwards as confirmed by SEM. Only the facet oriented normal to the incoming electron beam shows LEEM contrast as is seen in the figure.

By only illuminating the Zb segment in the top NW or the Wz segment in the bottom NW and projecting the back focal plane, µLEED patterns from the two facets could be obtained. At the Zb part, stationary spots were observed together with a few moving spots arising from diffraction off the non-normal {110}-type facets. By overlaying several µLEED-patterns obtained using different electron energies, the moving spots could be

averaged out, as shown in Figure 6.8(b). Indexing the pattern, it can be seen to consist of 2 {110} domains, as would be expected since this {110} facet is formed during overgrowth of a TPS as discussed in Section 2.3. Similarly, the μLEED pattern from the Wz part showed a single domain with a {10–10} pattern, see Figure 6.8(c). As a note, it can be mentioned that for μLEED patterns obtained at the Wz-segment at the top NW or Zb segment at the bottom NW, no non-moving spots could be observed.

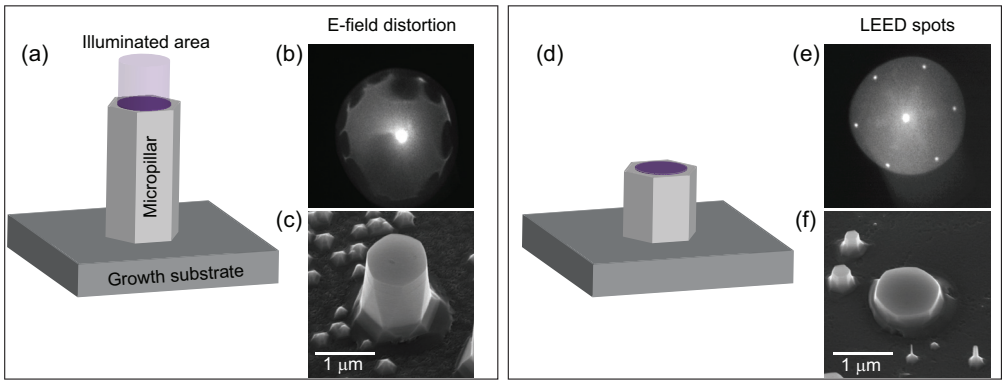

Figure 6.9. μLEED analysis from micropillars with large and small heights. (a) GaAs micropillar with high aspect ratio. The purple disc depicts part illuminated by electrons in order to obtain a μLEED pattern. (b) The obtained μLEED pattern only displays distortions in the electric field outside the sample due to the high aspect ratio. Electron kinetic energy = 19.7 eV. (c) 30 ° tilted view SEM image of the analyzed sample. (d) GaAs micropillar with significantly lower aspect ratio. (e) The μLEED pattern is free from distortions and shows clear spots with six-fold symmetry. Electron kinetic energy = 17.0 eV. (f) 30 ° tilted view SEM image of the sample with lower aspect ratio.

LEEM was developed as a tool to study planar samples and the high electric field can become a problem when analyzing objects with large height variations. A major restriction when analyzing pointy objects with large aspect ratio (such as a standing NW) is arc formation which can completely destroy a sample. A second restriction is related to the homogeneity of the electric field outside the sample which was modeled in Figure 6.3. In Figure 6.9(a–c), I investigated if 2 μm high GaAs micropillars could be studied in the LEEM. When only the top facet of the micropillar was illuminated and the diffraction pattern was projected, distortions in the electric field dominated and no LEED-pattern could be retrieved. Inserting a sample with 400 nm high micropillars instead, a LEED pattern with clear spots could be detected. It is therefore crucial to design 3-dimensional samples in a suitable way before indulging in LEEM/μLEED experiments.

6.4 Photoemission electron microscopy

PEEM measurements were performed in the same SPELEEM instrument as the LEEM/MEM experiments by turning off the electron gun and instead illuminating the sample with photons. The emitted photoelectrons were refocused, energy filtered and projected onto a screen, blue path in Figure 6.1, as was also done for reflected/diffracted electrons in MEM/LEEM.

Two different photon sources were available at the instrument: a Hg-lamp giving photons with an energy of 5 eV, and the synchrotron delivering x-rays with tunable energies between 50 and 600 eV. The low energy of the Hg-lamp, could mainly be used for work function studies. The lion's share of our PEEM experiments was, however, performed using synchrotron x-rays which allowed both electronic and chemical contrast. As was explained in Section 5.2, three useful types of photoelectrons can be emitted from the sample upon x-ray irradiation: core-level electrons, secondary electrons, and valence band electrons. A brief description of the possibilities of NW PEEM imaging using the various photoelectron types will be given below.

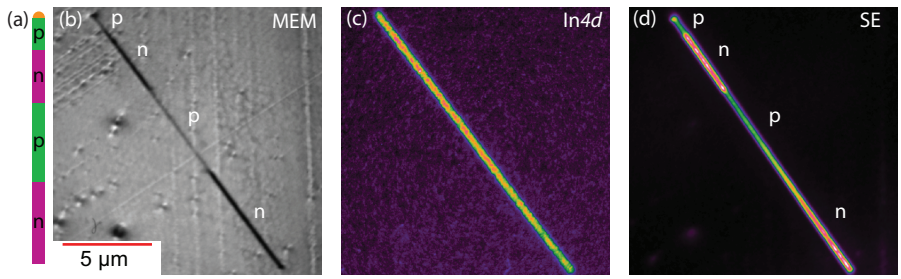

Figure 6.10. SPELEEM study of an atomic hydrogen cleaned InP NW with differently doped axial segments as shown in (a). (b) MEM image depicting the NW. The work function difference between the p- and the n-part gives the observed contrast. Start voltage = 0.13 eV. (c) XPEEM image of the same NW obtained using photoelectrons from the In*4d* core-level. Photon energy = 70 eV, Start voltage = 47.6 eV. (d) The same NW imaged in PEEM mode using SEs. Photon energy = 70 eV, Start voltage = 0.28 eV. The color code in (d) is such that the n-type part emits most SEs.

Imaging using photoelectrons directly emitted from a core-level can be very useful and allows for determination of the surface chemistry with high spatial resolution. For core-levels experiencing somewhat large chemical shifts, it is also possible to image using a specific chemical state of the atomic species. In Figure 6.10, results from a SPELEEM study performed on long, doped InP NWs deposited on a Si substrate are presented, also described in Paper III. From the MEM image, the overall morphology of the NW can be

identified and the contrast indicates work function differences along the NW. Switching to PEEM mode and forming an image using core-level electrons allows for determination of the spatial distribution of certain elements. In Figure 6.10(d), photoelectrons from the In*4d* core-level are imaged and it is clear that In was found to be located in the NW only (as would be expected). NW core-level imaging usually has a rather low signal-to-noise ratio and an image such as 6.10(c) typically has an acquisition time of 2–5 min.

It is also possible to form images using secondary electrons. SEs have been studied for a long time and are not unique to cathode lens microscopy. In all instruments where SEs are emitted, e.g. SEMs, TEMs, and PEEMs, one can obtain the information carried by the SEs. However, in most instruments it is not possible to tune in SEs with specific energies (energy filtering) thus losing much of the information. SEs are common to use in PEEM experiments since the signal is very high and allows for short image acquisition times and even video rate imaging. It is also an excellent starting point in every experiment in order to tune the electron lenses and ensure that the photoelectrons are on the optical axis.

SE images show contrast between almost anything, such as material variations, changes in charge carrier concentrations, crystal structure variations, etc. The challenging task is to understand what gives rise to the contrast. One of the reasons for the non-trivial interpretation is that the vast amount of literature in this field often is centered on a specific experiment or a specific sample. Experiments have been performed using a number of different excitation sources such as electron beams[141], UV light[142, 143], and x-ray sources[144]. The analyzed systems include metals[145] and semiconductors[143], and the sample environments range from modest vacuum[146] to UHV environment[147]. Further, the detection of the SEs has been performed in different setups either by measuring the integrated SE signal (the SE yield)[146], low pass energy filtering[148], or using true energy filtering[144]. It is therefore not unexpected that a number of different explanations for the contrast have been presented, including Fermi level pinning[147], metal over layers[149], and locally varying vacuum levels outside the sample[150]. Another reason for the non-trivial interpretation is the complicated situation in semiconductors where you not only have a work function (Fermi level to vacuum) as in a metal, but due to the band gap also have electron affinity (conduction band minimum to vacuum) and ionization energy (valence band maximum to vacuum). Determining which quantities are probed is not a trivial task as several groups have reported[141, 149, 151].

During the work presented in this dissertation, the acquisition and my interpretation of SE data have developed, leading up to the method and explanation presented herein. A single image in itself is most often not necessary to obtain quantitative data about a system. Instead, I have been mapping the SE intensity as a function of their kinetic energy, gaining knowledge about how low energy the emitted electrons can have and still be detected.

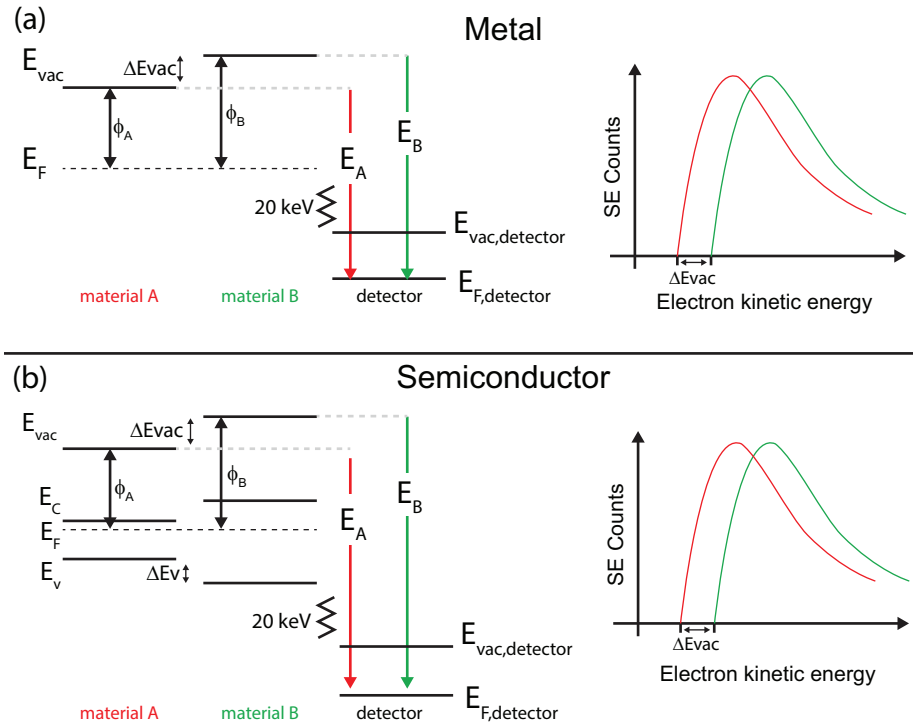

Figure 6.11. Model of SE emission when mapping the SE onset.(a) Schematic band diagram showing emission of SEs from two metals, *A* and *B*, with different work function, ϕ_a and ϕ_b, and aligned Fermi levels, E_F. The varying work functions give rise to locally varying vacuum levels just outside the sample surface. The sample is biased –20 kV with respect to the detector and the Fermi level of the detector is therefore lower than the sample's E_F. The lowest energy an electron escaping from *A* (*B*) can have when detected is E_A (E_B). The corresponding SE onset shift can be seen in the spectrum. (b) For a semiconductor, the situation is more complicated with possible conduction (E_c) and valence band (E_v) offsets. The Fermi levels are, still aligned and the varying vacuum levels arise from the different work functions. The corresponding SE onset curves can be seen in the spectrum. Please note that the energy distances are not drawn to scale.

The principle of mapping the SE onset can be seen in Figure 6.11(a). For two metal materials, *A* and *B*, with varying work functions, the local vacuum level just outside the sample will vary, reaching a uniform value first at a macroscopic distance[152]. The sample is floating at high negative potential in the PEEM and every electron that has enough energy to leave the sample can be detected[153]. The lowest energy an electron leaving *A* can have when detected is E_A, and similar E_B for an electron leaving *B*. In the SE spectra, this shows up as a shift of the SE peaks where the difference in local vacuum level potential as it is just outside the two materials can be deduced. For two semiconductor

materials, the situation is more complicated, Figure 6.11(b). The Fermi levels are still aligned, but two additional quantities exist: the electron affinity which is the energy distance from conduction band minimum to vacuum, and ionization energy which is the energy distance between valence band maximum to vacuum. For high energy excitation, as in the case of x-ray experiments, SEs will mainly be emitted from the densely occupied valence band, but the SE onset energy will also here be governed by the local vacuum level potential outside the two semiconductor materials. Importantly, since the SE emission onset only gives the position of the local vacuum level with respect to the Fermi level (the work function), additional information about the valence and conduction band edges are needed for complete characterization of the surface bands. Such information can be gained using STS and in Paper III and VII, this powerful combination was used to map all relevant electronic band for InP and InAs, respectively. Additionally, the shape of the SE peak is in principle determined by electron–electron interaction in the sample[154], but is modulated by the transfer function of the microscope[153] and for the systems I have been studying, it is hard to say what is governing the shape.

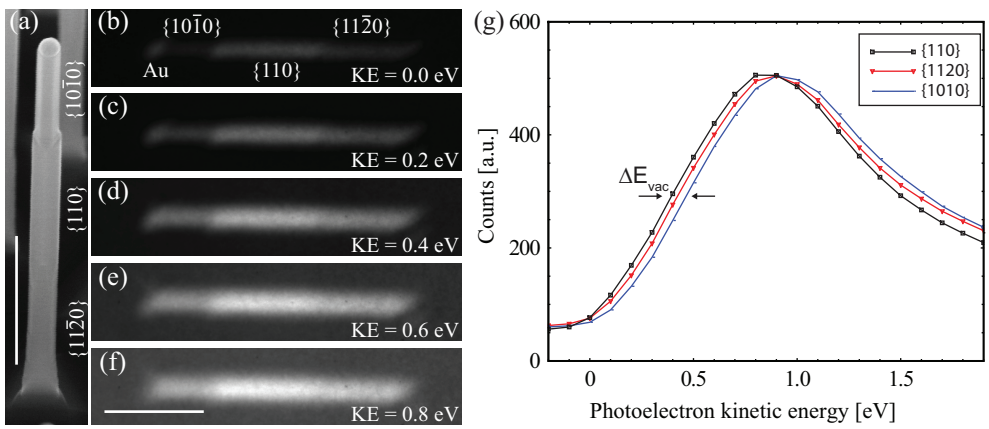

Figure 6.12. SE XPEEM study of an InAs NW with axial stacking of Wz and Zb segments with surface facets as indicated in the (a) 30 ° tilted view SEM image of an InAs NW. Scale bar denotes 500 nm. (b–f) Secondary electron XPEEM images of the InAs NW in (a) obtained using different photoelectron kinetic energy (KE). Scale bar in (f) is valid also for (b–e) and denotes 1 µm. (g) Normalized photoelectron count from the 3 different NW segments extracted from the SE XPEEM images. ΔE_{vac} denotes the difference in local vacuum level position) with {110} facets having the lowest E_{vac}. Photon energy was 70 eV. Energy window in (b–f) 0.5 eV.

In Figure 6.12 SE XPEEM results from InAs NWs with axial stacking of Wz-Zb-Wz, terminated by {11–20}, {110}, and {10–10} surfaces is shown. The surface termination of each segment was verified by µLEED as described in Paper VII. When tuning in secondary photoelectrons, Figure 6.12(b), it was possible to resolve all 3 segments as well

as the Au-In alloy particle residing on top of the NW, due to their different SE emission. As photoelectrons with higher kinetic energy are used to form the image, the signal went up but the contrast between the different segments went down. By plotting the secondary photoelectron count as extracted from each image, Figure 6.12(g), it was possible to extract the SE onset profile for each segment. Extracting the vacuum level difference at the linear part of the onset[145], gives the lowest vacuum level potential for {110} followed by a 30 meV higher vacuum level for its Wz counterpart, {11–20}, and an 80 meV vacuum level for {10–10} (compared to {110}).

In Paper IV, a SE study performed on InP NWs with an undoped segment sandwiched in between two highly doped n-type ends was presented. It was obvious that a dopant induced contrast existed and the transition regions between the n-type and undoped was mapped. Going from n-type to undoped during growth resulted in a longer transition region than going from undoped to n-type. This was explained using a graded transition region where dopants were incorporated into the NW a short time after the shutter to the source was closed.

In Paper III, InP NWs with axial stacking of n-type and p-type segments were studied. In this study, it was noticed that the contrast did not show the conventional intensity scale with p-type being brightest, gradually becoming darker as the material gets more and more n-type. Instead, I noticed a very low SE emission from the p-type segment which was explained using surface accumulated Zn oxide acting to lower the SE yield, and larger ionization energy in p-type InP (motivated by a change of crystal structure). In the article, it is assumed that the measured quantity between the two SE onsets, is the ionization energy and not the work function. Having improved our model and assuming that the difference in SE onset is the difference in local vacuum level, the interpretation of the results must be slightly modified. However, the only implications this has for level positions are that the local vacuum level at the n-type part is 60 meV higher than at the p-type part (previously 380 meV lower).

In addition to analyzing shifts of the SE onset, it is possible to analyze intensity variations of the SE emission. This can be challenging and care should be taken when analyzing the SE yield as a number of factors can (at least in theory) affect the SE emission. Henke proposed that rougher surfaces, due to their larger surface area, should promote SE emission[155]. Crystal defects such as stacking faults and dislocations have been shown to decrease the SE emission through increased inelastic scattering of the SEs on their path towards the surface[155]. The previously mentioned metal over layers, resulting from e.g. electron beam induced carbon contamination of the surface in electron microscopes, can result in Ohmic or Schottky contacts acting to increase or lower the SE emission[149, 156].

These SE intensity affecting factors can, however, often be ruled out when performing studies combining several techniques. The crystal quality is often well-known from TEM measurements, and surface roughness can be deduced using STM. Contaminating carbon

over layers are, in general, not a problem in the UHV environment in the LEEM/PEEM setup. In addition, it is possible to perform spatially resolved XPS in order to track the surface chemistry in the PEEM. SE measurements performed within LEEM/PEEM systems are therefore often preferred over similar measurements in less controlled environments such as SEMs.

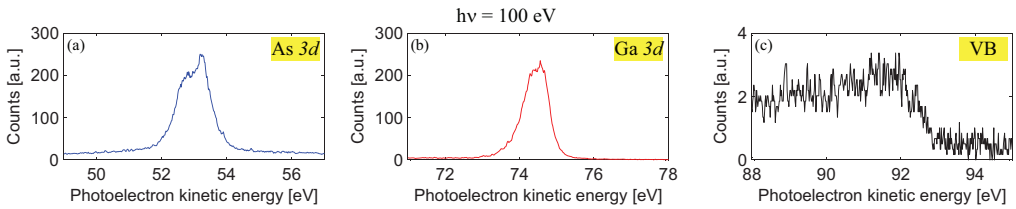

Figure 6.13. Photoelectron spectra from the top facet of a single GaAs micropillar (depicted in Figure 6.9) obtained in the PEEM system using 100 eV photons. (a) As *3d* spectrum showing no sign of As-oxide species. (b) Ga *3d* spectrum. (c) Spectrum obtained at the valence band (VB) region. Acquisition time for each spectrum was 2.5 min.

In the SPELEEM it is also possible to project the dispersion plane of the hemispherical electron energy analyzer thus showing photoelectron spectra. In Figure 6.13, I show XPS-spectra obtained from the top facet on one of the short micropillars depicted in Figure 6.9, having an acquisition area < 1 μm^2. Core-level spectra obtained from the As*3d* and Ga*3d* levels show a quite high signal-to-noise-ratio making it possible to see, among other things, the lack of As-oxides. Using the same acquisition time (2.5 min) for the VB photoelectrons I detected a signal roughly 100 times lower since the cross-section for photoionization goes down with increasing photon energy. In order to use PEEM for nanoscale band mapping, as has been done on e.g. graphene[157], it is therefore necessary to have materials giving a sufficiently high VB photoelectron signal, and GaAs is problematic. However, with the advent of the new aberration corrected systems the transmission of the microscopes is expected to increase tenfold allowing for studies of GaAs and other materials not possible today[123, 128].

7. Concluding remarks and outlook

The work presented in this dissertation demonstrates the successful usage of surface sensitive probes for studies of III–V NWs. Several means to overcome technical difficulties when adapting characterization techniques developed for 2D studies into 3D platforms have been discussed.

Using a novel route to deoxidize NWs, it was possible for us to present the first atomically resolved STM study of III–V NW surfaces in Paper I. Since then, other groups have followed and today 5 papers on the subject have been published world-wide (whereof 3 are due to the work behind this dissertation)[35, 44, 65, 66, 158]. The relatively few papers presented, despite the enormous amount of interest in NWs, reflect the challenges involved when performing STM on NWs.

Obtaining clean and well-ordered surfaces allowed for studies of electronic surface properties using STS. In Paper I and Paper III, STS was performed on InAs and InP NWs, respectively, showing surfaces influenced by states associated either with steps or with surface reconstructions. In Paper II, however, the first STS study of III–V NWs showing unpinned surfaces is presented. Unpinned surfaces allow for general probing of the electronic structure and have relevance both for surface and bulk regions of the sample, making them highly interesting for fundamental studies. Achieving unpinned surfaces is not trivial since surface defects and steps easily can pin the Fermi level. It is therefore crucial to optimize both growth and deoxidation of the NWs to achieve clean and well-ordered systems. Until this day, no other STS studies have been presented showing unpinned NW surfaces.

The power of STM/S lies in its possibility to determine surface properties on the atomic scale (even though I use it to image micrometer scale surface morphology in Paper VIII). In order to obtain information along complete NWs, i.e. on the micrometer scale, LEEM and PEEM was used. PEEM and STM is a very useful combination since it gives the possibility to image the NWs from the atomic scale up to complete NWs. Combining PEEM and STS is also very powerful since it allows for combining the valence and conduction band levels as obtained from STS with the vacuum level as obtained from PEEM. In Paper III and Paper VII, the results of such combinations are presented and it was shown to be possible to probe the position of all relevant electronic bands for individual NW segments.

The LEEM has not previously been used for NW studies and the complex contrast variations observed at very low electron energy (MEM) is explained in Paper V. The contrast was found to be very sensitive to work function variations along the NW but rather insensitive to NW geometry. The study performed here allows for continued studies of more advanced structures with electronic or magnetic variations along the NW. It is interesting to note that within Paper V, the first LEED-pattern from a III–V NW is presented. The possibility to obtain LEED patterns from small NW segments is very interesting since it is the first step towards quantitative LEED experiments where patterns are obtained over large electron kinetic energy ranges. Quantitative LEED can be used to, determine atomic relaxations in the top most few layers of the surface.

Both STM and LEEM were seen to be able to give important surface information for clean NWs. For NWs covered in oxide (either native or high-κ), other methods such as XPS was used. XPS has the possibility to probe the chemistry of buried interfaces such as the one between the NW and the oxide. In Paper VI, the first study of interfacial oxides for high-κ covered NWs was presented. The low surface coverage of NWs on the samples in conjunction with the attenuation of the photoelectron signal by the oxide make these studies incompatible with x-ray lab sources. Instead, there is a demand for synchrotron light sources able to deliver high intensity (and tunable) light. In Lund, we are well-equipped in this respect having the national synchrotron light source – the MAX-IV laboratory – close-by, being able to deliver x-rays with intensity permitting NW studies.

Looking back at III–V surface studies performed prior to the work presented in this dissertation, it has been devoted to the unpinned {110} surfaces which allow general probing of III–V properties[83]. As was shown in this work, III–V NWs offer two new unpinned, non-polar surfaces which also allow for general probing; namely the Wz {10–10} and {11–20} surface. These two additional surfaces offer an extra playground for surface scientists, and I foresee a bright future for studies within a number of surface related NW fields, including but not limited to the following:

(i) *Surface studies of NWs in operando.* Studies of contacted NWs that are characterized at the same time as they are being used as functional devices would be an excellent way to increase the complexity of the measurements. Studying under real operating conditions would be an elegant way to determine the most useful surfaces for device applications.

(ii) *Adsorption studies on NWs*. A number of adsorption studies, such as oxidation of NWs would be interesting to perform. Native oxides are sometimes linked to degradation in device performance and by studying a controlled oxidation process this effect could be understood in detail. Additionally, adsorption of larger molecules would be interesting in order to make hybrid organic-semiconductor devices, such as dye-sensitized solar cells[159].

(iii) *Fundamental studies of heterostructured NWs*. NWs grown with axial stacking of different materials and/or different crystal structures are interesting from a

fundamental as well as a technological point of view. Chemistry, atomic scale structure, and electronic properties at such interfaces are, most often not known and would be challenging to study. Examples include studies of homo- or heterostructure quantum dots which could be used as reliable single photon emitters[160].

(iv) *New material systems.* Surface studies of other materials systems, such as the III–N systems for LED-applications or III–Sb systems for electronics could be studied for their technological relevance. Verification of the proposed direct band gap in Wz GaP[47] would be very interesting for future optoelectronic applications such as high-efficiency green LEDs.

(v) *NWs as templates.* It would be interesting to use the unique NW surfaces as a template for growth of exotic materials, e.g. topological insulators. NWs have been grown in a wide range of material systems and with the Wz surfaces, it would be possible to grow lattice matched to materials where no growth substrates exist today. Especially, I think it would be very interesting to use Wz-Zb heterostructured NWs as templates for growing materials that would show different properties on the two segments, e.g. a material that is insulating when grown on the cubic segment but metallic when grown on the hexagonal segment. Examples of suitable materials are left as an exercise for the reader.

As can be seen from the list above, a virtual smorgasbord exists with experimental (and theoretical) challenges within all flavors of surface science. With this in mind, I am happy to have been part of the early work of NW surface characterization, and I expect the field to grow considerably the coming years.

8. Summary of papers

This chapter summarizes the papers that constitute the second part of the dissertation.

Paper I: Direct Atomic Scale Imaging of III–V Nanowire Surfaces

Here we report the first atomically resolved STM study of III–V semiconductor NWs. Using atomic hydrogen annealing, it was possible to remove the native oxide that naturally forms on the NWs upon contact with the ambient. The clean NW side facets could be probed by the STM tip and it was found that the two most common low-index wurtzite facets, {11–20} and {10–10}, were unreconstructed, as was also confirmed by *ab initio* calculations. STS measurements revealed electronic states within the entire band gap region, presumably originating from surface steps at the NWs.

Paper II: Direct Imaging of Atomic Scale Structure and Electronic Properties of GaAs Wurtzite and Zinc Blende Nanowire Surfaces

This paper describes an atomically resolved STM/S study of GaAs NWs grown with axial stacking of Zb and Wz crystal structure. The NWs were grown to expose the well-studied {110} surface at the Zb part and the two most common low-index Wz surfaces, {11–20} and {10–10}, at the Wz part. Performing STS on neighboring {110} and {11–20} facets and using the {110} facet as a reference, it was possible to obtain band gap energy and band offsets between Zb and Wz GaAs.

Paper III: Surface Chemistry, Structure, and Electronic Properties from Microns to the Atomic Scale of Axially Doped Semiconductor Nanowires

Doped InP NWs were studied using STM, XPS, and PEEM. With XPS, it was possible to monitor the removal of native oxide upon atomic hydrogen exposure revealing a release of an oxide induced n-type Fermi level pinning. From STM it was possible to detect reconstructed surfaces, in difference to what was found on InAs and GaAs NWs. Combining STS and PEEM, band diagrams with positions of surface valence and conduction band, as well as Fermi and vacuum level could be drawn.

Paper IV: Doping Profile of InP Nanowires Directly Imaged by Photoemission Electron Microscopy

Here we report on a fast way to determine doping profiles in InP NWs using SE XPEEM. Probing a NW with an undoped segment sandwiched between two highly doped n-type ends revealed contrast with the undoped segment emitting more photoelectrons. By studying the emitted SE intensity along the NW, it was possible for us map the space charge regions between the different segments. Varying lengths of the space charge regions was explained by memory effects where the introduction of dopants into the NWs was not terminated when the precursor gas flow turned off.

Paper V: Characterizing the Geometry of InAs Nanowires using Mirror Electron Microscopy

Large (diameter of 200-500 nm) InAs NWs were used as model systems in order to explain contrast observed in mirror electron microscopy (MEM). In MEM, low energy electrons are reflected of a potential field outside the sample surface, thereby not directly interacting with the sample itself. MEM shows non-intuitive contrast which was shown to be possible to simulate using caustic imaging theory. This paper describes the important quantities involved in explaining contrast observed during MEM of NWs.

Paper VI: Interface Composition of InAs Nanowires with Al_2O_3 and HfO_2 Thin Films

InAs NWs covered in thin films of two different high-κ dielectrica, Al_2O_3 or HfO_2, were studied using XPS. The interface between the high-κ and the NW is closely linked to device performance. Upon deposition of high-κ oxides a reduction of native oxides has been reported, so called self-cleaning. This effect was found to be less effective for NWs compared to bulk samples. It was also seen that the reduction of As-oxides was much more effective than the corresponding reduction of In-oxides. This type of studies is essential in order to understand and minimize electron trap formation at high-κ-semiconductor interfaces.

Paper VII: Electronic and Structural Mapping of Wurtzite and Zinc Blende InAs Nanowire Surfaces

InAs NWs with axial stacking of Wz and Zb segments were studied using a combination of STM/S, LEEM, and PEEM. Atomically resolved images from all common unreconstructed low-index surfaces ({11–20}, {110}, and {10–10}) were obtained. STS was used to probe neighboring Zb and Wz facets and the results were compared to theoretical calculations using *ab initio* methods. The surface structure was confirmed using LEEM and μLEED patterns could be obtained revealing (1 x 1) patterns for all above mentioned surfaces. From PEEM measurements it was possible to determine the position of the vacuum level.

Paper VIII: Scanning Tunneling Microscopy studies of Au-free Grown InAs Nanowires

STM was used to map surface morphology on Au-free grown InAs NWs. Imaging along several micrometers with monolayer height resolution over individual NWs showed a very low tapering of only 1.5 Å/μm, being under the detection limit of other techniques. A unique surface morphology not previously seen in other NW systems was found and attributed to arise from the abundance of stacking fault defects in the NWs. Individual As vacancies at the surface were probed using filled and empty states imaging. Finally, a tip asymmetry effect on the observed appearance was discussed.

Bibliography

[1] T. Mårtensson, *et al.*, "Epitaxial III–V Nanowires on Silicon," *Nano Letters,* **4**, 1987-1990, 2004.

[2] C. P. T. Svensson, *et al.*, "Monolithic GaAs/InGaP nanowire light emitting diodes on silicon," *Nanotechnology,* **19**, 305201, 2008.

[3] M. Egard, *et al.*, "Vertical InAs Nanowire Wrap Gate Transistors with ft > 7 GHz and fmax > 20 GHz," *Nano Letters,* **10**, 809-812, 2010.

[4] K. Tomioka, *et al.*, "A III-V nanowire channel on silicon for high-performance vertical transistors," *Nature,* **488**, 189-192, 2012.

[5] J. Wallentin, *et al.*, "InP Nanowire Array Solar Cells Achieving 13.8% Efficiency by Exceeding the Ray Optics Limit," *Science,* **339**, 1057-1060, 2013.

[6] N. Sköld, *et al.*, "Growth and Optical Properties of Strained GaAs–GaxIn1-xP Core–Shell Nanowires," *Nano Letters,* **5**, 1943-1947, 2005.

[7] A. Mikkelsen, *et al.*, "Direct imaging of the atomic structure inside a nanowire by scanning tunnelling microscopy," *Nature Materials,* **3**, 519-523, 2004.

[8] A. W. Dey, *et al.*, "High-Performance InAs Nanowire MOSFETs," *Electron Device Letters, IEEE,* **33**, 791-793, 2012.

[9] J. Wallentin, *et al.*, "High-Performance Single Nanowire Tunnel Diodes," *Nano Letters,* **10**, 974-979, 2010.

[10] P. Krogstrup, *et al.*, "Single-nanowire solar cells beyond the Shockley-Queisser limit," *Nature Photonics,* **7**, 306-310, 2013.

[11] M. T. Borgstrom, *et al.*, "Nanowires With Promise for Photovoltaics," *Ieee Journal of Selected Topics in Quantum Electronics,* **17**, 1050-1061, 2011.

[12] M. T. Björk, *et al.*, "One-dimensional Steeplechase for Electrons Realized," *Nano Letters,* **2**, 87-89, 2002.

[13] A. Das, *et al.*, "Zero-bias peaks and splitting in an Al-InAs nanowire topological superconductor as a signature of Majorana fermions," *Nature Physics,* **8**, 887-895, 2012.

[14] H. A. Nilsson, *et al.*, "Supercurrent and Multiple Andreev Reflections in an InSb Nanowire Josephson Junction," *Nano Letters,* **12**, 228-233, 2012.

[15] V. Mourik, *et al.*, "Signatures of Majorana Fermions in Hybrid Superconductor-Semiconductor Nanowire Devices," *Science,* **336**, 1003-1007, 2012.

[16] W. L. Magnus, *et al.*, "Strain mapping in free-standing heterostructured wurtzite InAs/InP nanowires," *Nanotechnology,* **18**, 015504, 2007.

[17] C. Philippe, *et al.*, "InSb heterostructure nanowires: MOVPE growth under extreme lattice mismatch," *Nanotechnology,* **20**, 495606, 2009.

[18] S. F. Fang, *et al.*, "Gallium arsenide and other compound semiconductors on silicon," *Journal of Applied Physics,* **68**, R31-R58, 1990.

[19] S. Chuang, *et al.*, "Ballistic InAs Nanowire Transistors," *Nano Letters,* **13**, 555-558, 2012.
[20] C. Thelander, *et al.*, "Nanowire-based one-dimensional electronics," *Materials Today,* **9**, 28-35, 2006.
[21] P. Caroff, *et al.*, "Crystal Phases in III-V Nanowires: From Random Toward Engineered Polytypism," *Ieee Journal of Selected Topics in Quantum Electronics,* **17**, 829-846, 2011.
[22] B. Mandl, *et al.*, "Growth Mechanism of Self-Catalyzed Group III-V Nanowires," *Nano Letters,* **10**, 4443-4449, 2010.
[23] M. Heurlin, *et al.*, "Continuous gas-phase synthesis of nanowires with tunable properties," *Nature,* **492**, 90-94, 2012.
[24] S. Hofmann, *et al.*, "Ledge-flow-controlled catalyst interface dynamics during Si nanowire growth," *Nature Materials,* **7**, 372-375, 2008.
[25] R. S. Wagner and W. C. Ellis, "Vapor-Liquid-Solid Mechanism of Single Crystal Growth (New Method Growth Catalysis from Impurity Whisker Epitaxial + Large Crystals Si E)," *Applied Physics Letters,* **4**, 89-&, 1964.
[26] M. E. Messing, *et al.*, "Generation of size-selected gold nanoparticles by spark discharge - for growth of epitaxial nanowires," *Gold Bulletin,* **42**, 20-26, 2009.
[27] C. Thelander, *et al.*, "Effects of Crystal Phase Mixing on the Electrical Properties of InAs Nanowires," *Nano Letters,* **11**, 2424-2429, 2011.
[28] H. J. Joyce, *et al.*, "Ultralow Surface Recombination Velocity in InP Nanowires Probed by Terahertz Spectroscopy," *Nano Letters,* **12**, 5325-5330, 2012.
[29] J. Wallentin, *et al.*, "Electron Trapping in InP Nanowire FETs with Stacking Faults," *Nano Letters,* **12**, 151-155, 2012.
[30] M. D. Schroer and J. R. Petta, "Correlating the Nanostructure and Electronic Properties of InAs Nanowires," *Nano Letters,* **10**, 1618-1622, 2010.
[31] K. A. Dick, *et al.*, "Parameter space mapping of InAs nanowire crystal structure," *Journal of Vacuum Science & Technology B,* **29**, 04D103, 2011.
[32] H. J. Joyce, *et al.*, "Phase Perfection in Zinc Blende and Wurtzite III–V Nanowires Using Basic Growth Parameters," *Nano Letters,* **10**, 908-915, 2010.
[33] J. Johansson, *et al.*, "Diameter Dependence of the Wurtzite-Zinc Blende Transition in InAs Nanowires," *Journal of Physical Chemistry C,* **114**, 3837-3842, 2010.
[34] P. Caroff, *et al.*, "Controlled polytypic and twin-plane superlattices in iii-v nanowires," *Nature Nanotechnology,* **4**, 50-55, 2009.
[35] T. Xu, *et al.*, "Faceting, composition and crystal phase evolution in III-V antimonide nanowire heterostructures revealed by combining microscopy techniques," *Nanotechnology,* **23**, 095702, 2012.
[36] R. E. Algra, *et al.*, "The Role of Surface Energies and Chemical Potential during Nanowire Growth," *Nano Letters,* **11**, 1259-1264, 2011.
[37] R. E. Algra, *et al.*, "Twinning superlattices in indium phosphide nanowires," *Nature,* **456**, 369-372, 2008.
[38] J. Wallentin and M. T. Borgstrom, "Doping of semiconductor nanowires," *Journal of Materials Research,* **26**, 2142-2156, 2011.
[39] M. T. Borgstrom, *et al.*, "Precursor evaluation for in situ InP nanowire doping," *Nanotechnology,* **19**, 2008.

[40] S. Lehmann, "A General Approach for Sharp Crystal Phase Switching in InAs, GaAs, InP, and GaP Nanowires Using Only Group V Flow," *Nano Letters,* **13**, 4099–4105, 2013.
[41] J. Johansson, *et al.*, "Growth related aspects of epitaxial nanowires," *Nanotechnology,* **17**, S355, 2006.
[42] E. T. Yu, "Cross-Sectional Scanning Tunneling Microscopy," *Chemical Reviews,* **97**, 1017-1044, 1997.
[43] J. Johansson, *et al.*, "Structural properties of (111)B-oriented III-V nanowires," *Nature Materials,* **5**, 574-580, 2006.
[44] M. Hjort, *et al.*, "Direct Imaging of Atomic Scale Structure and Electronic Properties of GaAs Wurtzite and Zinc Blende Nanowire Surfaces," *Nano Letters,* **13**, 4492–4498, 2013.
[45] V. Pankoke, *et al.*, "Role of sidewall diffusion in GaAs nanowire growth: A first-principles study," *Physical Review B,* **86**, 085425, 2012.
[46] V. Jindal and F. Shahedipour-Sandvik, "Density functional theoretical study of surface structure and adatom kinetics for wurtzite AlN," *Journal of Applied Physics,* **105**, 084902 2009.
[47] A. Belabbes, *et al.*, "Electronic bands of III-V semiconductor polytypes and their alignment," *Physical Review B,* **86**, 075208, 2012.
[48] A. De and C. E. Pryor, "Predicted band structures of III-V semiconductors in the wurtzite phase," *Physical Review B,* **81**, 155210, 2010.
[49] M. Murayama and T. Nakayama, "Chemical trend of band offsets at wurtzite/zinc-blende heterocrystalline semiconductor interfaces," *Physical Review B,* **49**, 4710-4724, 1994.
[50] C.-Y. Yeh, *et al.*, "Relationships between the band gaps of the zinc-blende and wurtzite modifications of semiconductors," *Physical Review B,* **50**, 2715-2718, 1994.
[51] Z. Zanolli, *et al.*, "Model GW band structure of InAs and GaAs in the wurtzite phase," *Physical Review B,* **75**, 245121, 2007.
[52] K. A. Dick, *et al.*, "Crystal Phase Engineering in Single InAs Nanowires," *Nano Letters,* **10**, 3494-3499, 2010.
[53] N. Akopian, *et al.*, "Crystal Phase Quantum Dots," *Nano Letters,* **10**, 1198-1201, 2010.
[54] D. Spirkoska, *et al.*, "Structural and optical properties of high quality zinc-blende/wurtzite GaAs nanowire heterostructures," *Physical Review B,* **80**, 2009.
[55] K. Haraguchi, *et al.*, "Gaas P-N-Junction Formed in Quantum Wire Crystals," *Applied Physics Letters,* **60**, 745-747, 1992.
[56] M. T. Bjork, *et al.*, "Si--InAs heterojunction Esaki tunnel diodes with high current densities," *Applied Physics Letters,* **97**, 163501-3, 2010.
[57] M. Heurlin, *et al.*, "Axial InP Nanowire Tandem Junction Grown on a Silicon Substrate," *Nano Letters,* **11**, 2028-2031, 2011.
[58] H. Pettersson, *et al.*, "Electrical and optical properties of InP nanowire ensemble p(+)-i-n(+) photodetectors," *Nanotechnology,* **23**, 135201, 2012.
[59] D. R. Khanal and J. Wu, "Gate coupling and charge distribution in nanowire field effect transistors," *Nano Letters,* **7**, 2778-2783, 2007.

[60] L. Vincent, *et al.*, "Composition and local strain mapping in Au-catalyzed axial Si/Ge nanowires," *Nanotechnology,* **23**, 395701, 2012.
[61] M. A. Hafez and H. E. Elsayed-Ali, "Atomic hydrogen cleaning of InP(100): Electron yield and surface morphology of negative electron affinity activated surfaces," *Journal of Applied Physics,* **91**, 1256-1264, 2002.
[62] T. Kikawa, *et al.*, "Atomic-Hydrogen Cleaning of Gaas and Inp Surfaces Studied by Photoemission Spectroscopy," *Surface Science,* **316**, 238-246, 1994.
[63] C. E. C. Wood, " III-V Alloy Growth by Molecular Beam Epitaxy in GaInAsP Alloy Semiconductors," ed. New York Wiley, 1982.
[64] K. A. Elamrawi, *et al.*, "Atomic hydrogen cleaning of InP(100) for preparation of a negative electron affinity photocathode," *Journal of Applied Physics,* **84**, 4568-4572, 1998.
[65] E. Hilner, *et al.*, "Direct Atomic Scale Imaging of III-V Nanowire Surfaces," *Nano Letters,* **8**, 3978-3982, 2008.
[66] M. Hjort, *et al.*, "Surface Chemistry, Structure, and Electronic Properties from Microns to the Atomic Scale of Axially Doped Semiconductor Nanowires," *Acs Nano,* **6**, 9679 2012.
[67] G. R. Bell, *et al.*, "Atomic hydrogen cleaning of polar III-V semiconductor surfaces," *Surface Science,* **401**, 125-137, 1998.
[68] Y. J. Chun, *et al.*, "Low Temperature Surface Cleaning of InP by Irradiation of Atomic Hydrogen," *Japanese Journal of Applied Physics,* **32**, L287.
[69] G. Binnig and H. Rohrer, "Scanning Tunneling Microscopy," *Helvetica Physica Acta,* **55**, 726-735, 1982.
[70] G. Binnig, *et al.*, "Surface Studies by Scanning Tunneling Microscopy," *Physical Review Letters,* **49**, 57-61, 1982.
[71] P. Ebert, *et al.*, "Contribution of Surface Resonances to Scanning Tunneling Microscopy Images: (110) Surfaces of III-V Semiconductors," *Physical Review Letters,* **77**, 2997-3000, 1996.
[72] R. M. Feenstra, *et al.*, "Atom-selective imaging of the GaAs(110) surface," *Physical Review Letters,* **58**, 1192-1195, 1987.
[73] J. Tersoff and D. R. Hamann, "Theory and Application for the Scanning Tunneling Microscope," *Physical Review Letters,* **50**, 1998-2001, 1983.
[74] J. Bardeen, "Tunnelling from a Many-Particle Point of View," *Physical Review Letters,* **6**, 57, 1961.
[75] J. Tersoff and D. R. Hamann, "Theory of the scanning tunneling microscope," *Physical Review B,* **31**, 805-813, 1985.
[76] C. J. Chen, "Microscopic View of Scanning Tunneling Microscopy," *Journal of Vacuum Science & Technology a-Vacuum Surfaces and Films,* **9**, 44-50, 1991.
[77] C. Weiss, *et al.*, "Imaging Pauli Repulsion in Scanning Tunneling Microscopy," *Physical Review Letters,* **105**, 086103, 2010.
[78] R. Temirov, *et al.*, "A novel method achieving ultra-high geometrical resolution in scanning tunnelling microscopy," *New Journal of Physics,* **10**, 053012, 2008.
[79] L. Gross, *et al.*, "High-Resolution Molecular Orbital Imaging Using a p-Wave STM Tip," *Physical Review Letters,* **107**, 086101, 2011.
[80] R. M. Tromp, *et al.*, "Quantum States and Atomic Structure of Silicon Surfaces," *Science,* **234**, 304-309, 1986.

[81] R. M. Feenstra, "Tunneling spectroscopy of the Si(111)2x1 surface," *Physical Review B,* **60**, 4478-4480, 1999.
[82] N. D. Lang, "Spectroscopy of Single Atoms in the Scanning Tunneling Microscope," *Physical Review B,* **34**, 5947-5950, 1986.
[83] R. M. Feenstra, "Tunneling Spectroscopy of the (110)-Surface of Direct-Gap Iii-V Semiconductors," *Physical Review B,* **50**, 4561-4570, 1994.
[84] P. Martensson and R. M. Feenstra, "Geometric and Electronic-Structure of Antimony on the Gaas(110) Surface Studied by Scanning Tunneling Microscopy," *Physical Review B,* **39**, 7744-7753, 1989.
[85] P. Martensson and R. M. Feenstra, "Voltage-Dependent Imaging of Antimony on the Gaas(110) Surface," *Journal of Microscopy-Oxford,* **152**, 761-769, 1988.
[86] R. Timm, "Formation, atomic structure, and electronic properties of GaSb quantum dots in GaAs," PhD Thesis, TU Berlin, Berlin, 2007.
[87] R. M. Feenstra*, et al.*, "Band gap of the Ge(111)c(2x8) surface by scanning tunneling spectroscopy," *Physical Review B,* **73**, 035310, 2006.
[88] M. McEllistrem*, et al.*, "Electrostatic sample-tip interactions in the scanning tunneling microscope," *Physical Review Letters,* **70**, 2471-2474, 1993.
[89] R. Dombrowski*, et al.*, "Tip-induced band bending by scanning tunneling spectroscopy of the states of the tip-induced quantum dot on InAs(110)," *Physical Review B,* **59**, 8043-8048, 1999.
[90] R. M. Feenstra*, et al.*, "Influence of tip-induced band bending on tunnelling spectra of semiconductor surfaces," *Nanotechnology,* **18**, 044015, 2007.
[91] G. J. de Raad*, et al.*, "Interplay between tip-induced band bending and voltage-dependent surface corrugation on GaAs(110) surfaces," *Physical Review B,* **66**, 195306, 2002.
[92] C. J. Chen, "In-situ characterization of tip electronic structure in scanning tunneling microscopy," *Ultramicroscopy,* **42–44**, 147-153, 1992.
[93] M. Morgenstern*, et al.*, "Low temperature scanning tunneling spectroscopy on InAs(110)," *Journal of Electron Spectroscopy and Related Phenomena,* **109**, 127-145, 2000.
[94] N. D. Jäger*, et al.*, "Scanning tunneling microscopy and spectroscopy of semi-insulating GaAs," *Physical Review B,* **65**, 195318, 2002.
[95] *SEMITIP software*. Available: http://www.andrew.cmu.edu/user/feenstra/semitip_v6/
[96] R. M. Feenstra and J. A. Stroscio, "Tunneling Spectroscopy of the Gaas(110) Surface," *Journal of Vacuum Science & Technology B,* **5**, 923-929, 1987.
[97] C. Davisson and L. H. Germer, "Diffraction of Electrons by a Crystal of Nickel," *Physical Review,* **30**, 705-740, 1927.
[98] C. J. Davisson and L. H. Germer, "The Scattering of Electrons by a Single Crystal of Nickel," *Nature,* **119**, 558-560, 1927.
[99] H. Hertz, *Ann. Phys. (Leipzig),* **31**, 983, 1887.
[100] A. Einstein, "Generation and conversion of light with regard to a heuristic point of view," *Annalen Der Physik,* **17**, 132-148, 1905.
[101] S. Günther*, et al.*, "Photoelectron microscopy and applications in surface and materials science," *Progress in Surface Science,* **70**, 187-260, 2002.

[102] G. Margaritondo, *Elements o Synchrotron Light*. Oxford: Oxford university press, 2002.
[103] J. M. Hollas, *Modern Spectroscopy*: Wiley, 2004.
[104] D. Briggs and P. Seah, *Practical Surface Analysis: Auger and X-ray photoelectron spectroscopy*: Wiley, 1990.
[105] S. Doniach and M. Sunjic, "Many-electron singularity in X-ray photoemission and X-ray line spectra from metals," *Journal of Physics C: Solid State Physics,* **3**, 285, 1970.
[106] R. Timm, *et al.*, "Reduction of native oxides on InAs by atomic layer deposited Al(2)O(3) and HfO(2)," *Applied Physics Letters,* **97**, 132904, 2010.
[107] R. Timm, *et al.*, "Interface composition of atomic layer deposited HfO(2) and Al(2)O(3) thin films on InAs studied by X-ray photoemission spectroscopy," *Microelectronic Engineering,* **88**, 1091-1094, 2011.
[108] J. J. Yeh and I. Lindau, "Atomic subshell photoionization cross sections and asymmetry parameters: $1 \leqslant Z \leqslant 103$," *Atomic Data and Nuclear Data Tables,* **32**, 1-155, 1985.
[109] R. Nyholm, *et al.*, "Beamline I311 at MAX-LAB: a VUV/soft X-ray undulator beamline for high resolution electron spectroscopy," *Nuclear Instruments & Methods in Physics Research Section a-Accelerators Spectrometers Detectors and Associated Equipment,* **467**, 520-524, 2001.
[110] R. M. Wallace, *et al.*, "Atomic Layer Deposition of Dielectrics on Ge and III–V Materials for Ultrahigh Performance Transistors," *Mrs Bulletin,* **34**, 493-503, 2009.
[111] W. Wang, *et al.*, "Is interfacial chemistry correlated to gap states for high-k/III–V interfaces?," *Microelectronic Engineering,* **88**, 1061-1065, 2011.
[112] G. D. Wilk, *et al.*, "High-κ gate dielectrics: Current status and materials properties considerations," *Journal of Applied Physics,* **89**, 5243-5275, 2001.
[113] W. Telieps and E. Bauer, "An analytical reflection and emission UHV surface electron microscope," *Ultramicroscopy,* **17**, 57-65, 1985.
[114] M. Mundschau, "Emission Microscopy and Surface Science," *Ultramicroscopy,* **36**, 29-51, 1991.
[115] J. Tersoff, *et al.*, "Running Droplets of Gallium from Evaporation of Gallium Arsenide," *Science,* **324**, 236-238, 2009.
[116] E. Hilner, *et al.*, "Ordering of the Nanoscale Step Morphology As a Mechanism for Droplet Self-Propulsion," *Nano Letters,* **9**, 2710-2714, 2009.
[117] B. Rausenberger, *et al.*, "LEEM and selected-area LEED studies of reaction front propagation," *Surface Science,* **287–288**, 235-240, 1993.
[118] B. Rausenberger, *et al.*, "Imaging reaction—diffusion fronts with low-energy electron microscopy," *Chemical Physics Letters,* **215**, 109-113, 1993.
[119] J. B. Hannon and R. M. Tromp, "Low-energy electron microscopy of surface phase transitions," *Annual Review of Materials Research,* **33**, 263-288, 2003.
[120] J. B. Hannon, *et al.*, "Dynamics of the silicon (111) surface phase transition," *Nature,* **405**, 552-554, 2000.
[121] F.-J. Meyer zu Heringdorf, *et al.*, "Growth dynamics of pentacene thin films," *Nature,* **412**, 517-520, 2001.

[122] F. M. Ross, *et al.*, "Transition States Between Pyramids and Domes During Ge/Si Island Growth," *Science,* **286**, 1931-1934, 1999.
[123] R. M. Tromp, *et al.*, "A new aberration-corrected, energy-filtered LEEM/PEEM instrument. I. Principles and design," *Ultramicroscopy,* **110**, 852-861, 2010.
[124] R. M. Tromp, *et al.*, "A New Low Energy Electron Microscope," *Surface Review and Letters,* **05**, 1189-1197, 1998.
[125] W. Swiech, *et al.*, "Recent progress in photoemission microscopy with emphasis on chemical and magnetic sensitivity," *Journal of Electron Spectroscopy and Related Phenomena,* **84**, 171-188, 1997.
[126] E. Bauer, "Photoelectron spectromicroscopy: present and future," *Journal of Electron Spectroscopy and Related Phenomena,* **114–116**, 975-987, 2001.
[127] E. Bauer, "Photoelectron microscopy," *Journal of Physics: Condensed Matter,* **13**, 11391, 2001.
[128] T. Schmidt, *et al.*, "First experimental proof for aberration correction in XPEEM: Resolution, transmission enhancement, and limitation by space charge effects," *Ultramicroscopy,* **126**, 23-32, 2013.
[129] S. A. Nepijko and G. Schönhense, "Measurement of potential distribution function on object surface by using an electron microscope in the mirror operation mode," *Journal of Microscopy,* **238**, 90-94, 2010.
[130] J. Slezák, *et al.*, "Surface diffusion of Au on Si(111): A microscopic study," *Physical Review B,* **61**, 16121-16128, 2000.
[131] M. E. Barnett and W. C. Nixon, "A mirror electron microscope using magnetic lenses," *Journal of Scientific Instruments,* **44**, 893, 1967.
[132] W. Święch, *et al.*, "In-situ studies of heterogeneous reactions using mirror electron microscopy," *Surface Science,* **294**, 297-307, 1993.
[133] S. M. Kennedy, *et al.*, "Laplacian image contrast in mirror electron microscopy," *Proceedings of the Royal Society A: Mathematical, Physical and Engineering Science,* **466**, 2857-2874, 2010.
[134] A. E. Luk'yanov, *et al.*, "Mirror electron microscopy," *Soviet Physics Uspekhi,* **16**, 529, 1974.
[135] S. A. Nepijko, *et al.*, "Measurement of the electric field distribution and potentials on the object surface in an emission electron microscope without restriction of the electron beams," *Journal of Microscopy,* **211**, 89-94, 2003.
[136] S. M. Kennedy, *et al.*, "Phase sensitivity of slow electrons to interactions with weak potentials," *Physical Review A,* **74**, 044701, 2006.
[137] T. Schmidt, *et al.*, "Double aberration correction in a low-energy electron microscope," *Ultramicroscopy,* **110**, 1358-1361, 2010.
[138] C. Riedl, *et al.*, "Quasi-Free-Standing Epitaxial Graphene on SiC Obtained by Hydrogen Intercalation," *Physical Review Letters,* **103**, 246804, 2009.
[139] C. Virojanadara, *et al.*, "Homogeneous large-area graphene layer growth on 6H-SiC(0001)," *Physical Review B,* **78**, 245403, 2008.
[140] P. W. Hawkes and J. C. H. Spence, *Science of microscopy*: Springer, 2007.
[141] I. Mullerova, *et al.*, "Imaging of the boron doping in silicon using low energy SEM," *Ultramicroscopy,* **93**, 223-243, 2002.
[142] V. W. Ballarotto, *et al.*, "Photon energy dependence of contrast in photoelectron emission microscopy of Si devices," *Applied Physics Letters,* **78**, 3547-3549, 2001.

[143] V. W. Ballarotto, *et al.*, "Model for doping-induced contrast in photoelectron emission microscopy," *Journal of Applied Physics,* **91**, 469-475, 2002.
[144] A. A. Zakharov, *et al.*, "Recent advances in imaging of properties and growth of low dimensional structures for photonics and electronics by XPEEM," *Journal of Electron Spectroscopy and Related Phenomena,* **185**, 417-428, 2012.
[145] O. Renault, *et al.*, "Work-function imaging of oriented copper grains by photoemission," *Surface and Interface Analysis,* **38**, 375-377, 2006.
[146] S. L. Elliott, *et al.*, "Dopant profiling with the scanning electron microscope—A study of Si," *Journal of Applied Physics,* **91**, 9116-9122, 2002.
[147] M. Giesen, *et al.*, "Characterization of p-n junctions and surface-states on silicon devices by photoemission electron microscopy," *Applied Physics a-Materials Science & Processing,* **64**, 423-430, 1997.
[148] P. Kazemian, *et al.*, "High resolution quantitative two-dimensional dopant mapping using energy-filtered secondary electron imaging," *Journal of Applied Physics,* **100**, 2006.
[149] M. M. El-Gomati, *et al.*, "Why is it that differently doped regions in semiconductors are visible in low voltage SEM?," *Electron Devices, IEEE Transactions on,* **51**, 288-292, 2004.
[150] C. P. Sealy, *et al.*, "Mechanism for secondary electron dopant contrast in the SEM," *Journal of Electron Microscopy,* **49**, 311-321, 2000.
[151] E. Pincik, *et al.*, "Properties of semiconductor surfaces covered with very thin insulating overlayers prepared by impacts of low-energy particles," *Vacuum,* **67**, 131-141, 2002.
[152] L. Kronik and Y. Shapira, "Surface photovoltage phenomena: theory, experiment, and applications," *Surface Science Reports,* **37**, 1-206, 1999.
[153] M. S. Claus and S. Gerd, "Investigating surface magnetism by means of photoexcitation electron emission microscopy," *Reports on Progress in Physics,* **65**, 1785, 2002.
[154] B. L. Henke, *et al.*, "Soft-x-ray-induced secondary-electron emission from semiconductors and insulators: Models and measurements," *Physical Review B,* **19**, 3004-3021, 1979.
[155] B. L. Henke, *et al.*, "0.1-10-Kev X-Ray-Induced Electron Emissions from Solids - Models and Secondary-Electron Measurements," *Journal of Applied Physics,* **48**, 1852-1866, 1977.
[156] G. H. Jayakody and M. M. El Gomati, "SE dopant contrast in LVSEM: The effects of surface and vacuum conditions," *Electron Microscopy and Analysis* **2003**, 389-392, 2004.
[157] A. A. Zakharov, *et al.*, "Nanoscale 3-D (E, k_x, k_y) band structure imaging on graphene and intercalated graphene," *Ibm Journal of Research and Development,* **55**, 6:1-6:6, 2011.
[158] P. Capiod, *et al.*, "Band offsets at zincblende-wurtzite GaAs nanowire sidewall surfaces," *Applied Physics Letters,* **103**, 122104-4, 2013.
[159] B. O'Regan and M. Gratzel, "A low-cost, high-efficiency solar cell based on dye-sensitized colloidal TiO2 films," *Nature,* **353**, 737-740, 1991.
[160] M. T. Borgstrom, *et al.*, "Optically bright quantum dots in single nanowires," *Nano Letters,* **5**, 1439-1443, 2005.